GKSS
FORSCHUNGSZENTRUM
in der HELMHOLTZ-GEMEINSCHAFT

Modeling and simulation of deformation and fracture behavior of components made of fully lamellar γTiAl alloy

(Vom Promotionsausschuss der Technischen Fakultät der Christian-Albrechts-Universität zu Kiel als Dissertation angenommene Arbeit)

Author:

M. R. Kabir

ISSN 0344-9629

HELMHOLTZ
| GEMEINSCHAFT

wissen
schafft
nutzen

GKSS 2008/11

GKSS 2008/11

Modeling and simulation of deformation and fracture behavior of components made of fully lamellar γTiAl alloy

(Vom Promotionsausschuss der Technischen Fakultät der Christian-Albrechts-Universität zu Kiel als Dissertation angenommene Arbeit)

Author:

M. R. Kabir

(Institute of Materials Research)

GKSS-Forschungszentrum Geesthacht GmbH · Geesthacht · 2008

Die Berichte der GKSS werden kostenlos abgegeben.
The delivery of the GKSS reports is free of charge.

Anforderungen/Requests:

GKSS-Forschungszentrum Geesthacht GmbH
Bibliothek/Library
Postfach 11 60
21494 Geesthacht
Germany
Fax.: +49 4152 87-17 17

Als Manuskript vervielfältigt.

ISSN 0344-9629

GKSS-Forschungszentrum Geesthacht GmbH · Telefon (04152) 87-0
Max-Planck-Straße 1 · 21502 Geesthacht / Postfach 11 60 · 21494 Geesthacht

GKSS 2008/11

Modeling and simulation of deformation and fracture behavior of components made of fully lamellar γTiAl alloy

(Vom Promotionsausschuss der Technischen Fakultät der Christian-Albrechts-Universität zu Kiel als Dissertation angenommene Arbeit)

Mohammad Rizviul Kabir

107 pages with 85 figures and 7 tables

Abstract

The present work deals with the modeling and simulation of deformation and fracture behavior of fully lamellar γTiAl alloy; focusing on understanding the variability of local material properties and their influences on translamellar fracture. A fracture model has been presented that takes the inhomogeneity of the local deformation behavior of the lamellar colonies as well as the variability in fracture strength and toughness into consideration. To obtain the necessary model parameters, a hybrid methodology of experiments and simulations has been adopted. The experiments were performed at room temperature that demonstrates quasi-brittle response of the TiAl polycrystal. A remarkable variation in stress-strain curves has been found in the tensile tests. Additional fracture tests showed significant variations in crack initiation and propagation during translamellar fracture. Analyzing the fracture surfaces, the micromechanical causes of these macroscopic scatter have been explained. The investigation shows that the global scatter in deformation and fracture response is highly influenced by the colony orientation and tilting angle with respect to the loading axis. The deformation and fracture behavior have been simulated by a finite element model including the material decohesion process described by a cohesive model. In order to capture the scatter of the macroscopic behavior, a stochastic approach is chosen. The local variability of stress-strain in the polycrystal and the variability of fracture parameters of the colonies are implemented in the stochastic approach of the cohesive model. It has been shown that the proposed approach is able to predict the stochastic nature of crack initiation and propagation as observed from the experiments. The global specimen failure with stable or unstable crack propagation can be explained in terms of the local variation of material properties.

Modellierung und Simulation des Verformungs- und Bruchverhaltens von Bauteilen aus lamellaren γTiAl-Legierungen

Zusammenfassung

Ziel der vorliegenden Arbeit ist die numerische Analyse durch Modellierung und Simulation des Verformungs- und Bruchverhaltens von lamellaren Titan-Aluminid-Legierungen (γTiAl) im kontinuumsmechanischen Rahmen der Finiten-Element-Methode. Im Zentrum der Arbeit steht

dabei die Berücksichtigung der stochastischen Variabilität von lokalen Materialeigenschaften und deren Auswirkung auf die global messbaren Größen wie Kraft und Verschiebung einschließlich der dabei auftretenden lamellaren Rissentwicklung. Hierfür wurde ein neuartiger stochastischer Ansatz verwendet, bei dem lokale Werkstoffinhomogenitäten im Modell durch unregelmäßige Verteilung von Zugfestigkeiten und Bruchzähigkeiten berücksichtigt werden. Unter der Bezeichnung lokal wird hierbei die Mesoebene über der Mikrostruktur verstanden, bei der die Eigenschaften von einer Lamellenkolonie als homogen betrachtet werden. Die unregelmäßige Verteilung ergibt sich durch die Vielzahl von Kolonien in einem Probenkörper mit jeweils unterschiedlichen Materialeigenschaften. Mit dem stochastischen Ansatz lassen sich so unterschiedliche Verteilungen systematisch analysieren. Für die Simulation des Polykristalls aus γTiAl wurden die Kolonien durch regelmäßige Blöcke idealisiert und mit stochastischen Materialparametern versehen. Für die Beschreibung der Bruchentwicklung wurde das Kohäsivmodell verwendet. Um die lokalen Modellparameter realitätsnah zu bestimmen, wurde eine hybride Vorgehensweise gewählt, bei der zum einen experimentell zugängliche lokale Parameter direkt verwendet werden und zum anderen die weiteren Parameter durch numerische Simulationen an Hand von global bestimmten experimentellen Kurven ergänzt werden. Das Werkstoffverhalten wurde bei Raumtemperatur bestimmt, da hierbei das quasi-spröde Verhalten der polykristallinen γTiAl-Legierung als Turbinenwerkstoff der kritische Zustand ist. Versuche an Flachzugproben ergaben (makroskopisch) eine deutliche Variation in den Spannungs-Dehnungskurven. Ebenso zeigten die Versuche an Bruchmechanikproben eine signifikante Variation hinsichtlich der Rissintiierung und translamellaren Rissausbreitung sowie Eintritt des instabilen Versagens. Die Analyse der Bruchflächen bei den Chevron-Biegeproben lieferte ein Verständnis über die Streuung der Kraft-Verschiebungskurven. Darüber hinaus zeigen die Simulationen, dass nicht notwendigerweise das schwächste Korn (Kolonie) das Versagen einleitet, sondern daran auch die Orientierungen der Nachbarkolonien in Form von unterschiedlichen Festigkeiten beteiligt sind. Es konnte gezeigt werden, dass mit dem gewählten stochastischen Ansatz das Verhalten von Zug- und Biegeproben mit unregelmäßiger Rissentwicklung sowie das instabile Versagen realitätsnah beschreibbar sind.

Manuscript received / Manuskripteingang in TKP: 22. Dezember 2008

Contents

Notations

Cohesive parameters

T_0	Maximum cohesive traction
Γ_0	Critical separation energy
δ_0	Maximum cohesive separation
δ_1, δ_2	Cohesive shape parameter

Crystal plasticity parameters

g_0	Critical resolved shear stress
h_0	Hardening parameter
$\dot{\gamma}^{(\eta)}$	Shear rate of the slip system η
$\tau^{(\eta)}$	Schmidt-stress in η

Deformation and Fracture parameters

σ	Uniaxial stress (from tension test)
ϵ	Total strain (from tension test)
σ_e	Equivalent stress
ϵ_e	Equivalent strain
σ_{22}	Component stress in direction 2
ϵ_{22}	Component strain in direction 2
K	Stress intensity factor
K_{Ic}	Critical stress intensity factor for mode I fracture
$\mathcal{G}$	Energy release rate
$\mathcal{G}_{Ic}$	Critical energy release rate for mode I fracture
J	J-Integral
a_0/W	Notch ratio

Abbreviations

$EPFM$	Elastic plastic fracture mechanics
$SE(B)$	Single notch bending specimen
CV	Chevron
$CMOD$	Crack mouth opening displacement
$CTOD$	Crack tip opening displacement
CZM	Cohesive zone model
$Rect-TSL$	Cohesive model with rectangular shape
$Tria-TSL$	Cohesive model with triangular shape
$CRSS$	Critical resolve shear stress
PST	Polly synthetically twinned
PUC	Periodic unit cell
RVE	Representative volume element
$RCorRD$	R for random, C or D for random type

Chapter 1

Introduction

1.1 Motivation

From the perspective of advanced light weight materials, the gamma based titaniumaluminide alloys (commonly known as γTiAl) are considered very attractive for high temperature applications [1, 2]. These alloys have excellent properties, which include low density (specific weight of 3.85 g/cm^3), high specific stiffness (elastic modulus about 175 MPa), and good oxidation resistance. Due to these properties the material is lightweight, and shows enhanced thermo-mechanical behavior compared to the conventional Ti and Ni alloys. Therefore, the alloy has been foreseen as a propitious material for different rotary components of aero engines [3]. Among the γTiAl alloy families, the fully lamellar microstructure with small colony size (about 50-150 μm) shows high stiffness and good fracture toughness [4–7]. The main drawbacks of this alloy are the poor ductility (1-2 % total strain), inherent brittleness and unpredictable nature of failure. As known from the laboratory testing, the alloy can not sustain increasing load after crack initiation, especially at room temperature where the material fails almost quasi-brittle manner. Sometimes, small propagation of cracks may occur depending on the geometry and loading type, however, the material ultimately fails catastrophically without undergoing noticeable plastic deformation.

In a fully lamellar polycrystal, lamellar colonies are randomly oriented in transverse direction. The failure in this type of microstructure is attributed to interlamellar or translamellar fracture which is controlled by the orientations of the lamellar colonies. During the transverse crack propagation a crack-front advances through favorably oriented lamellae, mostly by translamellar breaking, but also by interlamellar breaking when suitable lamellae orientations are present. The translamellar break of the lamellae plates results in a higher fracture toughness (higher resistance to fracture), while the interlamellar break between two lamellae interfaces produces a lower fracture toughness (lower resistance to fracture). The resistance to crack propagation varies throughout the fracture path as the main crack path is associated with small crack branching, crack bridging, and sometimes crack deflection at the lamellar boundaries [8–11]. The microstructural features, like lamellae thickness,

lamellae orientation, colony size and the tilting angle of the colonies to the loading direction results in the stochastic nature of crack initiation and propagation. This eventually leads to unpredictable brittle-like failure, showing scatter in the global force-displacement curves [12–15]. In components or structures, the variations in microstructure and material properties can not be avoided. Therefore, a characterization of the material with respect to the deformation and fracture behavior is necessary.

The material characterization can be done by adopting experiments, microstructure investigations and numerical analyses. Recently, numerical modeling has become a powerful research tool for exploring the micromechanisms of deformation and fracture at local and global windows. To capture the important phenomena that a material undergoes during external loading, a multi length-scale description combining microscopic to macroscopic details is required. Fig. 1.1 shows different length scales for the modeling of γTiAl alloys. At sub-micro level, dislocation movement within the crystal lattice can be taken into consideration. At micro-level, the micromechanisms of deformation (e.g., local plasticity effects from slip and twinning) can be well described by the crystal plasticity model. On the other hand, the global deformation and fracture of the material can be treated by meso and macro-level modeling considering the effects from well understood microscopical events (e.g., heterogeneity of material properties).

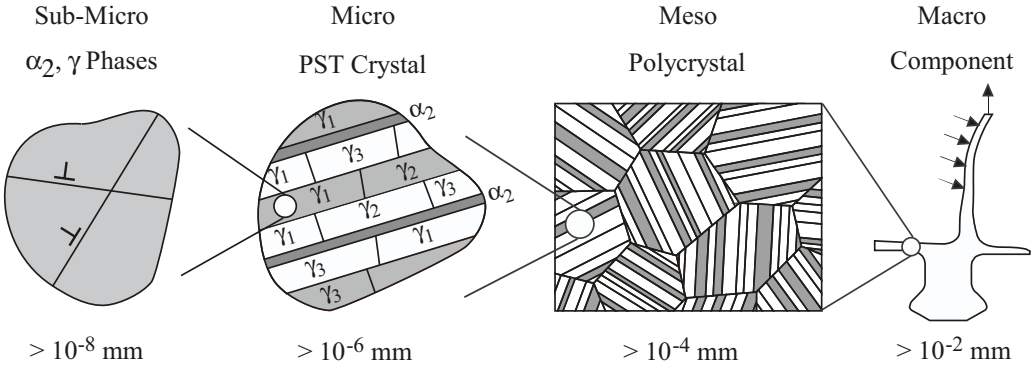

Figure 1.1: Different length scales for micromechanical modeling of γTiAl.

The numerical models that have been developed so far do not incorporate all the length scale phenomena. Certain developments have been achieved for quantitative and qualitative descriptions of the micro and macro mechanisms in single and multi-scale approaches. In general, the multi-scale modeling approaches are robust, and require large computer facilities; therefore, not suitable for component simulations. A common way of numerical modeling is to describe the required physical aspects in a single scale model (either macro, meso or micro scale), and to some extent, in a multi-scale model.

With respect to the modeling of γTiAl alloys, several works have advanced the general understanding of how microstructural effects influence the global deformation behavior of lamellar γTiAl alloy. The microstructural features, such as grain size, lamellar spacing, grain orientation are investigated to predict the stress-strain fields at room and high temperature [16–25]. Also, the mechanical fracture behavior of γTiAl alloys with different microstructural arrangements and variable material properties have already been discussed and described in great detail in literature, however, mostly using macro

scale descriptions [12, 18, 26–28].

To investigate the influence of varying material properties on mechanical and fracture behavior, a stochastic approach needs to be implemented. This approach incorporates probability theories to describe the likelihood of failure and the statistical distribution of the failure parameters. A well known implementation of such a method to describe brittle fracture and variation of material properties is the "Local approach of Weibull statistics" [29, 30]. In this approach the very local microcracks (e.g., defects in crystal lattice, microcrack in grain boundaries) are considered as fracture initiating sites. In the statistical fracture modeling, the Weibull distribution function provides the spread of local fracture strength to the whole material volume, while the "weakest link assumption" describes the brittle like fracture. Based on the Weibull weakest link principle, both analytical models [31, 32] and FE simulations are established to handle this kind of problems in concrete [33], ceramics [34], fiber composite materials [35] and TiAl alloys [26]. However, the variation band of local fracture strength is always unknown, and has to be assumed and validated with the global scatter of failure strength. Many experiments have to be conducted in order to determine the Weibull distribution parameters.

While the Weibull local approach describes the cleavage fracture probability due to microcracks only (a correlation between the microstructural features and the crack initiation is generally absent), another approach can be proposed for brittle (or quasi-brittle) fracture that takes into account the crack initiation and propagation criteria based on the meso-scale microstructural descriptions, e.g., randomly oriented lamellar colonies, as found in fully lamellar TiAl alloys. In this work an approach will be presented, which is based on the so called cohesive damage model (shortly, cohesive model). This model describe damage by a mechanism of decohesion of the material at a local region. The material decohesion occurs when certain critical fracture criteria, described by the cohesive model, are fulfilled. In order to capture the experimental scatter, the local fracture criteria can be considered as random fields related to the fracture of colonies. As known so far, the local heterogeneity of lamellar microstructure and their effects on the global fracture behavior (i.e., crack initiation, propagation, and unstable failure) have not been studied extensively.

1.2 Aim

The aim of this work is to investigate the quasi-brittle fracture of fully lamellar γTiAl alloy using a cohesive model and a stochastic approach. The local variability of fracture properties, i.e., cohesive strength and cohesive toughness of the material, and also the local inhomogeneous deformation behavior of the polycolonies are incorporated in the numerical model to predict the crack initiations and occurrence of failure with an acceptable reliability. The proposed approach will be verified through experiments at room temperature. The approach is briefly summarized in Fig. 1.2. Below is a more detailed descriptions of the step taken.

- Material characterization through experiments and fractography analysis (Fig. 1.2(a)): Focuses on the analysis of mechanical and fracture behavior. The test specimens will provide the stress-strain and fracture toughness data. From the fractographic analysis the heterogeneity of the microstructure and the experimental results will be correlated.

- Simulation scheme for validation (Fig. 1.2(b)): Local variation of stress-strain curves of a polycrystal of fully lamellar γTiAl alloy as well as the deformation constraint of the colonies will be predicted using a two-scale (micro to meso) model. The gathered data of the local variation of stress-strain curves will be implemented to a meso-scale model for simulating material deformation. Global fracture behavior of the experimental tests will be simulated using a stochastic approach of the cohesive model, which will provide relevant material parameters.

- Assessment of material parameter transferability (Fig. 1.2(c)): Considering the component as an idealized laboratory specimen, the material parameters for quasi-brittle fracture will be transferred to different types of laboratory specimens to predict the component failure behavior.

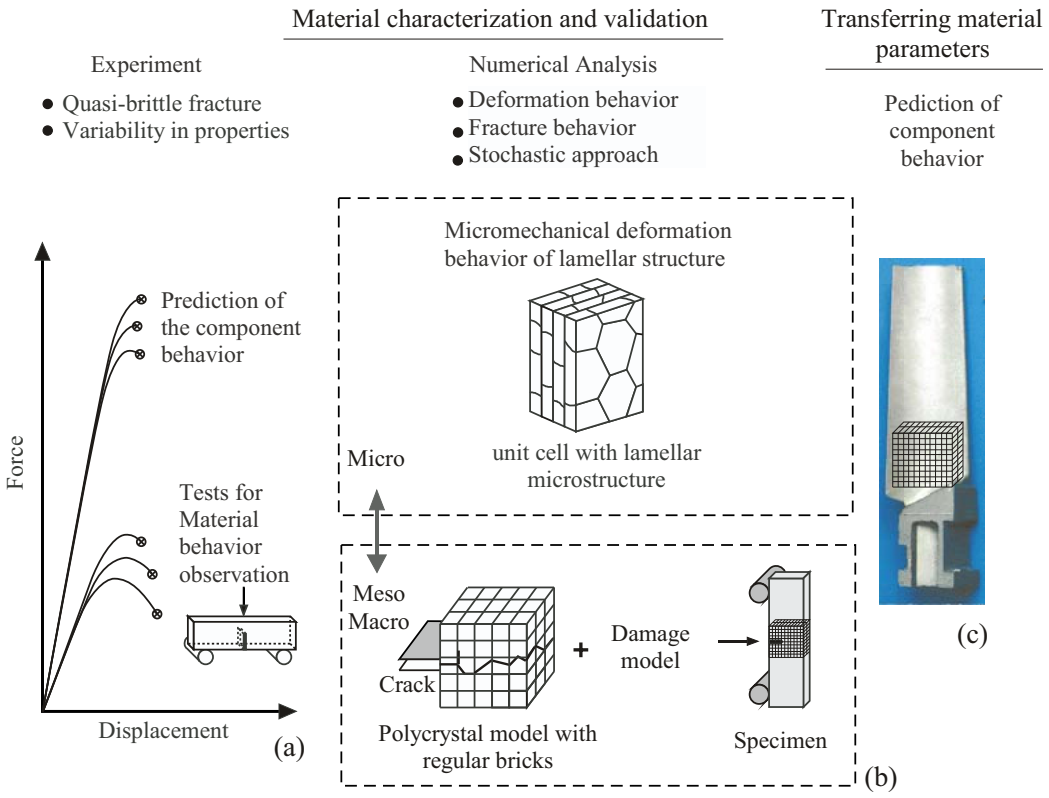

Figure 1.2: Investigation of deformation and fracture behavior of γTiAl: (a) material characterization with experiments, (b) numerical analysis for failure prediction and determination of material parameters, (c) prediction of failure of a test component by transferring the material parameters.

Chapter 2

Gamma based titanium aluminide alloy

The mechanical properties of gamma based TiAl alloys are highly sensitive to the minor microstructural changes. In general, the microstructures with acceptable ductility show poor fracture toughness and reduced creep resistance. Conversely, microstructures with improved toughness and creep resistance yield unsatisfactory ductility. Due to the inverse correlation between the tensile properties and the fracture resistance, a microstructural optimization for achieving well-balanced engineering properties is quite difficult. Today, a broad variety of γTiAl alloys with different microstructures can be custom tailored using novel processing techniques. Each microstructure is needed to be investigated to ensure their acceptability for industrial application. In the following section a brief introduction to the microstructure of a fully lamellar γTiAl alloy is given and the deformation behavior is discussed. The information will provide useful knowledge for the modeling inputs.

2.1 Preparation of fully lamellar γTiAl alloy

The material used in this investigation has the composition Ti-47Al-3.7(Nb,Cr,Mn,Si)-0.5B (in at%), and is denoted by γTAB at GKSS. An ingot obtained from triple vacuum arc melting (VAR) was used for subsequent extrusion. The extrusion was conducted at a billet temperature of about 1250 ^{0}C with an 7:1 extrusion ratio, resulting in a uniform, defect free extruded rod of 22 mm constant core diameter. A schematic view of the γTiAl extrusion is shown in Fig. 2.1.

The initial microstructure of the cast alloy and the extruded rod consists of duplex-type γ-grains. The fully lamellar microstructure was obtained through heat treatment at 1360 °C, holding for 30 min, followed by oil quenching. Finally, a mean colony size of approximately 100 μm was obtained.

During the extrusion process, colonies are aligned nearly parallel to the extrusion direction, while in the radial section of the extruded rod lamellar colonies are randomly oriented (see Fig. 2.2). Minor deviations (±20°) of parallel lamellae along the extrusion direction were confirmed by the texture analysis.

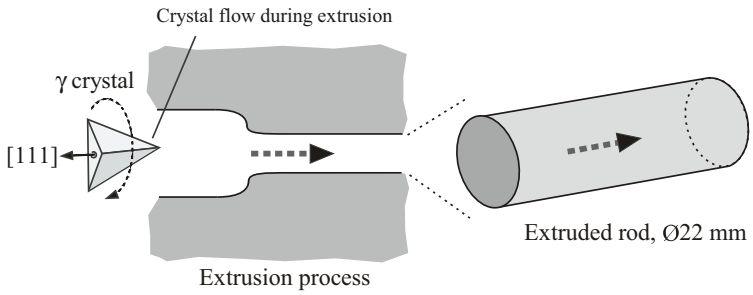

Figure 2.1: Schematic view of the extrusion process with crystal flow.

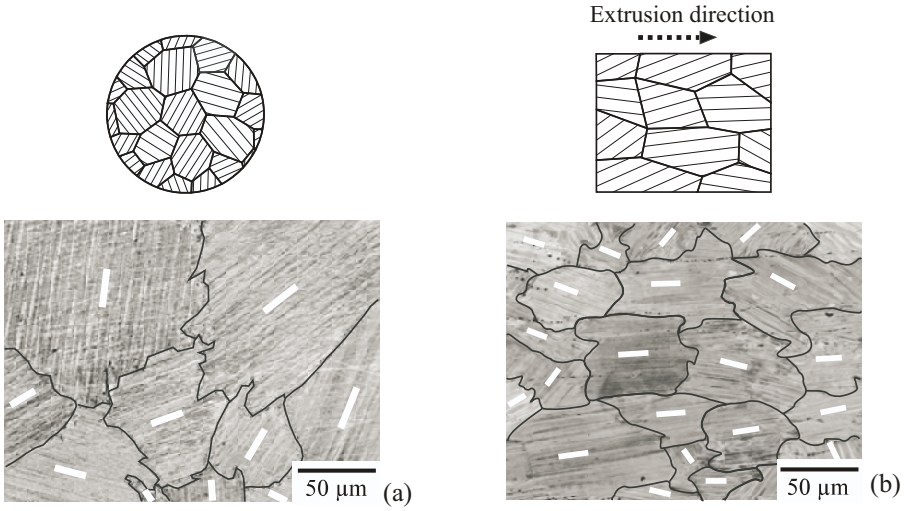

Figure 2.2: Colony orientation after heat treatment: (a) radial section, (b) longitudinal section.

2.2 Crystallographic structure

The lamellar structure in a single colony consists of two intermetallic phases, γ(TiAl) with face-centered tetragonal and α_2(Ti_3Al) with hexagonal crystallographic structure, as shown in Fig. 2.3(a,b). The lamellae are parallel to each other and each lamellar colony consists of a regular patterns of α_2 and γ lamellae. Usually, there are many γ-lamellae situated between two α_2 lamellae (Fig. 2.3(c)).

In the lamellae, crystallographic planes $(111)_\gamma$ and $(0001)_{\alpha 2}$ as well as the directions $<1\bar{1}0>\gamma$ and $<11\bar{2}0>\alpha_2$ are parallel. The arising lamellae interfaces are atomically flat over a large distance and are parallel to the {111} planes of the γ crystals. In the lamellar microstructure, according to Yamaguchi et al. [36], six domain structures with six different variants of γ lamellae occur, which are due to 60^0 rotation around an [111] direction. Three domains are formed due to the orientations of 0^0, 120^0 and 240^0, and are called matrix lamellae. The other three domains are due to the orientations of 180^0, 300^0 and 60^0, and are called twin lamellae. Matrix and twin lamellae have 180^0 orientation to each other. The microstructure with α_2 lamellae, γ lamellae with matrix and twin as well as their domain orientations are shown in Fig. 2.4(a,b).

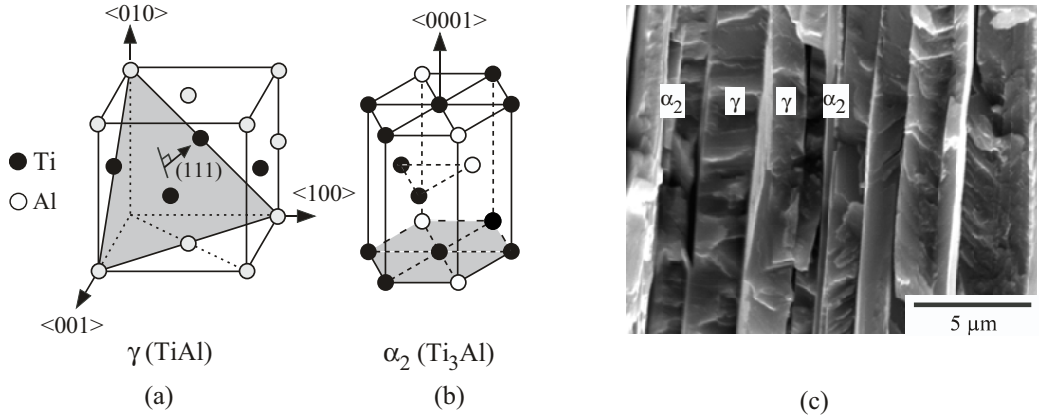

Figure 2.3: Crystallographic structure: (a) tetragonal γ-phase, (b) hexagonal α_2-phase, (c) fracture surface showing the alternating lamellae.

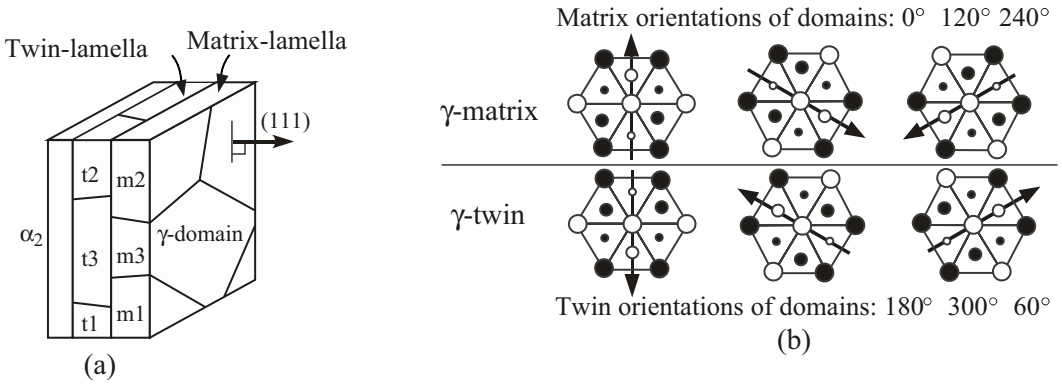

Figure 2.4: Domain structure in γ-lamellae: (a) lamellar structure with α_2 and γ-lamella including a simple representation of γ-domains, (b) matrix and twin domains and their orientation relationships.

2.3 Deformation of γTiAl

Room temperature plastic deformation of γTiAl occurs by crystallographic slip and mechanical twinning. The crystallographic slips are mainly activated by the ordinary and super dislocations. The ordinary dislocations are single dislocations with a Burgers vector, $\vec{b}$, as shown for a simple case of edge dislocation in Fig. 2.5(a). On the other hand, a superdislocation has a Burgers vector $2\vec{b}$ due to a pair of partial dislocations moving together as shown in Fig. 2.5(b). The partial dislocation occurs in an ordered crystal, creating an antiphase boundary in the slip plane when gliding over a certain area. It takes a second dislocation of the same kind to eliminate the antiphase boundary. A superdislocation is defined by adding these two partial dislocations.

Another deformation mode causing plasticity is twinning. Whereas the crystallographic orientation remains unchanged during slip, a reorientation occurs in a small volume of the crystal lattice during

twinning, see Fig. 2.6.

The deformation mechanisms for γTiAl alloys were investigated in numerous works during the last few decades [37–45]. As reported in literature, in α_2-crystals slip occurs in prismatic, basal and pyramidal planes whereas in γ-crystals slip occurs in $\{111\}_\gamma$-plane, as shown in Fig. 2.7.

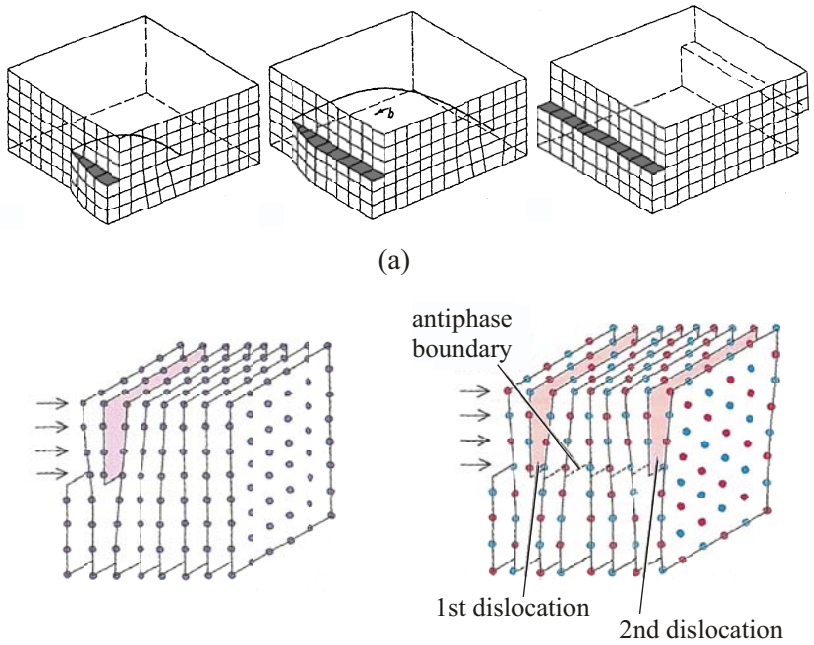

Figure 2.5: Dislocation movement: (a) single or ordinary dislocation through a cubic lattice, (b) super dislocation, i.e., two partial dislocation separated by antiphase boundary

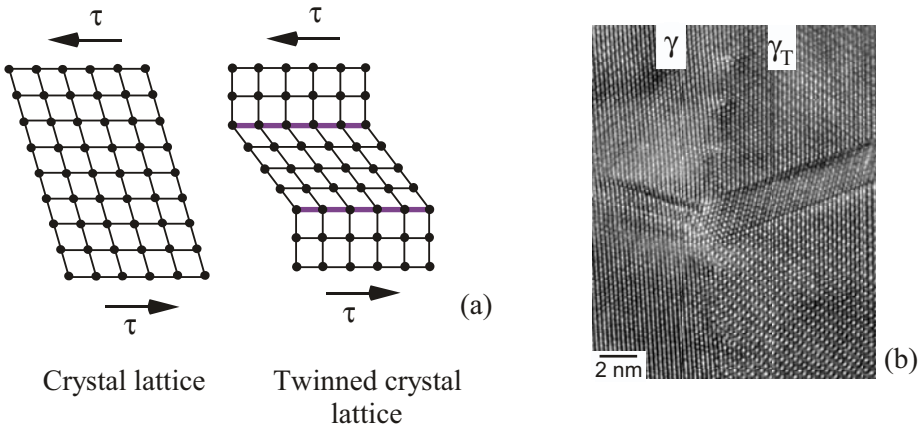

Figure 2.6: Mechanical twinning with crystal lattice reorientation: (a) schematic view, (b) deformation twin in a two-phase TiAl alloy. The twins were generated at the γ/γ_T interface.

According to [23] the slip systems in lamellar structures are divided into three slip modes, which are: longitudinal, mixed, and transverse, see Fig. 2.8. In longitudinal mode, glide planes and glide

directions are parallel to the lamellae planes, whereas in the mixed mode, only the glide directions are parallel. Finally, in transverse mode, neither the glide planes nor the glide directions are parallel to the lamellae planes.

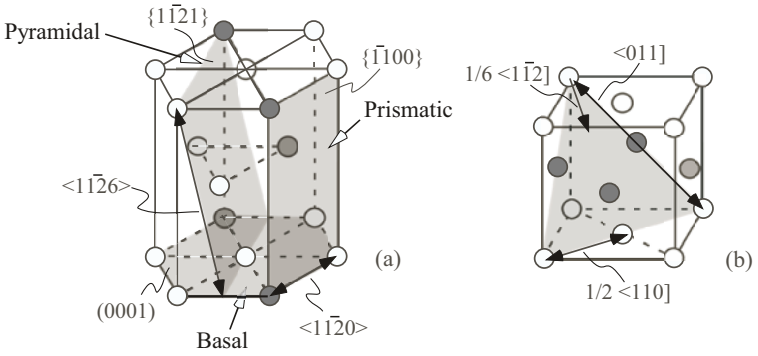

Figure 2.7: Slip systems in (a) α_2, and (b) γ

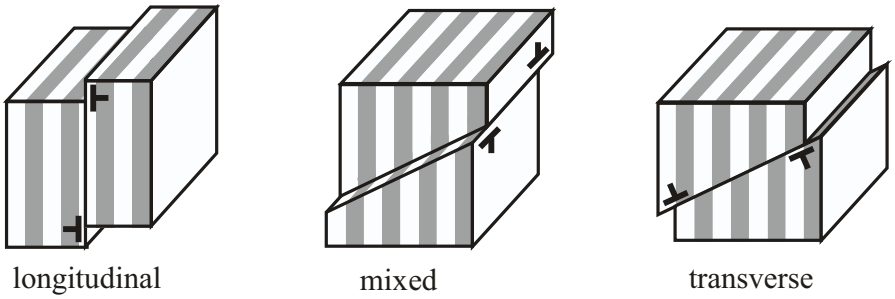

Figure 2.8: Three slip modes in lamellar microstructure

All possible slip systems that are found in two phase γTiAl are presented in Table 2.1 and Table 2.2.

The microstructural information (Section 2.2) and the deformation mechanisms presented here will be implemented to a micromechanical based numerical model, proposed by Werwer [46], and will be discussed in Chapter 6. The model will be used to simulate the local stress-strain responses of a γTiAl polycrystal.

Classification	longitudinal	mixed	transverse
Ordinary	(111) 1/2[1$\bar{1}$0]	(11$\bar{1}$) 1/2[1$\bar{1}$0]	($\bar{1}$11) 1/2[110]
	—	—	($\bar{1}\bar{1}$1) 1/2[110]
Super	(111) [01$\bar{1}$]	($\bar{1}\bar{1}$1) [01$\bar{1}$]	(11$\bar{1}$) [0$\bar{1}\bar{1}$]
	(111) [10$\bar{1}$]	($\bar{1}$11) [10$\bar{1}$]	(11$\bar{1}$) [$\bar{1}$0$\bar{1}$]
	—	—	($\bar{1}$11) [0$\bar{1}\bar{1}$]
	—	—	($\bar{1}\bar{1}$1) [$\bar{1}$0$\bar{1}$]
twin	($\bar{1}\bar{1}\bar{1}$) 1/6[11$\bar{2}$]	—	(11$\bar{1}$) 1/6[$\bar{1}\bar{1}$2]
	—	—	($\bar{1}$11) 1/6[$\bar{1}$1$\bar{2}$]
	—	—	($\bar{1}\bar{1}$1) 1/6[$\bar{1}$1$\bar{2}$]

Table 2.1: Slip systems in γ-TiAl according to [23]

Classification	longitudinal	mixed	transverse
prismatic	—	$\langle 11\bar{2}0\rangle\{1\bar{1}00\}$	—
basal	$\langle 11\bar{2}0\rangle\{0001\}$	—	—
pyramidal	—	—	$\langle\bar{1}\bar{1}26\rangle\{11\bar{2}1\}$

Table 2.2: Slip systems in α_2-Ti_3Al according to [23]

Chapter 3

Experimental investigations and fractography

3.1 Specimen preparation

Tensile and bending tests were performed to obtain the deformation and fracture behavior of the alloy. The specimen lengths were kept parallel to the extrusion direction (see Fig. 3.1). In order to ensure translamellar fracture, the notches of the fracture specimens were cut perpendicular to the extrusion direction.

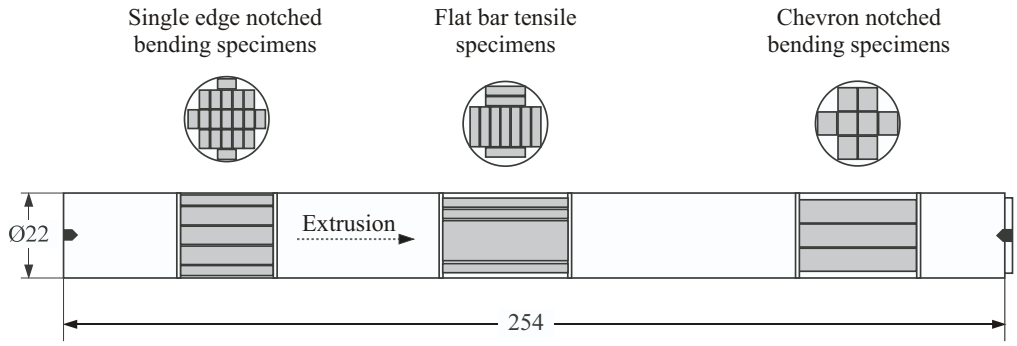

Figure 3.1: Extruded rod of γTAB alloy with specimen sections.

Tensile specimens

The geometrical details of the small-sized flat tensile specimens are shown in Fig. 3.2(a). The specimens were prepared using spark erosion, then mechanically polished to obtain defect free surfaces. The elongation during tensile loading was measured directly on one side of the flat specimen over a gauge length (L_0) of 7.5 mm. With this testing arrangements, the true stress-strain curves and the elastic slopes can be determined [47]. This data was used to describe the material elastic-plastic behavior

in the FE simulations.

Bend specimens

Single edge notched bend specimens (SE(B)) were prepared for two different types of notches: regular (rectangular) and chevron (triangular). The special feature of the chevron notch is that the tip of the triangular notch forces the initiation of a crack at a defined point, and provides an increasing crack-front width during crack propagation. Due to this effect, a crack-front can extend in a controlled manner, even sometimes for brittle or quasi-brittle materials [48, 49].

The geometrical details of the bend specimens are depicted in Fig. 3.2(b,c). For the SE(B) with regular notch, two notch depths were chosen, a shallow one with $a_0/W = 0.35$ and a deep one with $a_0/W = 0.6$. Each notch had a narrow width of 0.07 mm, and was machined using a 50 μm spark-wire. Very sharp notches were obtained with this method. Fracture toughness was measured considering the sharp notch as a crack.

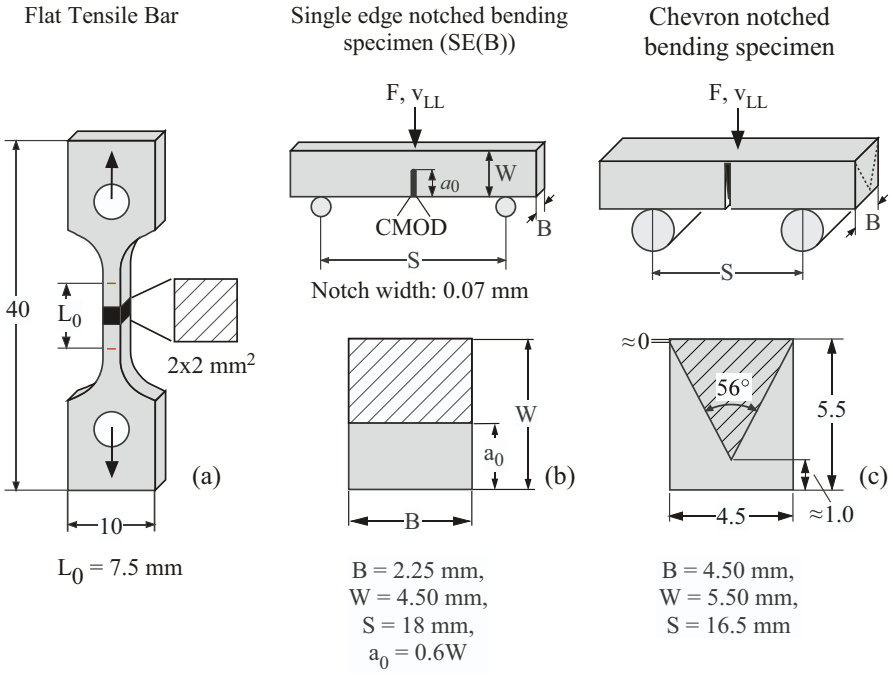

Figure 3.2: Geometries of the specimens: (a) flat tensile specimen, (b) single edge notched bend specimen (SE(B)), (c) chevron notched bend specimen.

3.2 Experiments and results: Tension tests

True stress-strain curves were determined from six tensile tests. The results are shown in Fig. 3.3. The calculated elastic modulus from the six tests is 175 GPa, which agrees with the data reported in literature [7].

The figure shows significant differences between the stress-strain (σ-ϵ) curves with respect to yield strengths, fracture stresses and strains. For specimens 4,5 and 6, the σ-ϵ -curves lie close to each other showing varying fracture strains. Specimens 1,2 and 3 show remarkable differences in σ-ϵ -curves and fracture strengths. All specimens fail within 0.9-1.5% strain, therefore, the alloy is reffered to as a 'quasi-brittle' material. From the curves the average failure strength was determined to be 750 MPa.

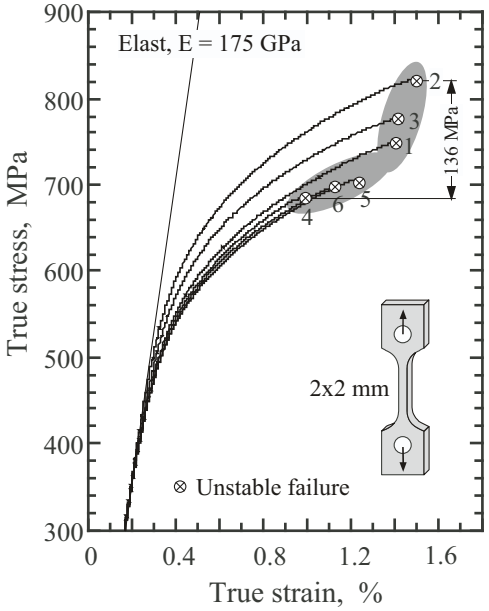

N°	Test	σ^{max}_{true} (MPa)	ε^{max}_{true} (%)
1	ZQ1	748.0	1.41
2	ZQ2	820.4	1.50
3	ZQ3	776.6	1.42
4	ZQ6	683.6	0.99
5	ZQ4	702.3	1.24
6	ZQ5	697.6	1.13

Figure 3.3: Stress-strain curves from the flat bar tensile specimens.

The variation of fracture stress and strain, and the shifting of the σ-ϵ curves are predominantly influenced by the colony structure and orientation. Due to the orientation angle with respect to the loading axis, a colony can deform easily (soft colony) or can show high stiffness (hard colony), eventually produces variation in stress-strain curves. As the orientation and the size of the colonies are not constant throughout the microstructure, each tested specimen has its own microstructural arrangement that differs from one another, resulting in different tensile results. The variation of the stress-strain behavior may also be influenced by some unwanted presence of different microstructural arrangements or phases. For example, the micrograph in Fig. 3.4 shows a significant presence of duplex like grain-clusters among the lamellar colonies. However, the presence of different microstructures and their influences on the experimental tensile behavior has not been investigated.

In the numerical analysis the above mentioned variations are implemented. Fracture strength has a lower limit of 683.6 MPa and an upper limit of 820.4 MPa. The number of tests is not enough to obtain a statistically reliable scatter band. However, the obtained variation band is quite similar to the variation band reported in the literature [14].

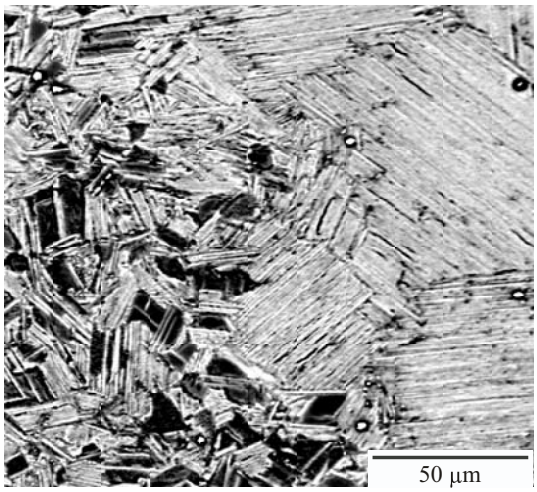

Figure 3.4: Microstructural inhomogeneity in fully lamellar γTAB observed from the extruded rod. Some duplex grains are found along with the lamellar colonies.

3.3 Experiments and results: Bend tests

3.3.1 SE(B) specimens with straight notches

The bend tests were carried out with a screw driven test machine at room temperature, from which the force, F, and the crack mouth opening displacement, CMOD, were measured. The resulting F-CMOD curves for two different notch depths are depicted in Fig. 3.5(a).

For the case of the notch depth ratio, $a_0/W = 0.35$, all specimens failed catastrophically after the initiation of cracks showing small nonlinear deformation. On the other hand, deformation controlled crack propagation was observed for the deep notch, $a_0/W = 0.6$. Significant scatter in the softening part of the F-CMOD curves was found. In addition, the specimens also showed large pop-ins before catastrophic failure.

The translamellar crack propagation for $a_0/W = 0.6$ notch depth can be seen in Fig. 3.5(b). Evidence of local crack deflection and crack bridging can be seen in the figure. Fig. 3.5(c) gives a closer view of the translamellar fracture across a colony which broke along the $\{111\}_\gamma$-plane. The global force-deformation behavior due to different notch depth ratios can be recognized easily from Fig. 3.5(a). A shallow notch promotes uncontrolled crack propagation (or unstable failure) earlier than a deeper notch.

3.3.2 SE(B) specimens with chevron notch

Eight fracture experiments were performed on chevron notched bend specimens, and the force, F, was plotted against the load-line-displacement, v_{LL}, see Fig. 3.6. Some nonlinear deformation with minor or larger crack extensions can be observed for all cases, however, all the specimens failed

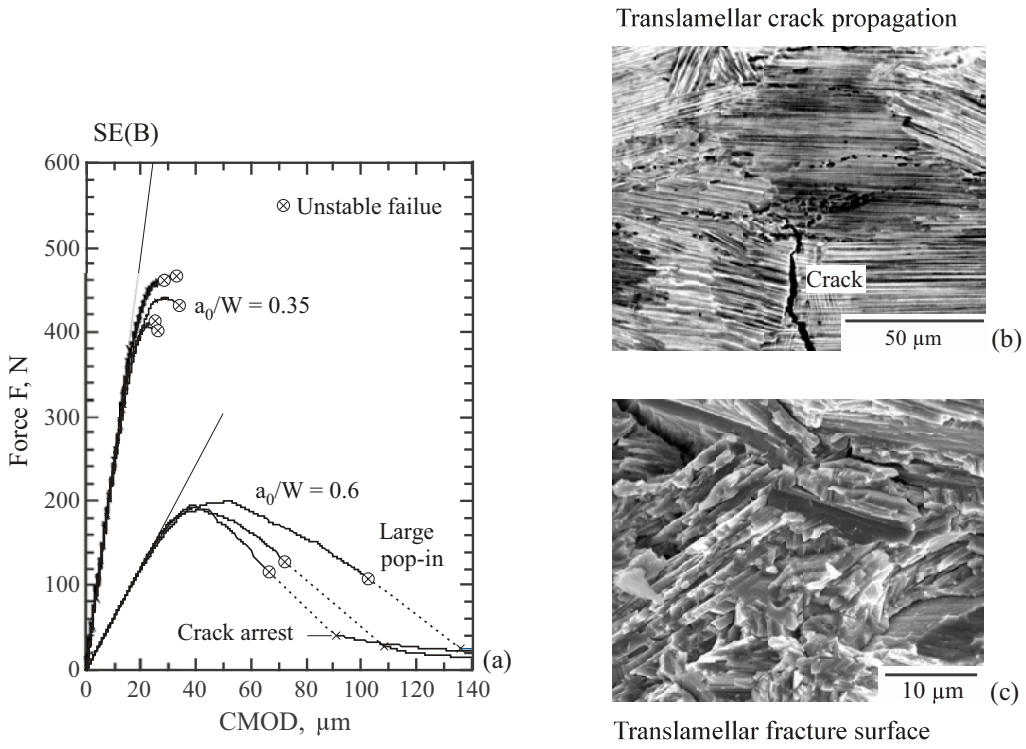

Figure 3.5: SE(B) specimens: (a) F-CMOD behavior for shallow and deep notches, (b) translamellar crack propagation, (c) high resolution of the translamellar fracture surface.

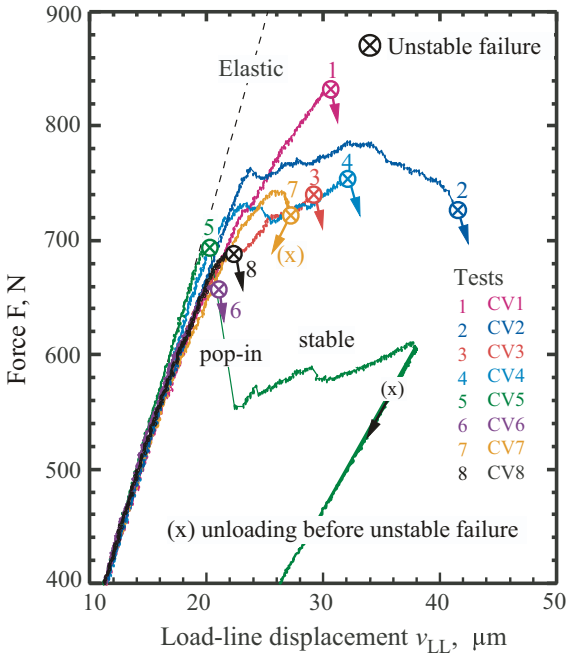

Figure 3.6: Chevron notched bend specimens: force vs. load-line-displacement behavior.

abruptly showing unstable crack propagation. Minor pop-ins are discernible from the F-v_{LL} curves. Tiny saw-teeth trends can be detected on the curves. These were generated from the step-wise crack

propagation through the lamellar colonies. In some cases significant load-drops (or big pop-ins) are observed after the initiation of cracks, followed by uncontrolled crack propagation. For example, the specimens CV1, CV6, CV7, and CV8 failed just after the onset of significant pop-ins. The other cases, for example, in specimens CV2, CV4, and CV5, deformation controlled crack propagation has been observed, which proceeded in a continuous manner up to a certain limit showing smaller pop-ins.

The experimental F-v_{LL} curves differ from each other in terms of fracture initiation, pop-in phenomena, crack propagation and subsequent failure.

3.4 Fractography analysis

Fracture surfaces of the Chevron notched bend specimens have been analyzed for a better understanding of the experimental scatter in the F-v_{LL} data. Three F-v_{LL} curves from the specimens CV1, CV2, and CV5 respectively are examined in correlation with the fracture surfaces. It was found that the variation in the F-v_{LL} curves were influenced by the microstructure at the notch tip.

In specimen CV1, the translamellar fracture continued up to a crack extension of 1.04 mm until finally abrupt failure occurred due to unstable crack propagation, see Fig. 3.7. The cleavage facets in Fig. 3.8 indicates that the initiation of cracks at the notch tip was followed by interlamellar fracture along $\{111\}_\gamma$ planes. The crack front advanced through different oriented lamellae, since many of the $\{111\}_\gamma$ planes were ideally positioned to promote microcracking. As a result a jagged fracture surface was obtained.

In this type of polycrystalline alloys, tilting of the lamellar colonies with respect to the loading axis is an important mechanism during the cracking process. A schematic drawing of the crack path, with and without tilting of a colony is shown in Fig. 3.9.

An image of the specimen CV2 is shown in Fig. 3.7. Observations indicate a homogeneous translamellar fracture through the randomly oriented colonies. Deformation controlled crack propagation is observed up to a large global displacement. All the colonies broke in a purely translamellar manner. No cleavage facets of interlamellar type fracture have been found (see CV2 in Fig. 3.8). Further translamellar fracture occurred without significant pop-ins. The crack propagation was ensured by the small tilting angles of the colonies with respect to the loading axis.

In Fig. 3.7 and Fig. 3.8, the notch tip of the specimen CV5 is shown. Here, the lamellar orientation of the first colony at the chevron notch tip is almost perpendicular to the loading direction. The initial crack propagation was due to the interlamellar fracture along the inclined lamellar planes, as indicated in Fig. 3.8. As a result a large pop-in can be observed on the respective F-v_{LL} curve. The crack jumped forward, but was arrested by stiffer colonies on its fracture path, leading to a stable deformation controlled crack propagation.

The crack initiation in the triangular chevron notch is strongly regulated by the notch tip microstruc-

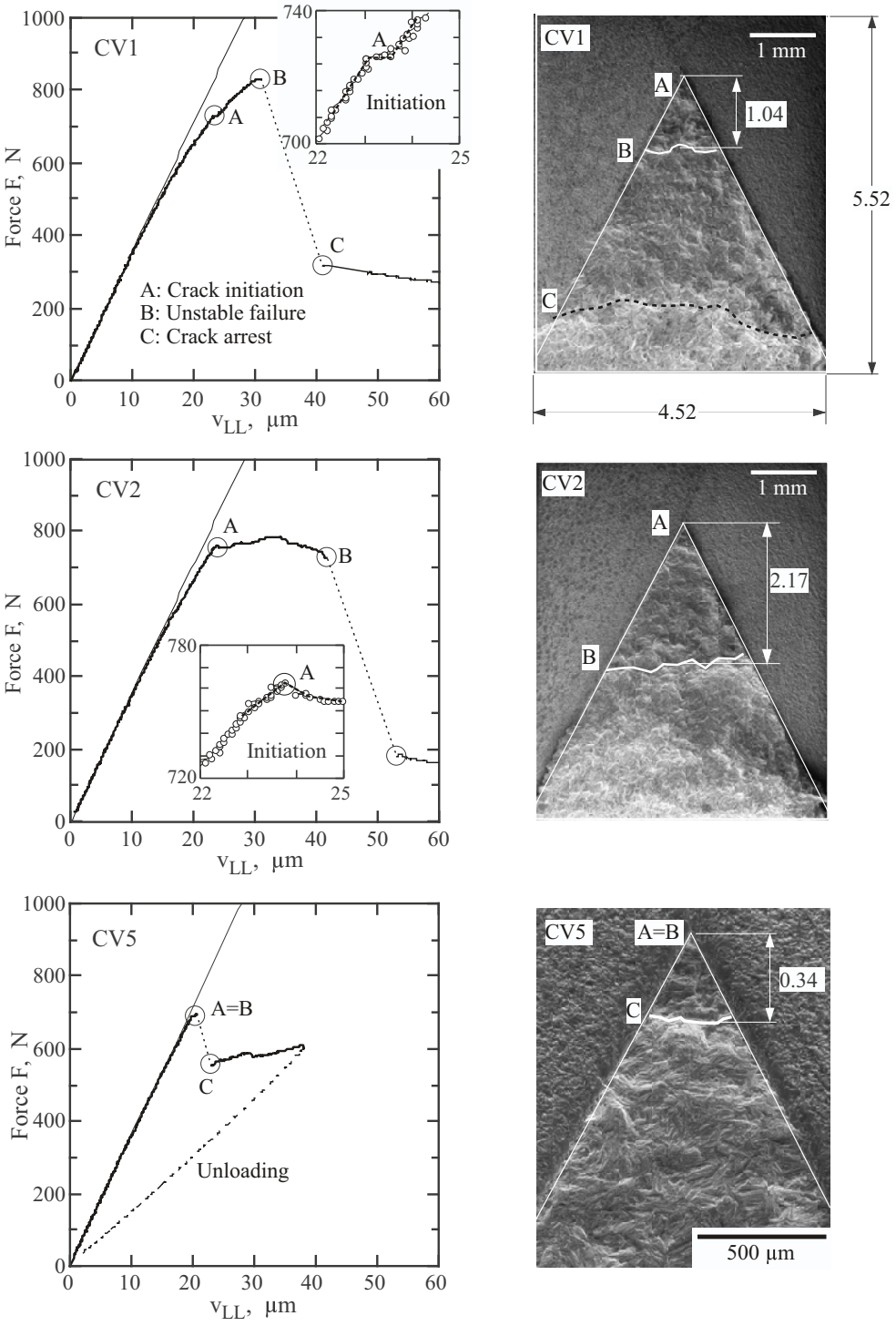

Figure 3.7: Different characteristics in the F-v_{LL} curves of the chevron notched bend specimens with fractography images.

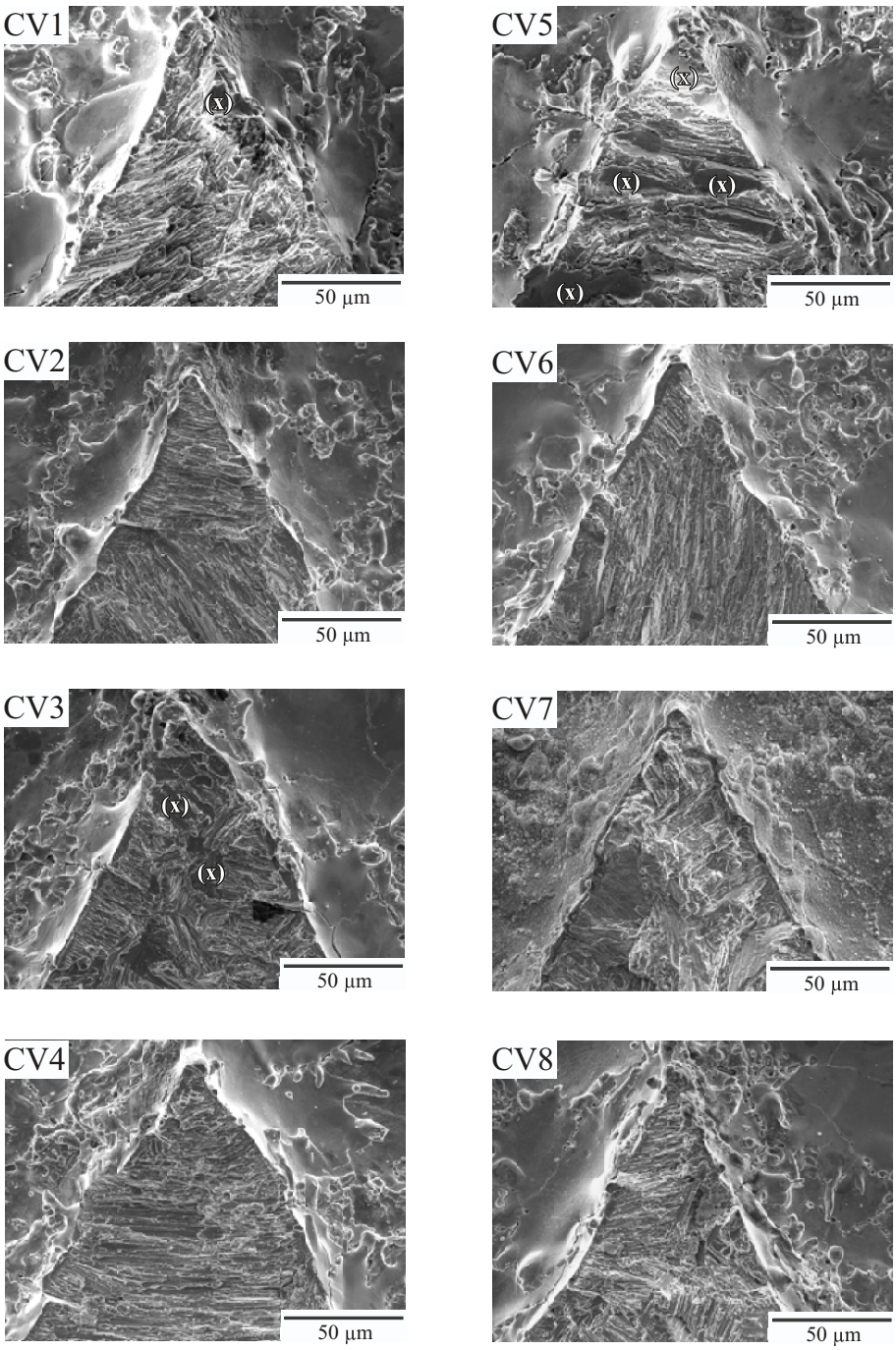

(x) Intelamellar fracture sites

Figure 3.8: Fracture surfaces close to the chevron notch tip of all tested chevron specimens (CV1-CV8).

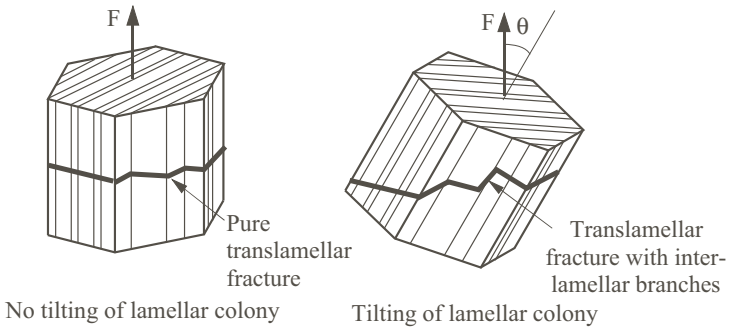

Figure 3.9: Schematic of the crack path through lamellae with different orientations to the loading axis.

ture. Different oriented and tilted colonies at the notch tip are discernible from the pictures in Fig. 3.8. The tilting angles of these colonies aid further propagation of the cracks along the $\{111\}_\gamma$-planes.

As stated in [50], the fracture toughness for lamellar γTiAl varies within a certain range depending on the lamellar orientation. The degree of variation depends on the amount of interlamellar and translamellar fracture which are promoted by the orientations of the colonies [51]. As reported in [52, 53], the fully lamellar microstructure delivers a fracture toughness, K_{Ic}, in the range of 20-37 MPa $\sqrt{m}$ for translamellar fracture while the interlamellar fracture toughness of the lamellar $\{111\}_\gamma$ planes is very low, about 1-3 MPa $\sqrt{m}$ [18, 52].

Chapter 4

Numerical approaches of fracture mechanics

4.1 Background

Components and structures are not free of defects that may lead to catastrophic failure under operating conditions. Among the defects, the presence of sharp cracks is the most critical one from which fracture may start. Fracture mechanics establishes a guidance to avoid component failure assuming that the engineering materials always contain cracks. Under the fracture mechanics theories, the extension of cracks in a material is characterized by material related parameters. The material parameters and the laboratory test results can be correlated, by which the response of a structure containing cracks can be predicted.

The continuum mechanics approach to fracture assumes that the material is a homogeneous continuum and that the defects are large compared to the characteristic dimensions of the microstructure. To study the growth of existing cracks, voids or other defects, stress analyses are performed in combination with some postulates that predict occurrence of fracture. Two important issues have to be considered for characterizing the fracture, firstly, information that provides a correct and physically meaningful picture of the processes occurring at the crack tip and secondly, description of the fracture toughness (which is the critical value of crack driving force) of a material in a specific structural geometry. The both issues are taken care of in the fracture models using phenomenological or micromechanical based descriptions.

The computational fracture mechanics approaches were developed based on the fundamental ideas of the strength reduction of materials, provided by Griffith and Irwin. Griffith proposed the energy criterion of fracture in 1920. According to him, when a solid is fractured, work is performed to create new material surfaces in a thermodynamically irreversible manner. He considered that the brittle materials contain microcracks, which introduce high stress concentrations near their tips. He developed a relationship between crack length, fracture surface energy to generate traction-free cracked surfaces,

and applied stress [54].

In Griffith's theory, the work of fracture is spent in the rupture of cohesive bonds, which is valid for pure elastic material. The fracture surface energy, which represents the energy required to form a cracked surface, corresponds only to the normal separation of atomic planes. The dissipation energy associated with nonhomogeneous slip within and between the grains as well as plastic, viscous deformation, etc. are not considered. The energy required for the rupture of atomic bonds is only a small portion of the total dissipated energy during fracture.

For the "somewhat brittle material", Irwin provided an extension of Griffith's theory. He stated that a region of plastic deformations may exist closer to the crack but does not extend away by more than a small fraction of the crack length [55]. This is known as the "small-scale yielding condition". He proposed the concept of the stress intensity factor, K as a criterion of crack initiation, that can be related to the strain energy release rate. The critical value of the stress intensity factor, K_c, is geometry independent, and represents the material property commonly known as fracture toughness.

The fracture in brittle or quasi-brittle material can be characterized using the Griffith and Irwin's theory of fracture, however, the approaches lose their validity when the material shows large scale yielding. The development of fracture mechanics since 1960 focused on capturing large scale yielding in fracture analysis, which is known nowadays as elasto-plastic fracture mechanics (EPFM). Two well known approaches are the "J-integral" [56] and the crack-tip-opening-displacement, CTOD [57]. The "J-integral"approach expresses the energy release rate as a path independent line integral, while the crack-tip-opening-displacement approach correlates the amount of crack tip plastic strain to the separation of the crack faces. Standard test methods are available to determine these fracture mechanics parameters.

In structural analysis, the maximum sustained load of a cracked component can be described in terms of single parameters of fracture, such as, K_c, J_c or $CTOD$. The approach is known as the global approach of fracture mechanics. This approach has certain restrictions, for example, it does not provide any prediction of size effects observed in brittle fracture nor can it be applied where non-isothermal loading conditions are active. Moreover, an existing crack is necessary for the analysis. Recent developments of the "local approach to fracture"are not limited to these restrictions. Two conditions have to be fulfilled for the local approach: (i) micromechanical based models must be established that describe the softening effects by the constitutive equations of damage evolution; (ii) a good understanding of the crack tip stress-strain field has to be developed. Numerical formulations of micromechanical models for computer implementations are necessary for this approach. The approach introduces new parameters which have to be experimentally determined.

A suitable way of analyzing the structural fracture is to describe the physical damage processes phenomenologically within a model. The cohesive model (also known as cohesive zone model, CZM) is such a model that describes various kinds of decohesion processes by relating the surface tractions (or cohesive stress, T) to the process of material separation, δ. The idea of a "strip yield model"proposed by Dugdale [58] and Barenblatt [59] can be considered as the foundation of the cohesive model. Dug-

dale and Barenblatt divided the crack in two parts: one part is the stress free crack surfaces, the other part is the one loaded by cohesive stresses. Dugdale introduced the finite stress to be the yield stress, which holds only for plane stress conditions. Barenblatt assumed that the stresses in the fracture process zone follow a prescribed distribution of σ(x), where x is the ligament coordinate. The cohesive models and the "strip yield model"differ from the idea of Barenblatt in that the traction acting on the ligament is a function of the crack opening, i.e., T(δ), and not of the distance from the crack tip.

The cohesive model allows fracture analysis beyond the restrictions of single parameter based global approaches to fracture. It also has certain advantages over the local continuum models of damage, for example, it does not show pathological mesh dependency and does not require the introduction of a length parameter via the FE mesh. Its implementation to the finite element method enables one to analyze complicated structures numerically. The cohesive model will be used in the present work and its fundamentals are described in the next section.

4.2 The cohesive model

In front of the crack tip a small zone exists where micro-cracking takes place and damage occurs at increasing deformation. This process is described by an increase of stress (or traction, T) up to a certain maximum level followed by a decrease of active stresses to zero until the material totally separates. The relationship of the traction, T, and the separation, δ, is described by a function called the traction-separation law (TSL). Propagating crack is simulated by the separation process that generates free surfaces along a predefined plane. The region where evolution of damage occurs is called the fracture process zone (FPZ). The maximum value of traction, which is the cohesive strength, T_0, and the critical separation, δ_0, are the material related parameters.

The basic idea of the cohesive model is depicted in Fig. 4.1(a,b). In the finite element simulation the fracture process zone is idealized as a perfect plane and is referred to as the fracture plane. The cohesive elements (which are basically zero thickness interface elements) are introduced between the continuum elements at the fracture plane (Fig. 4.1(b)). Each cohesive element follows a predefined TSL. When the cohesive separation, δ, along the interface exceeds a maximum separation, δ_0, at the cohesive element nodes, the stress transmission reduces to zero, and the crack extends up to the respective element size.

The shape of the TSL can be generated by various functions. In literature, several TSL-functions can be found: linear, constant, exponential, and bilinear functions, see Fig. 4.2. For pure normal separation in ductile materials, Needleman [60] first introduced a polynomial function. Tvergaard [61] extended the polynomial function for mixed mode fracture. For brittle like materials, for example, concrete and rocks, Hillerborg [62] used a purely decreasing linear function.

The TSL controlling the separation process is purely phenomenological. No successful test method exists to measure the TSL function directly [66]. Therefore, the shape sensitivity of the TSL with

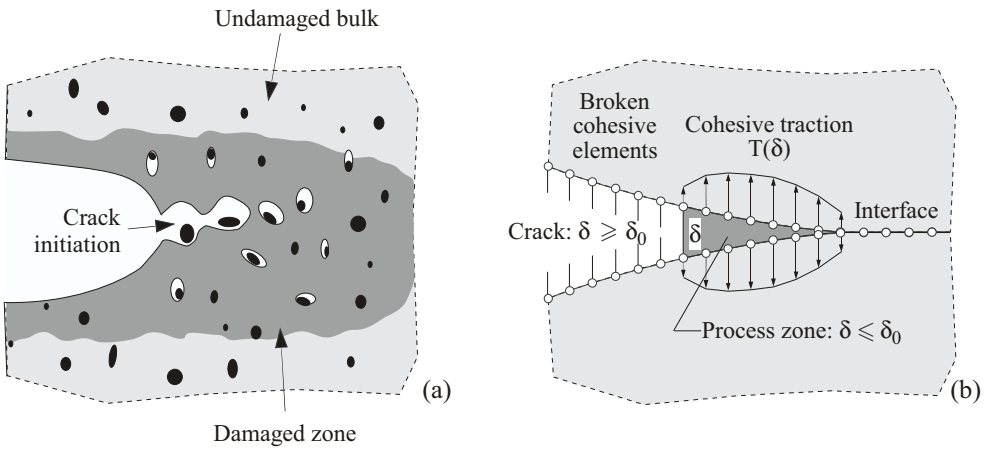

Figure 4.1: Crack evolution in a bulk material: (a) realistic presentation of damage by void growth, (b) idealization by the cohesive model.

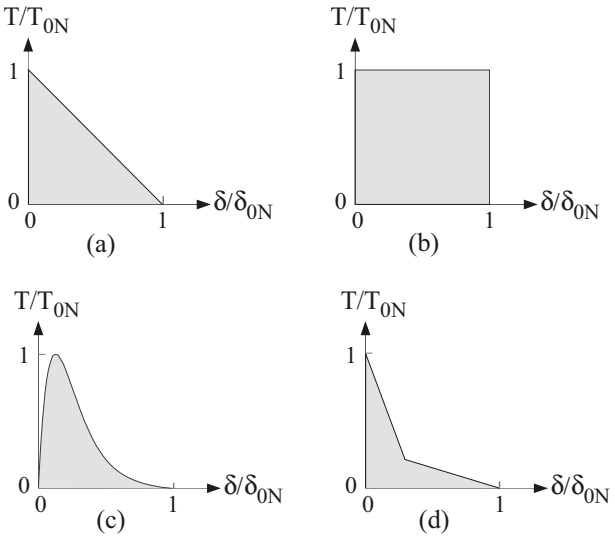

Figure 4.2: Cohesive traction-separation laws (TSL) for normal fracture: (a) linear [62], (b) constant [63], (c) polynomial [64], (d) bilinear [65].

respect to the particular fracture phenomenon, like quasi-brittle or ductile has to be investigated.

In this investigation, concerning the quasi-brittle fracture of γTiAl alloys, the following TSL is used as proposed in [67, 68]:

$$T = T_0 \begin{cases} 2\left(\dfrac{\delta}{\delta_1}\right) - \left(\dfrac{\delta}{\delta_1}\right)^3 & \text{for} \quad \delta \le \delta_1 \\ 1 & \text{for} \quad \delta_1 < \delta \le \delta_2 \\ 2\left(\dfrac{\delta - \delta_2}{\delta_0 - \delta_2}\right)^3 - 3\left(\dfrac{\delta - \delta_2}{\delta_0 - \delta_2}\right)^2 + 1 & \text{for} \quad \delta_2 < \delta \le \delta_3 \end{cases} \tag{4.1}$$

The shape of the TSL function can be arbitrarily varied from a rectangular to a nearly triangular one

by using two extra parameters, δ_1 and δ_2, as shown in Fig. 4.3. The parameters are correlated to the maximum cohesive separation, δ_0, such that $\delta_1 = 0.001\delta_0$ and $\delta_2 = 0.75\delta_0$ in the case of the nearly rectangular function, while for the triangular one $\delta_1 = \delta_2 = 0.001\delta_0$. The two TSL functions will be denoted as Rect-TSL and Tria-TSL.

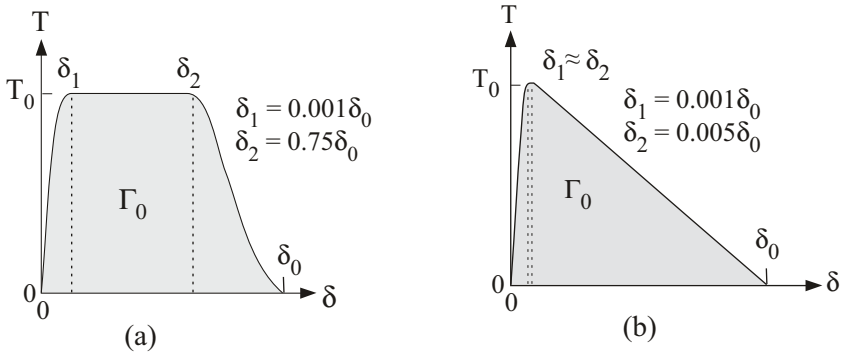

Figure 4.3: Cohesive traction-separation law used in this investigation: (a) Rect-TSL, (b) Tria-TSL.

The area under the TSL curve is the separation energy, Γ_0:

$$\Gamma_0 = \int_0^{\delta_0} T(\delta)\, d\delta \tag{4.2}$$

The critical separation, δ_0, is related to the separation energy, Γ_0, as follows:

$$\delta_0 = \frac{2\Gamma_0}{T_0\left(1 - \frac{2}{3}\frac{\delta_1}{\delta_0} + \frac{\delta_2}{\delta_0}\right)} \tag{4.3}$$

The parameters T_0 and Γ_0 can be determined by experimental means in certain cases or by supplementary use of experiments and simulations. For brittle or quasi-brittle materials, the cohesive strength, T_0, can be experimentally determined as the maximum true stress at fracture from the tensile tests, provided that no ductile necking develops before reaching the maximum stress. Otherwise, for ductile materials with significant necking before fracture, cohesive strength can be determined from elastic-plastic FE calculations. The separation energy, Γ_0, is equal to the critical value of the *J*-integral at physical crack initiation. Therefore, by means of standard fracture mechanics tests with pre-cracked bending specimens, Γ_0 can be determined. In order to find the cohesive parameters numerically, the stresses, the strains, and the crack initiation during increasing deformation need to be correlated with the experimental observations.

Determining a reliable value of the critical cohesive separation, δ_0, needs a large amount of experimental work, however, it can be derived from the cohesive energy, Γ_0, as given by the relationship in Eq. (4.3).

In the present work, the critical fracture stress or the fracture strength will be taken as the cohesive strength, T_0. The cohesive energy, Γ_0 will be determined using a hybrid methodology of experiments and simulations. The δ_0 values are calculated from Eq. (4.3).

For a homogeneous material, the separation along the crack path can be described by a single set of T_0 and δ_0. For a heterogeneous material, cohesive parameters along the crack path are not constant but vary according to the microstructural heterogeneity. Such a crack path can be described by the random values of T_0 and δ_0 which will result in a stochastic nature of crack initiation. Random values of T_0 and δ_0 will be distributed using a simple distribution function described in the next section. Further aspects of fracture, like crack branching, crack deflection, and the interaction of different fracture modes (normal and shear modes) are still the subject of discussion and will not be implemented in the cohesive model.

4.3 Stochastic approach

The random material properties and the distribution in the microstrucutre are handled with a stochastic approach. From the experimental data and fractography of a fully lamellar γTAB, the following property variations were found:

1. Variation of the fracture strength and toughness properties:

   Random orientation of lamellar colonies and their tilting angle with respect to the loading axis provide certain local variations in fracture strength and toughness. These properties are related to the cohesive strength, T_0, and cohesive energy, Γ_0. Stochastic variation can be adopted in the FE model by stochastic distributions across the cohesive elements lying on the fracture plane.

2. Variation of the local deformation behavior of the polycolonies:

   In polycrystals with differently oriented lamellar colonies, inhomogeneous stresses and deformations occur locally. The deformation behavior of the colonies can be expressed by local $\sigma-\epsilon$ curves. The variation of such microscale $\sigma-\epsilon$ curves can be determined from a crystal plasticity model which incorporates the descriptions of microstructure and micromechanisms of deformation within a lamellar colony.

For the finite element implementation the variable σ-ϵ-curves are used for the continuum element deformation behavior and the T_0, Γ_0 are used for the separation of cohesive elements, see Fig. 4.4 for a schematic representation. Both types of variations should be taken into account in the global fracture simulation of γTAB.

In the simulation of fracture, crack initiation takes place when the nodal separation of a cohesive element increases beyond the critical separation, δ_0. A low T_0 combined with a high Γ_0 provides a large δ_0, while a high T_0 combined with a low Γ_0 results in a low δ_0 (shown schematically in Fig. 4.4, bottom). Random variation of the two cohesive parameters, T_0 and Γ_0 produce discrete values of the maximum cohesive separation, δ_0, resulting in random nature of crack initiation. As the Γ_0 and δ_0 are analytically related (see Eq. (4.3)), either the variation of Γ_0 or the variation of δ_0 can be stochastically chosen. In this work Γ_0 is used as a random parameter as it can be verified from the fracture tests with

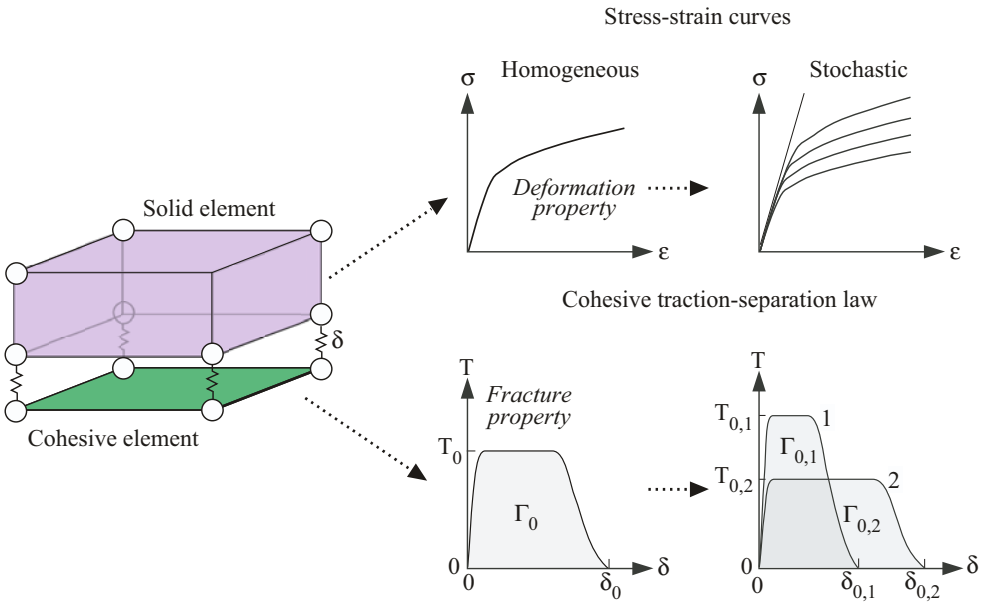

Figure 4.4: Stochastic approach considering property variations in the continuum (3D solid elements) and fracture plane (cohesive elements).

less effort. For numerical analysis, the random values of δ_0 corresponding to the random values of Γ_0 are given as an input in the FE model.

The following two undefined phenomena have to be taken care of for the numerical implementation of the stochastic parameters:

- The variation band of the microstructural related parameters (σ-ϵ, T_0 and Γ_0).
- The frequency distribution function of the parameters.

The variation band for the $\sigma-\epsilon$ curves can be determined using a polycrystal model. However, the microstructural fracture parameters in a polycrystal can not be easily obtained by the available experimental techniques. Therefore, the variation band of the fracture strength, T_0, is taken from the fracture point of the global stress-strain curves, which may be smaller than the real scatter. Generally, microstructural scatter is assumed quite big in heterogeneous materials, however, no exact variation band of the scatter can be determined.

In the present analysis, a uniform distribution [69] of all parameters is considered as a first approximation. Fig. 4.5 shows an arbitrary Weibull density distribution as well as the rectangular distribution function for the assumed microstructural properties. Using the rectangular distribution function the cohesive parameters are equally distributed across the fracture plane. Therefore, all parameters have equal importance or weight to initiate cracks.

To investigate the influence of parameter distribution further frequency distribution is assumed, see Fig. 4.6. In the first assumption (Fig. 4.6b), the chosen microstructure is such that the lower value

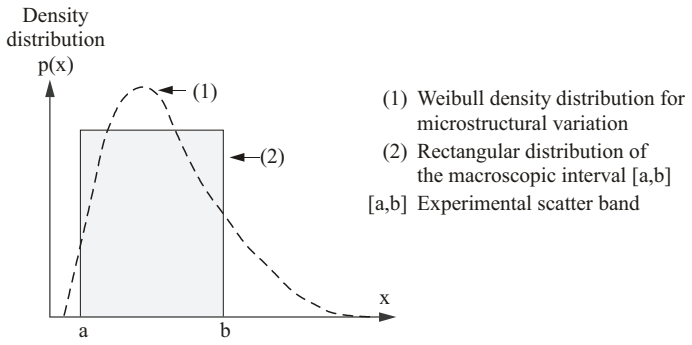

Figure 4.5: Stochastic distributions for the Weibull density function of local properties e.g., fracture strengths and the uniform distribution as used in the stochastic approach of cohesive model.

of the properties occur more often than the higher ones. In the second assumption (Fig. 4.6c), the opposite is assumed. In the third microstructural assumption (Fig. 4.6d) the average values of the material properties are more prevalent. Properties like stress-strain, fracture strength and fracture toughness may follow one of the above histograms.

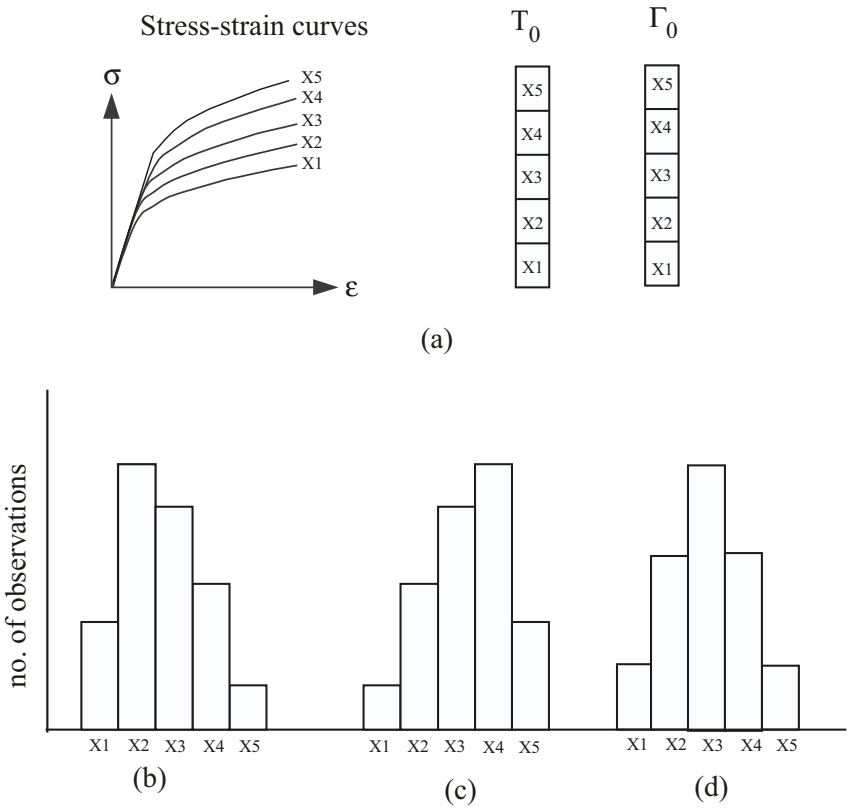

Figure 4.6: Frequency distributions of material properties.

With the proposed variation bands and assumed frequency distributions, a successful validation of the cohesive model is expected. A detailed description of the investigation will be provided in Chapter 6.

4.4 The FE model

The FE models were generated with 3D geometry using 8-node brick elements. An appropriate mesh coarsening technique was implemented to restrict the size of the model with respect to the number of elements and nodal degrees of freedom. In order to generate a fracture surface, fine regular meshes were produced across the fracture plane, where cohesive elements were attached. For a homogeneous material, the fracture was simulated by attributing a single set of cohesive parameters along the fracture plane. Maximum cohesive separation, δ_0, was the same for each cohesive element. The elastic-plastic behavior of the continuum element is described by the average stress-strain curve obtained from the tensile experiments. On the other hand, fracture in a heterogeneous material is simulated by allocating stochastic values of T_0 and δ_0 (derived from the cohesive energy, Γ_0) along the fracture plane. To capture the heterogeneous deformation of the lamellar colonies, an additional distribution of stress-strain curves is applied in a small region of continuum elements above the cohesive layer. Due to inhomogeneous deformation of the continuum elements nearby the cohesive layer, an inhomogeneous stress field along the fracture plane will develop, which may influence the crack initiation.

In order to simulate global deformation and fracture behavior of lamellar γTAB, some assumptions are made in the FE model. The colonies of the γTAB are simplified as cubic blocks of continuum elements with a constant value which is equal to the average size of the real colonies (ca. 100 μm). The mechanical behavior of a colony is simulated by assigning local $\sigma-\epsilon$ curves to the respective continuum block. Each continuum block is attached to a cohesive block, at which cohesive parameters are randomly assigned.

The effect of colony orientations on the fracture is described by the higher and lower fracture parameters. For example, a favorably or non favorably oriented colony that produces a lower or higher fracture toughness during crack propagation is described by a set of cohesive parameters with lower T_0 and Γ_0, or higher T_0 and Γ_0. A colony's deformation behavior is described by a lower σ-ϵ-curve for a weak colony and a higher σ-ϵ-curve for a strong colony.

The real microstructure and its cohesive model idealization including the stochastic aspects are shown schematically in Fig. 4.7(a,b). Colonies are depicted as cubic blocks with randomly distributed σ-ϵ-curves. Random cohesive parameters, T_0 and Γ_0 (resulting from different oriented colony fractures) are applied to the cohesive blocks.

The cohesive element size should be related to the maximum separation, δ_0, which can be correlated to the different lamellar microstructure [70]. Cohesive elements which are an order larger than δ_0 are avoided as the larger elements create problems during numerical crack propagation, or provide mesh dependent results.

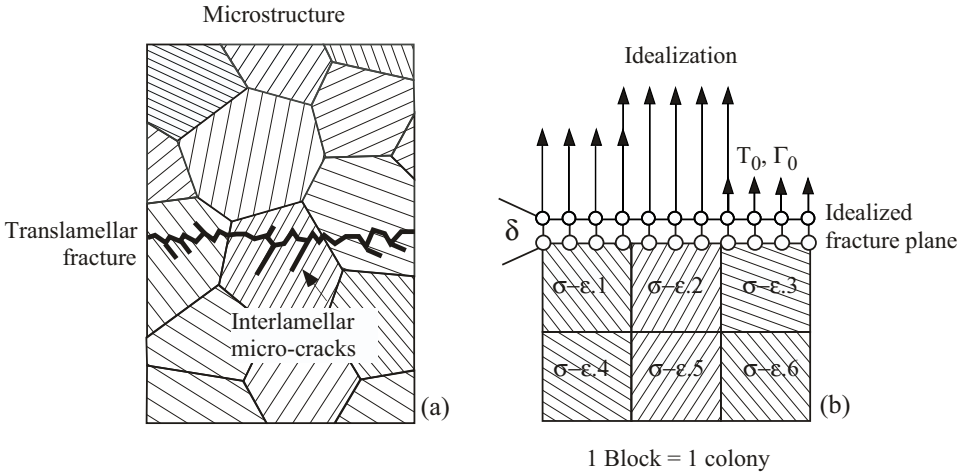

Figure 4.7: Lamellar microstructure of γTiAl: (a) realistic microstructure drawing, (b) idealization with a stochastic approach using the cohesive model.

Chapter 5

Studies on the cohesive model for quasi-brittle fracture simulation

From a macroscopic point of view the fracture may roughly be classified as ductile and brittle. Typically, a large amount of plastic deformation takes place during ductile fracture. The crack propagates in a controlled manner with the increased deformation (i.e., stable crack propagation). On the other hand, little or no plastic deformation occurs during brittle fracture and merely a controlled crack propagation can be observed. The material fails abruptly just after the crack initiation or after a little stable crack propagation. Ductile or brittle characteristics of the material can be distinguished from the experimental observations by their force-displacement behavior, crack initiation, and crack propagation. The phenomena should be taken into account during parameter identification of the cohesive model.

In the present chapter the influence of the model parameters, T_0 and Γ_0, on the load-displacement behavior, crack initiation, and propagation is investigated numerically. A 2D FE model for plane strain will be used.

5.1 Study of the TSL shape for quasi-brittle material

The shape of the TSL was varied from rectangular to triangular by changing the shape parameters, δ_1 and δ_2. The Rect-TSL and Tria-TSL have been already shown in Fig. 4.3 in Chapter 4. The parameter, δ_1, was taken such that the first part of the TSL has a steep slope ($\delta_1 = 0.001\delta_0$). In the case of γTAB it was set to $0.001\delta_0$. The second shape parameter, δ_2, was changed from $0.005\delta_0$ to $0.75\delta_0$ to obtain a gradual shift from a nearly triangular to a nearly rectangular shape. Influences of the TSL were studied by setting $\delta_2 = 0.005\delta_0$, $0.1\delta_0$, $0.4\delta_0$, $0.6\delta_0$, and $0.75\delta_0$. The average failure strength of the tensile experiments was taken as the cohesive strength, $T_0 = 750$ MPa. The cohesive energy, Γ_0, was set to 3 N/mm, which is an approximate value obtained from the fracture tests of bending specimens.

The simulations were performed on a single edge notched three-point bend specimen (SE(B)). A 2D FE model of the SE(B) was generated with a notch depth ratio of $a_0/W = 0.6$, as shown in Fig. 5.1.

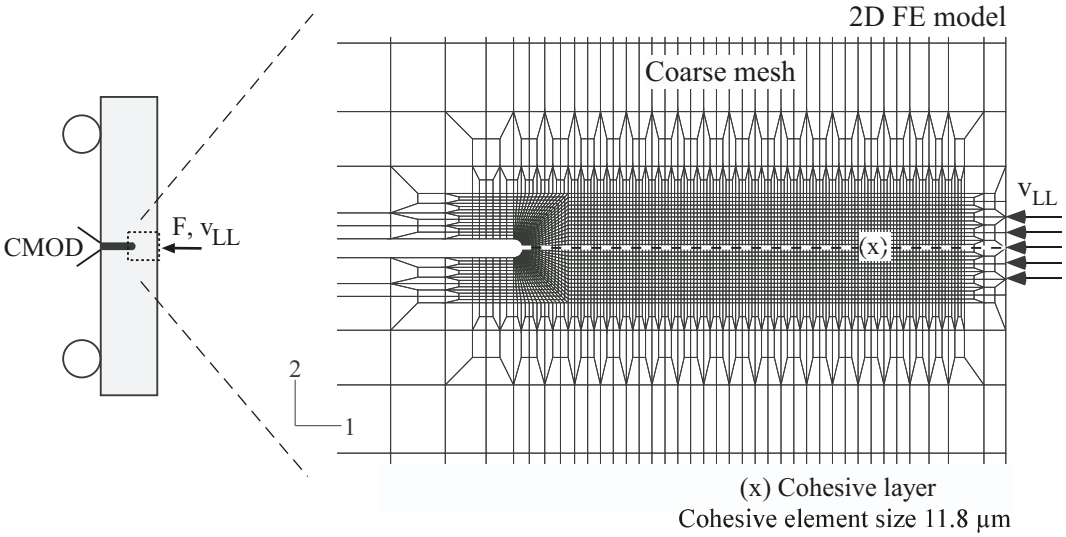

Figure 5.1: 2D FE model and the local mesh along the ligament of a SE(B) specimen.

The elastic-plastic properties for the FE model were derived from the average stress-strain response of the γTAB alloy tensile tests. The elastic modulus, E, is 175000 MPa and the Poison's ratio, ν, is 0.27. The simulation results are summarized below.

(a) Influence of the TSL-shape on the force-deformation (F-CMOD) behavior

Simulated F-CMOD curves are plotted for the TSL shapes, see Fig. 5.2(a,b). For the Tria-TSL ($\delta_2 = 0.005\delta_0$), a deformation controlled curve with quasi-static crack propagation was obtained, while for the Rect-TSL ($\delta_2 = 0.75\delta_0$) the curve stopped at the maximum load just at the onset of a cohesive element break. The softening parts of the curves coincide with each other irrespective of the TSL-shapes, which implies that after crack initiation the damage progresses in a same manner for all the cases.

The simulated F-CMOD curve for the Tria-TSL is smoothly rounded at the maximum force. With a sequential change of the TSL shape form triangular to rectangular, the F-CMOD curves sharpen gradually at the apex. For Rect-TSL the cracks initiated at the maximum where the F-CMOD curves ended. At this point no further stress equilibrium was obtained by the numerical solver and the calculation stopped. This phenomenon is interpreted as unstable condition of the specimen before sudden failure, which is equivalent to the experimentally observed sudden load drop.

To understand the influence of TSL-shapes on crack initiation and notch-tip stresses, evolution of cohesive strength along the crack path has been plotted, see Fig. 5.3(a). The notch-tip stresses are shown Fig. 5.3(b). For Tria-TSL, stresses in the cohesive elements at the notch-tip decrease gradually after $T=T_0$. Also, tractions in the cohesive elements away from the notch-tip increases same manner

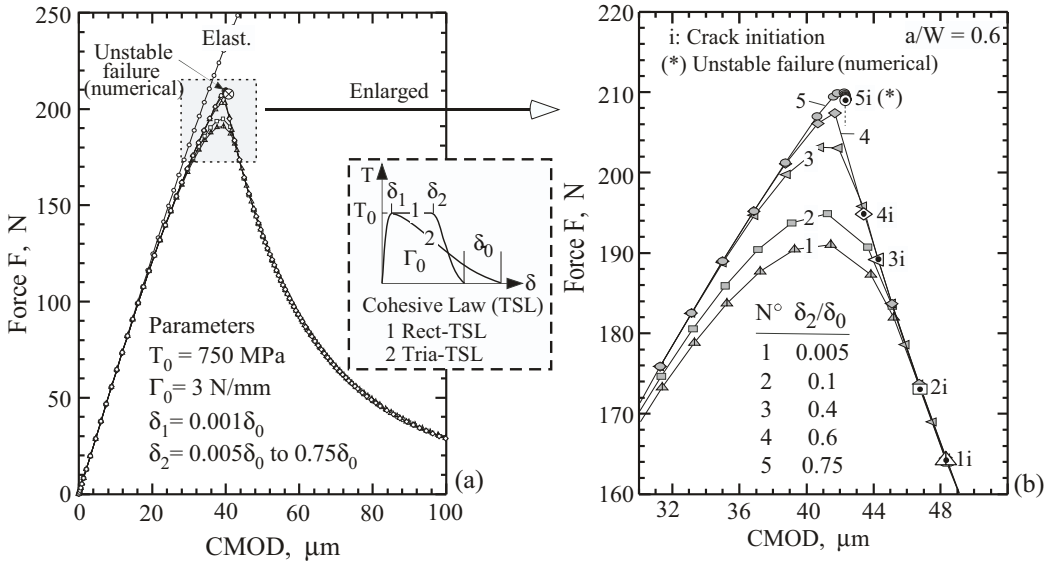

Figure 5.2: Influence of the TSL-shape: (a) F-CMOD curves, (b) enlarged window near the maximum load.

up to $T=T_0$. The gradient is very continuous during traction evolution which result in a stable crack propagation. The apex of the F-CMOD curve was rounded at the maximum due to the decreasing part of the Tria-TSL. Cracks initiate at the decreasing part of the curve which were fairly beyond the rounded peak.

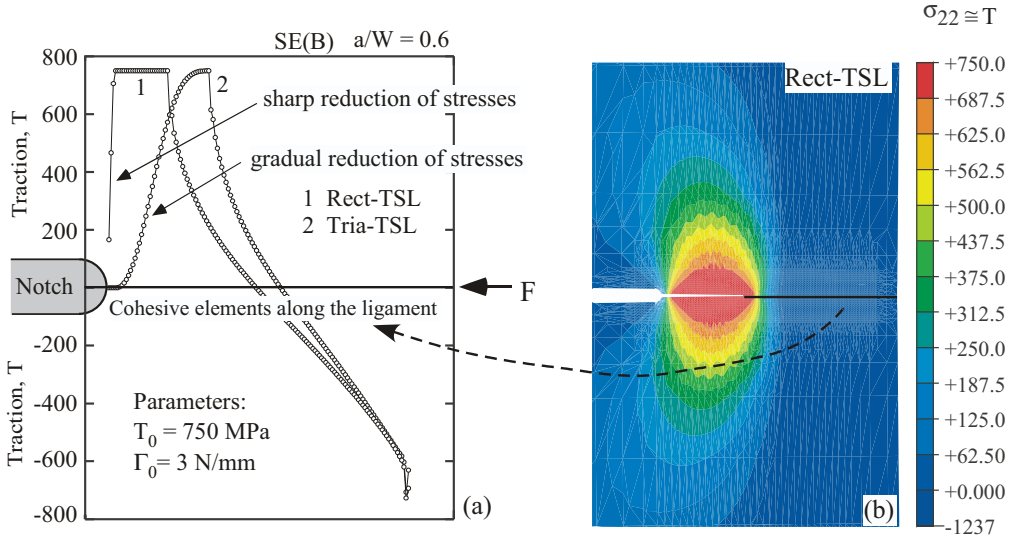

Figure 5.3: Stress (traction) distribution along the ligament: (a) comparison between the Rect and Tria-TSL, (b) normal stress distribution above the cohesive zone.

For Rect-TSL the maximum strength, T_0, is reached in a number of cohesive elements at the same time increment. Therefore, the maximum load can be higher compared to the Tria-TSL. In order to break a cohesive element, the material separation, δ, has to be extended up to δ_0. Due to the

steep slope of the third part of the Rect-TSL, a sharp strength reduction (high stress gradient) in several cohesive elements has been seen. The evolution of cohesive traction is similar to the stress evolution seen in brittle type fracture. For brittle type fracture, catastrophic failure results in sharp stress reduction, however, numerical modeling of quasi-static process can not capture such dynamic load-drop. At such unstable condition the calculations stop showing global equilibrium problem in the model.

The simulated force-deformation curves for the Rect-TSL that predict sudden failure are related to the material parameters (keeping the geometric configuration and loading condition fixed). With a higher Γ_0-value the Rect-TSL results in a deformation controlled stable crack propagation similar to the Tria-TSL. For example, taking Γ_0 = 10 N/mm, which is no longer related to γTAB alloy, a continuous F-CMOD curve was obtained, see Fig. 5.4. Deformation controlled crack propagation continued until the material totally collapsed. Due to the TSL characteristics the Rect-TSL yields a sharp peak near the maximum load while the Tria-TSL yields a rounded curve. The curves coincide somewhat beyond the maximum load. The results show the feasibility of Rect-TSL for simulating both stable crack propagation and sudden failure.

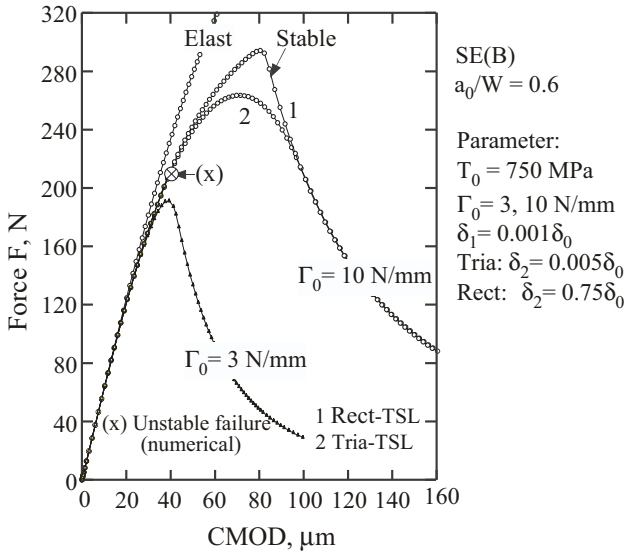

Figure 5.4: Influence of a higher cohesive energy, Γ_0 on the global response with the Rect-TSL.

(b) Influence of the TSL-shape on maximum load and crack initiation

In the numerical analysis a crack initiation is postulated when a single cohesive element at the notch tip has been separated. The crack initiation points observed from the simulated F-CMOD curves vary for different TSL shapes (see the magnified view in Fig. 5.2(b)). The transition of TSL shapes from Tria to Rect shifts the crack initiation points upward. For Tria-TSL the lower curve shows that the initiation of crack occurs significantly beyond the maximum load. The experimental observations of γTiAl exhibits that the initiation occurs at the maximum force showing small crack tip plasticity. This

crack initiation characteristic matches with the results of Rect-TSL.

(c) Remarks on choosing TSL for quasi-brittle fracture

It has been shown that the Tria-TSL always results in a stable crack propagation irrespective of the variation of fracture parameters related to γTiAl alloy. Experimental evidences rather prove an unstable nature of crack propagation. The analyses show that the Rect-TSL can capture both stable (deformation controlled) and unstable (not any more deformation controlled) nature of crack propagation depending on the cohesive parameters.

The Tria-TSL produces rounded maxima at the F-CMOD curves that look somewhat similar to the experimental observations. The rounded apex is, however, the result of the softening part of the Tria-TSL where no crack initiation has been found. On the other hand, the rounded maximums of the experimental curves are due to the initiation of microcracks in the colonies that soften the material at the notch tip. The results from the Rect-TSL showed that the F-CMOD curve softens just after the crack initiation which is more realistic than the Tria-TSL results. Therefore, a Rect-TSL is proposed for quasi-brittle fracture analyses.

5.2 Parameter study with 2D simulations

For a clear understanding of the physical significance of the cohesive parameters with respect to global fracture response the model parameters have been studied. The T_0 and Γ_0, have been varied and fitted with the experimental F-CMOD curves to check the parameter sensitivity. At first, the cohesive strength,T_0, was taken as 500, 750 and 1000 MPa, while the cohesive energy was set to an arbitrary higher value ($\Gamma_0 \ggg 1000$ N/mm). For a higher Γ_0, the maximum separation, δ_0, is larger. This allows no crack initiation within the global strain limit of γTAB alloy. The results are shown in Fig. 5.5, where the simulated curves are plotted along with the experimental curves. With the increase of T_0, the simulated F-CMOD curves shift to the elastic-plastic curve within this strain limit (shown by an arrow in Fig. 5.5). For T_0 = 500 MPa, the simulated curve deviates from the elastic slope earlier than the experimental one. For T_0 = 750 MPa, the initial part of the simulated curve matches the initial part of the experimental F-CMOD response quite good. For T_0 = 1000 MPa, the simulated curve became stiffer than the experimental curves. It can be seen that the experimental value T_0 = 750 MPa simulates the initial part of the experimental curve quite better.

In the second step, the strength, T_0 = 750 MPa, was kept fixed, and the cohesive energy, Γ_0, was changed as a free variable, i.e., Γ= 2.5, 3, 4, and 5 N/mm. The simulation results are shown in Fig. 5.6. With a finite Γ_0-value, a finite maximum separation, δ_0, was obtained. Crack initiated after reaching δ=δ_0. Due to different crack initiation points for different δ_0 values, the curve 5 in Fig. 5.6 was cut at some points.

Both stable and unstable crack propagations were obtained by varying the Γ_0 value. For all Γ_0 values

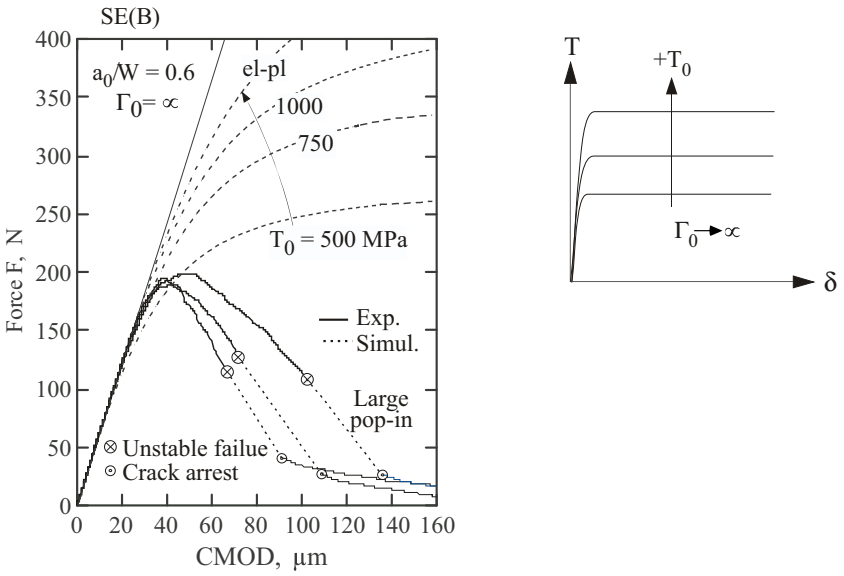

Figure 5.5: Influence of T_0 on F-CMOD response of the γTAB alloy considering no crack initiation.

sharp apexes at the maximum load were observed. The sharp apex in the simulated F-CMOD curve is the intrinsic characteristic of the Rect-TSL.

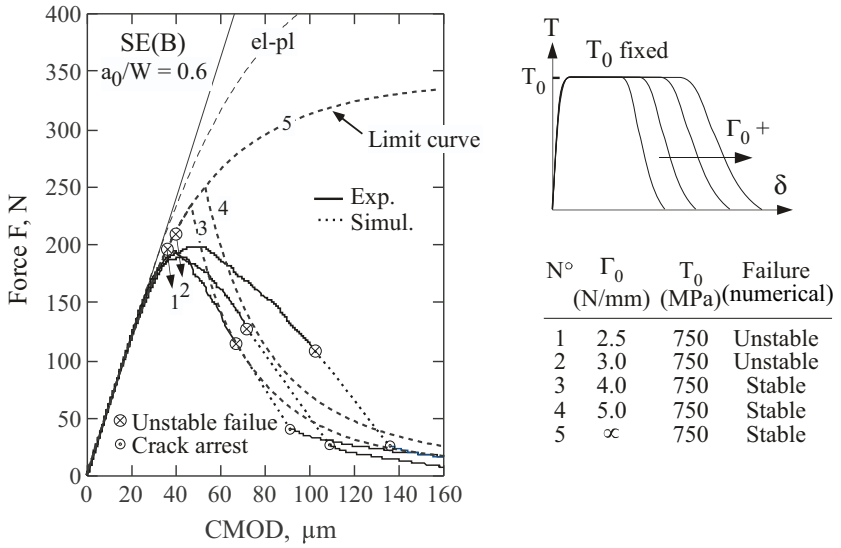

N°	Γ_0 (N/mm)	T_0 (MPa)	Failure (numerical)
1	2.5	750	Unstable
2	3.0	750	Unstable
3	4.0	750	Stable
4	5.0	750	Stable
5	$\propto$	750	Stable

Figure 5.6: Influence of Γ_0 on F-CMOD response of the γTAB alloy keeping T_0 fixed.

With the reduction of Γ_0 from 5 to 2.5 N/mm the maximum load reduces. For Γ_0 = 5 N/mm, the maximum load at the apex (about 250 N) overestimates the experimental maximum load (about 200 N) although the decreasing part matches quite well to the experimental counterpart. It seems that the curve with Γ_0 = 4 N/mm is somewhat better than Γ_0 = 5 N/mm when comparing with the maximum load and the softening part of the simulated F-CMOD curves. Therefore, Γ_0 = 4 N/mm can be taken as an appropriate average value for the cohesive energy, Γ_0, related to γTAB alloy.

5.3 Mesh dependency of the rectangular shape cohesive model

An appropriate FE mesh has to be generated in order to avoid the numerical problems during incremental nodal separation and strength reduction in the cohesive elements. In Chapter 4, some straightforward recommendations were given for the cohesive element size. The element length should not be much larger than $4\delta_0$. However, no stringent requirements can be provided.

Already seen from Fig. 5.3, the Tria-TSL provides stress-softening over a long range of elements, and the mesh size dose not influence the results considerably. The Rect-TSL follows a steep reduction of the strengths which is more sensitive to the change of traction and separation. This action may depend on the mesh size. As a general principle it has to be ensured that the numerical convergent problem due to instability of the system is free from mesh dependency. Therefore, following three kinds of meshes are examined:

1. Homogeneous fine mesh with 12 μm cohesive elements.
2. Heterogeneous mesh of medium (18 μm cohesive elements) and coarse (40 μm cohesive elements) sections.
3. Homogeneous coarse mesh with 40 μm cohesive elements.

For this investigation a Rect-TSL with $\delta_1 = 0.001\delta_0$, $\delta_2 = 0.70\delta_0$, T_0=750 MPa, and Γ_0=3.0 N/mm were chosen. The results are shown in Fig. 5.7(a-d). For the first case, the FE model with homogeneous fine mesh (12 μm element length) provides a continuous F-CMOD curve with a small load drop just after crack initiation. During damage process the incremental strength reduction for element nodal separation was mesh compatible such that the system equilibrium was maintained by the FE solver. For the second case, the crack propagated within the medium sized mesh but stopped at the transition from smaller to bigger elements. In a bigger element the nodal separation is larger, and the separation process requires a big strength reduction in the element. In such situation numerical solver problem arises. For the third case, the F-CMOD curve stopped at the onset of cohesive element separation. The continuous strength reduction requires appropriate incremental separation which was not achieved by the larger elements. The results show that the separation process is highly sensitive to the FE mesh. However, the stress development at the notch tip is not influenced by the mesh size, as shown in Fig. 5.7(b-d).

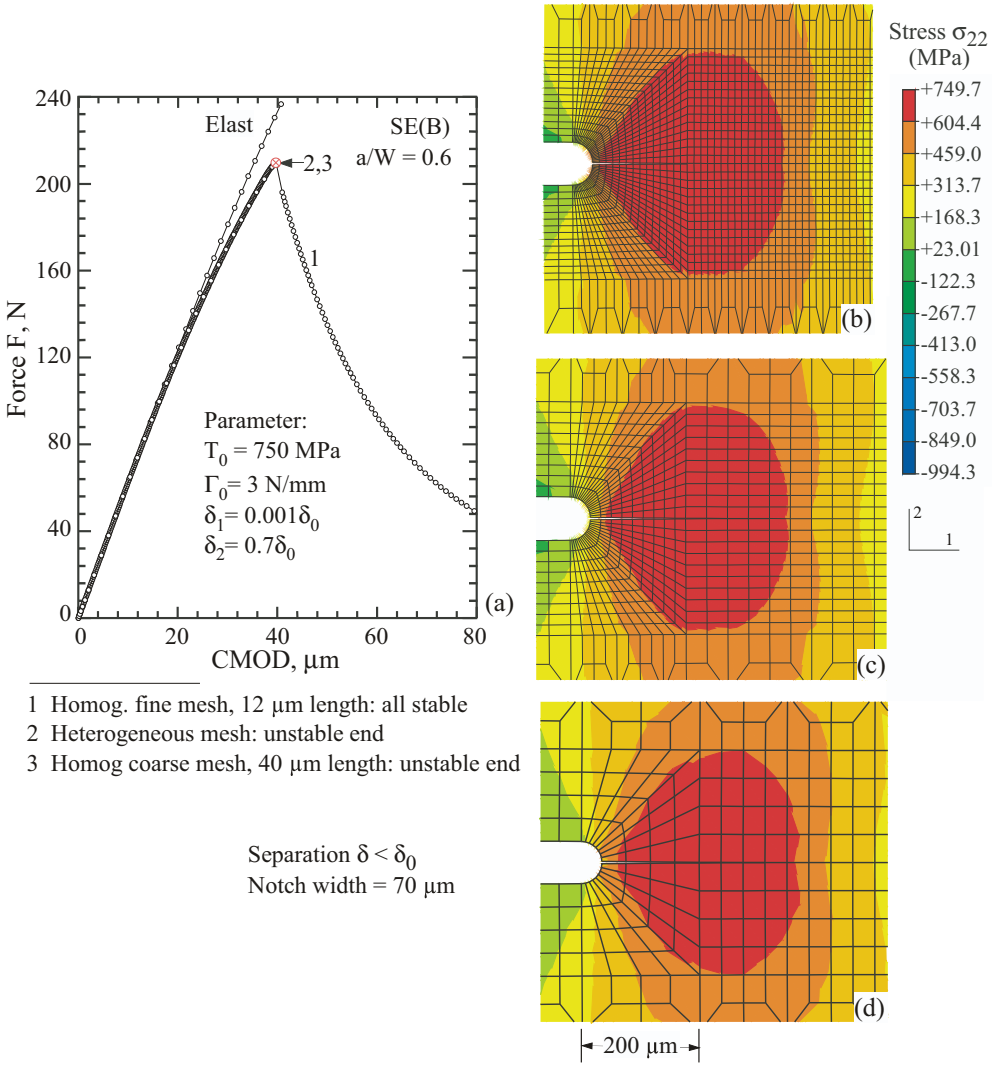

Figure 5.7: Mesh dependency of the Rect-TSL: (a) F-CMOD curves for different mesh densities, (b) homogeneous fine mesh, (c) heterogeneous mesh with the medium and coarse meshing, (d) coarse meshing

Chapter 6

Fracture simulation with a stochastic approach and its validation

In this chapter the modeling approach for simulating the quasi-brittle fracture of γTAB will be discussed. Also, the cohesive model incorporating stochastic parameters will be validated. In chapter 5 the material separation due to fracture was described on a predefined line in the 2D FE simulations of SE(B) specimens. Due to the absence of a 2D fracture plane the crack front can not be obtained here. As a result, the influences of the variable material properties on crack propagation can not be explained properly. Therefore, investigations are performed using 3D models. The numerical approach is discussed in three sections.

In section 6.1, a two-scale FE model is constructed to predict the polycrystal deformation behavior defined by a crystal plasticity based model. The local $\sigma-\epsilon$ curves of the polycrystal colonies are determined from the model.

In section 6.2, macro scale fracture behavior of the tensile bar is simulated with the proposed stochastic approach. Effects of the local $\sigma-\epsilon$ curves on the global response of a specimen as well as the contribution of the random cohesive parameters (T_0 and Γ_0) to the propagation of cracks are analyzed.

In section 6.3, variations of the cohesive parameters are implemented on a chevron notched bending specimen to simulate the experimental scatter and crack propagation that are observed in the F-v_{LL} curves. The principle aspects of the quasi-brittle fracture of lamellar γTiAl are discussed.

6.1 Micromechanical model of lamellar γTAB

6.1.1 Two-scale FE model of a lamellar polycrystal

In a two-scale model, the microstructural features of a polycrystal, such as the intermetallic phases, lamellae structure, random orientation of the lamellar colonies etc. are described at a local scale. In this local scale the micromechanisms of deformation are described by the continuum mechanics based constitutive equations. For any given overall strain, a localization rule determines the local scale solutions. Knowing the micromechanical stress state, the macroscopic stresses can be calculated using a homogenization rule.

The multiscale modeling approach correlates the micro-macro relationship using some localization and homogenization technique. Many multiscale modeling approaches can be found in the literature. In the present work the "FE^2 multiscale approach" [71] has been used. An FE^2 model was formulated in the previous work of multiscale modeling within the Collaborative Research SFB 371[1], entitled "Mechanics of Multiphase Materials". The model can be adopted for describing different length scale features of lamellar microstructures. The approach allows one to investigate the deformation behavior of randomly oriented colonies. The evaluation of the "FE^2 multiscale approach" for investigating the influences of colony orientations on the local and global deformation behavior covering the local stress-strain responses in a fully-lamellar polycrystal have not been accomplished so far.

In the lamellar microstructure of γTiAl alloy the lamellae phases (α_2, γ-matrix, γ-twin) are aligned parallel to each other. Between two α_2-phases many γ-phases can be situated (recall Fig 2.3 in Chapter 2). Such a lamellar microstructure was constructed setting many periodic unit cells (PUC) parallel to each other. Important microstructural features that influence the material properties, for example, presence of phases and their orientations in a lamellar microstructure, were described in representative volume elements (RVE). The RVE represents the minimum material volume of a microstructure. To describe a (α_2+γ)TiAl lamellar microstsructure, RVEs were defined for three lamellar phases, α_2, γ-matrix and γ-twin respectively. The RVEs were embedded into the PUCs to generate the lamellar microstructure. Volume contents of these phases (α_2 about 5%, $\gamma_m = \gamma_t = 47.5\%$) were maintained in the PUCs. For a prescribed lamellae orientation, this PUCs were arbitrarily rotated in 3D space.

A PUC model of lamellar microstructure consisting of different phases is shown in Fig. 6.1(a). In Fig. 6.1(b) a simple PUC is constructed with one set of α_2, γ-matrix, and γ-twin phases.

The PUC model was used to generate a polysynthetically twinned (PST) single crystal with a specific lamellae orientation. The PST crystal is a single grain with lamellar structure. The lamellar microstructure including lamellae phases, lamellae thickness and orientation can be controlled during PST crystal generation. A single PST crystal is equivalent to a single lamellar colony. Therefore, a fully lamellar polycrystal with randomly oriented colonies can be modeled by combining many

[1]Collaborative Research "SFB 371" conducted at the Technical Universtiy Hamburg-Harburg together with GKSS Research Centre Geesthacht, 1993 – 2003, financed by Deutsche Forschungsgemeinschaft.

PST single crystals with random lamellar orientation. In Fig. 6.2(a,b) such a cubic polycrystal model is constructed with 64 PST crystals. The orientations of the lamellar colonies were defined by the respective orientation directions of the PUCs.

At a meso scale a single colony was discritized with 8 FE elements (Fig. 6.2(b)). Each element was then linked with periodically arranged 8 PUCs at a micro scale (Fig. 6.2(c)). As a result, a single lamellar colony consists of 64 PUCs. The micro level PUCs and the meso level colonies are linked by the FE^2 principle as described in [46, 72].

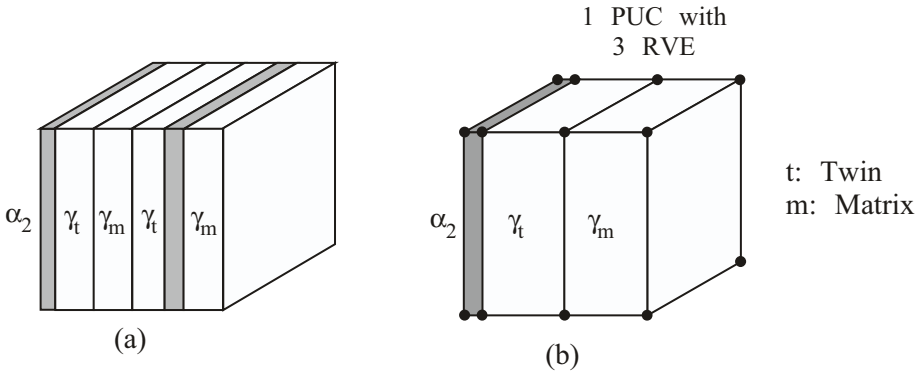

Figure 6.1: Lamellar microstructure: (a) PUC with lamellae phases as seen in the microstructure, (b) simplified PUC with single lamellae phases as used in the two-scale FE model.

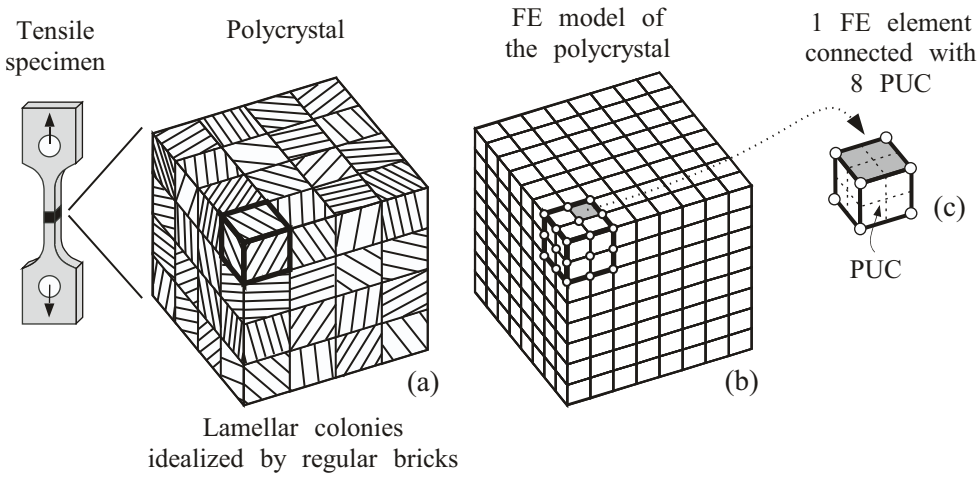

Figure 6.2: Modeling of lamellar γTAB polycrystal with the FE^2 approach: (a) regular cube consisting of 64 PST crystals, (b) FE elements (mesh) consisting of the regular PST crystals, (c) one FE element described by 8 PUC.

The polycrystalline cube has an edge length of 400 μm and an average colony size of 100 μm (size of the PST crystal). The orientations of lamellae colonies are analogous to the observed orientation from the cross-section of the extruded bar, i.e., about ± 20° against the extrusion direction, but are randomly rotated across the radial direction.

6.1.2 Crystal plasticity

Deformation behavior of the α_2 and the γ-phases are described in an ABAQUS user defined material subroutine (UMAT) for crystal plasticity. The UMAT was originally developed by Huang [73] and modified by Lin et al. [74]. The constitutive law used in the UMAT is based on a rate-dependent visco-plastic formulation:

$$\frac{\dot{\gamma}^{(\eta)}}{\dot{\gamma}_0} = \left|\frac{\tau^{(\eta)}}{g^{(\eta)}}\right|^{m-1}\left(\frac{\tau^{(\eta)}}{g^{(\eta)}}\right), \tag{6.1}$$

where, $\dot{\gamma}^{(\eta)}$ is the shear rate of the slip system η, $\dot{\gamma}_0$ is a reference shear rate, $\tau^{(\eta)}$ is the Schmidt-stress in η, $g^{(\eta)}$ is the current yield stress of η, and m is the strain rate exponent. The initial yield stress, $g^{(\eta)}$, is identical to the critical resolved shear stress (CRSS), which is the required minimum stress to initiate slip on a given slip plane and in a given direction.

The evolution of $g^{(\eta)}$ is described by a linear hardening law:

$$\dot{g}^{(\eta)} = h_0^{(\eta)} \sum_{\beta} q_{\eta\beta}\dot{\gamma}^{(\beta)}, \tag{6.2}$$

where $h_0^{(\eta)}$ is the hardening modulus, and $q_{\eta\beta}$ is the hardening matrix. The values of $q_{\eta\beta}$ are generally found to be in the range of 1.0 to 1.4, however, for the particular case of α_2 and γ, information about the appropriate values are not found anywhere in the literature. Therefore, $q_{\eta\beta}$ is assumed to be 1.0 for all slip systems of η and β.

6.1.3 Simulation of local stress-strain behavior of the polycrystal colonies

Identification of crystallographic parameters for γTAB

As the lamellar colonies in the polycrystal were analogous to the lamellar PST crystals of same crystallographic slip systems, the parameter set for the fully lamellar γTAB polycrystal can be determined from the parameter set of the PST crystal. In literature the crystallographic parameters, such as strength of the slip systems, g_0, and hardening parameters, h_0, of a lamellar PST crystal for the binary composition of Ti-49.3Al were determined using the two-scale FE model in conjunction with the experiments [23, 46]. The parameters are the following:

$$g_0^{\text{long}} = 55\text{MPa}, \qquad h_0^{\text{long}} = 400\text{MPa} \tag{6.3}$$

$$g_0^{\text{mix}} = 150\text{MPa}, \qquad h_0^{\text{mix}} = 320\text{MPa} \tag{6.4}$$

$$g_0^{\text{trans}} = 185\text{MPa}, \qquad h_0^{\text{trans}} = 135\text{MPa} \tag{6.5}$$

The superscripts long, mix, and trans stand for longitudinal, mixed, and transverse slips respectively. The flow curves for 0°, 45° and 90° orientations were quantitatively satisfied by the parameters.

To determine the parameters for the lamellar polycrystal with randomly oriented colonies, tensile simulations were performed using the FE^2 model. The global stress-strain curves were calculated

from the reaction force as a response of imposed longitudinal deformation. Taking the PST crystal parameters (Eq. 6.3, 6.4, 6.5) as a basis, different parameters were studied and the simulated $\sigma-\epsilon$ curves were adjusted with the tensile test records. The best fitted curve is shown in Fig. 6.3.

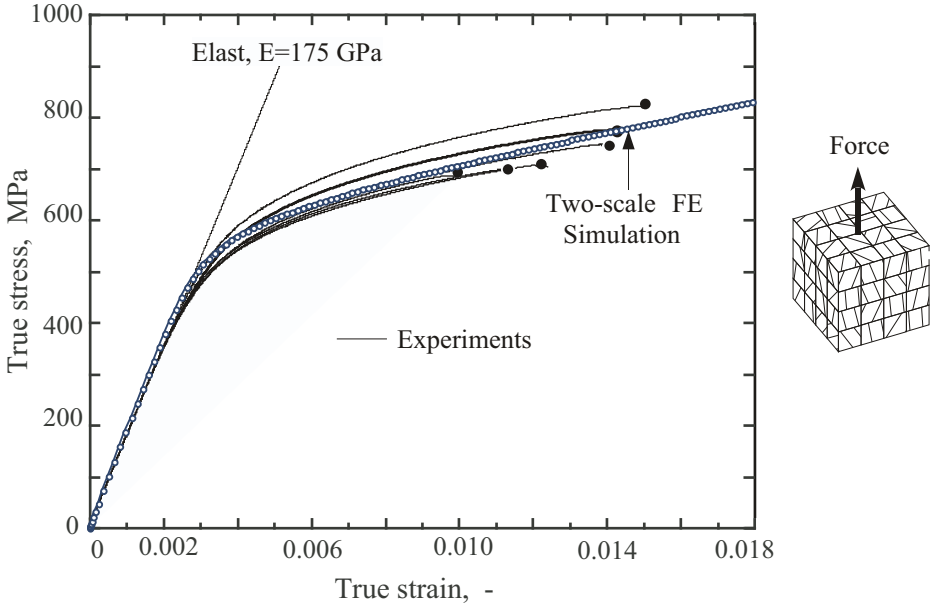

Figure 6.3: Stress-strain curve from the multiscale simulation of tensile test, used for crystallographic parameter identification.

The fitted $\sigma-\epsilon$ curve from the polycrystal simulation matched the overall behavior of the experimental $\sigma-\epsilon$ curves quite well. The crystallographic parameters of the γTAB polycrystal are taken from this fitted curve. The obtained parameters are:

$$g_0^{\text{long}} = 82.5\text{MPa} \qquad h_0^{\text{long}} = 2400\text{MPa} \tag{6.6}$$

$$g_0^{\text{mix}} = 175\text{MPa} \qquad h_0^{\text{mix}} = 2400\text{MPa} \tag{6.7}$$

$$g_0^{\text{trans}} = 277.5\text{MPa} \qquad h_0^{\text{trans}} = 2400\text{MPa} \tag{6.8}$$

The above values are higher than the PST crystal parameters. As explained in [46] these higher values are due to the inhomogeneous lamellar microstructure in the polycrystal and the deformation constraints from the neighboring colonies.

Strain profile

In Fig. 6.4 the strain profile at the outer surfaces of the polycrystal cube at a global strain, $\epsilon_{22} = 2.5\%$ is shown. The strain component, ϵ_{22}, is plotted in a scale of 1.665-3.682% for clarity. The figure shows red areas with higher strains and blue areas with lower strains. Due to oriented colonies the hard and easy mode of deformation are active in a polycrystal. Each embedded colony experiences deformation constraints, consequently, inhomogeneous stress and strain fields are generated in the polycrystal.

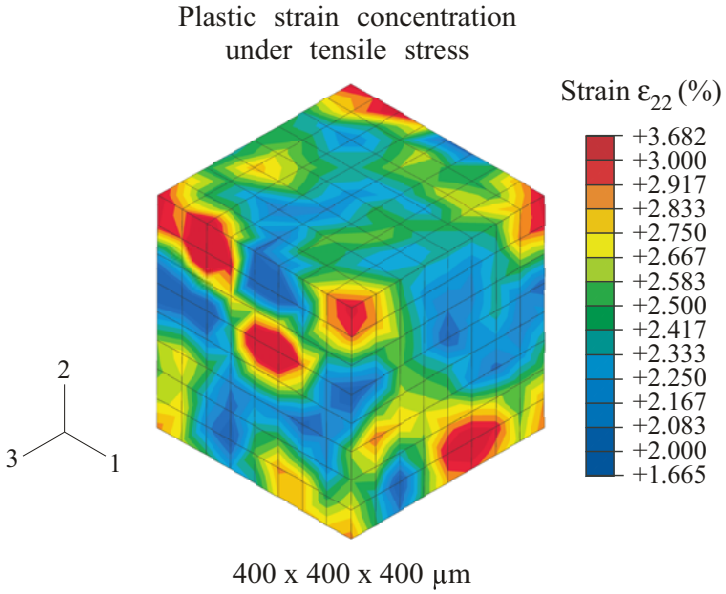

Figure 6.4: Plastic strain concentrations across the regular cube with 64 colonies specified for γTAB.

Local variation of stress-strain

The colony stress and strain are obtained by homogenizing the stresses and strains over the 64 PUCs. Following relationships are used:

$$\sigma_{colony} = \sum_{i}^{64} \sigma_{puc}, \tag{6.9}$$

$$\epsilon_{colony} = \sum_{i}^{64} \epsilon_{puc}, \tag{6.10}$$

Using the above relationships the component stress in loading direction (σ_{22}) as well as the von Mises effective stress (σ_e) for each colony is calculated. In Fig. 6.5 the simulated component stress-strain curves (σ_{22}-ϵ_{22} curves) as well as the von Mises equivalent stress-strain curves (σ_e-ϵ_e curves) for all the 64 colonies are plotted. The figures show large variations for both the σ_{22}-ϵ_{22} and σ_e-ϵ_e curves. The variation band of σ_{22}-ϵ_{22} curves is slightly larger than the variation band of σ_e-ϵ_e curves. As the component stresses are highly influenced by the deformation constraint from the neighborhood, this differences in the variation band is expected.

The true $\sigma-\epsilon$ curve from the global response of the polycrystal cube is also included in Fig. 6.5a. The global stress-strain curve lies almost in the middle of the variation band. This means that globally the polycrystal has produced an averaged response despite large σ_{22}-ϵ_{22} variations across the colonies.

The elastic slopes also vary for all the colonies. This variation obviously comes from the orthotropic elastic properties of the α_2 and γ-phases. Due to random orientation of the colonies, the deformation behavior of the phases is dominated by certain elastic component, which changes the average elastic behavior of the colonies.

Frequency distributions of the σ_{22}-ϵ_{22} curves are determined at two distinct global strains, ϵ_{22} = 1.5% and 2%, and are shown in Fig. 6.6. From the bar diagram a Gauss or a Weibull distribution function can be derived. No experimental validation has been performed for the variation band.

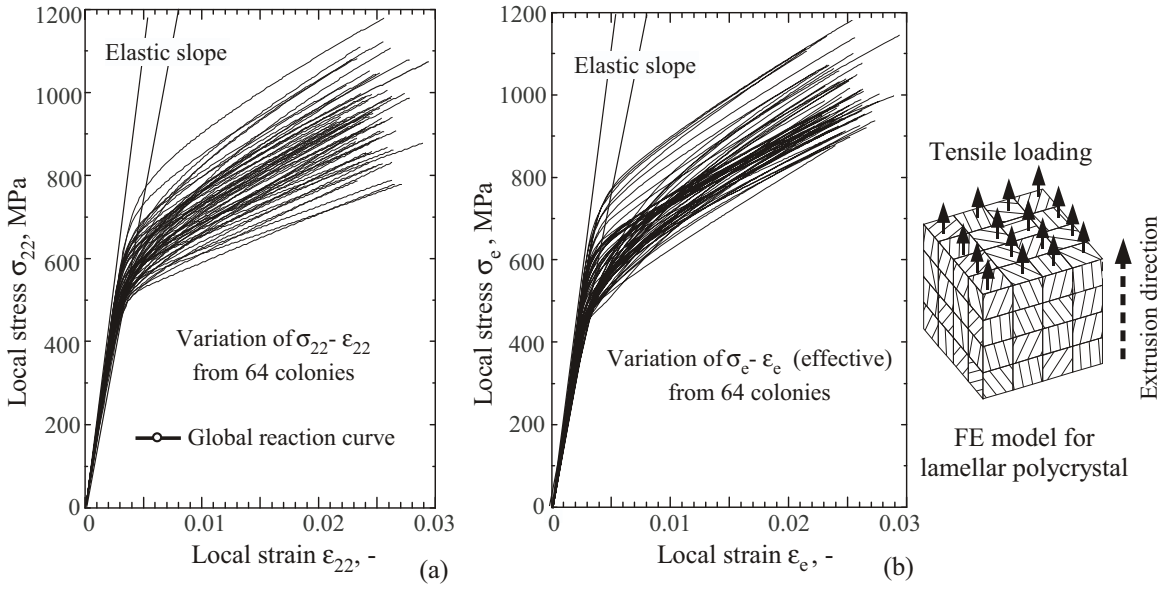

Figure 6.5: Local stress-strain curves of 64 lamellar colonies simulated with the two-scale FE model, (a) variation in σ_{22}-ϵ_{22} curves, (b) variation in σ_e-ϵ_e curves.

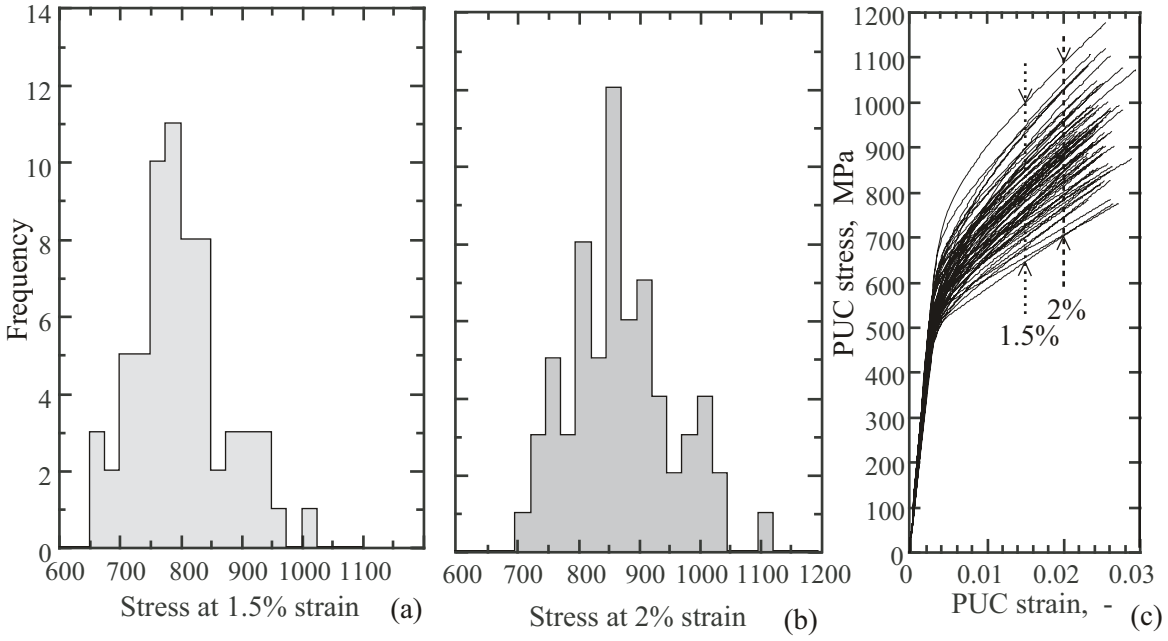

Figure 6.6: Variations of the stress-strain curves from the multiscale simulation for the polycrystal γTAB at 1.5% and 2% global strains.

Influence of deformation constraints of the colonies

The local deformation constraints due to neighboring colonies are simulated. The transverse deformation constraints in the polycrystal that result from the neighboring colonies of different orientations will be denoted as "constraint effect". To analyze the constraint effects, a centered PST crystal in the polycrystalline cube (colony number 26) has been chosen. The same colony was modeled as a single PST crystal (no neighboring colonies are present) with the same material and orientation definitions.

The two cases are shown in Fig. 6.7(a,b) and the simulated stress-strain data are plotted in Fig. 6.7(c). It can be seen that the embedded colony underlies higher constraints, which increase the stresses during imposed deformation. On the other hand, the constraint free colony (PST crystal) exhibits much lower stresses under increasing strains.

The increment of longitudinal stresses, σ_{22}, in the embedded colony depends on the surrounding anisotropic PST crystals, which causes a significant variation of local σ_{22}-ϵ_{22} curves in the polycrsytal.

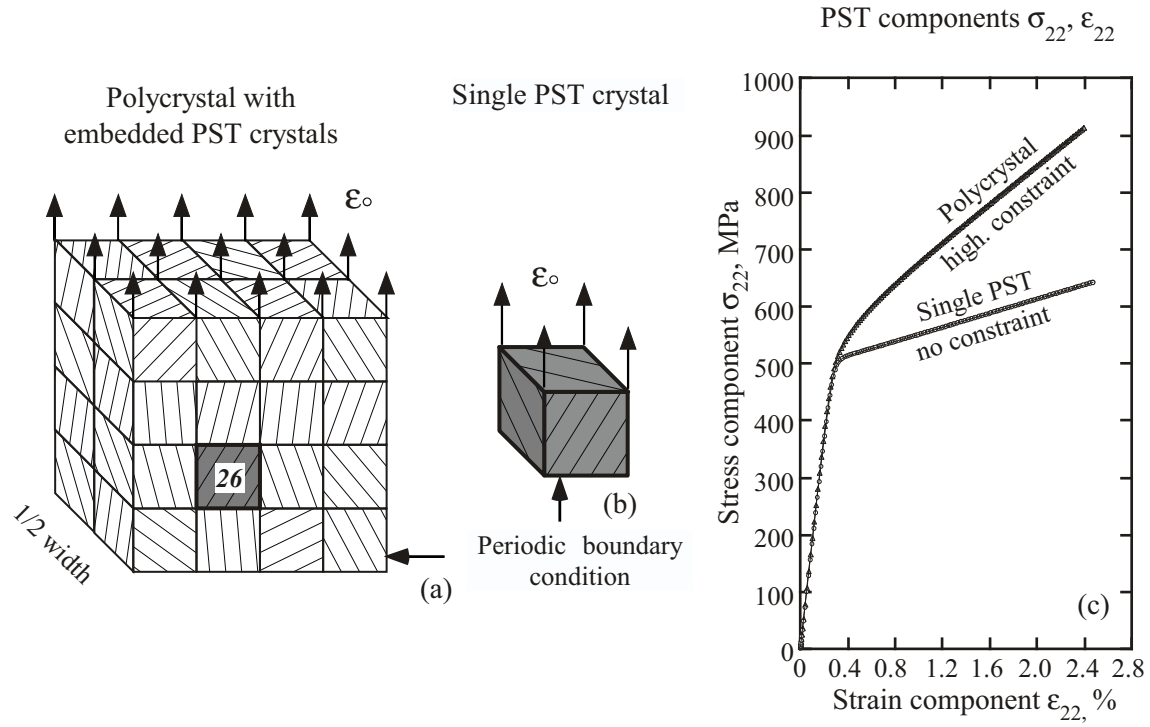

Figure 6.7: Constraint effect in a lamellar polycrystal: (a) constrained PST crystal (number 26) embedded in the regular cube, (b) constraint free PST crystal, (c) stress-strain curves showing the constraint effect.

6.1.4 Anisotropic effects of lamellae orientations in the polycrystal

Previously in chapter 3, Fig. 3.3, a scatter band was shown for the experimental $\sigma-\epsilon$ curves. For the lamellar TiAl alloys two possible explanations for this scatter may be given:

1. In TiAl alloy the lamellae orientations against the loading axis yield anisotropy in flow stresses and plastic strains, as was reported in [16]. The rotations of the colonies about the loading axis (perpendicular to the cross-section of the extruded bar) do not have much influences on the stress-strain behavior [75].

   For the polycrystal, this anisotropic effect may contribute to a stronger or a weaker global response. As the colonies of the extruded rod are oriented in the range of $\pm\ 20^0$ with respect to the load axis, only a minor influence on the resulting $\sigma-\epsilon$ curves is expected.

2. Presence of unexpected grain structures (like duplex grains situated among the fully lamellar microstructure) or the clusterization of the colonies within the microstructure can not be avoided during processing.

The first explanation for the anisotropic effect is verified using two-scale FE^2 simulations. Single and polycrystal models with randomly oriented colonies are generated from which the effects of colony orientations on the global deformation behavior of the γTAB alloy are studied. The following cases are examined:

1. Single crystal behavior expressed for the three distinct lamellae orientations, $\varphi = 0°$, $45°$ and $90°$. φ is the orientation angle of the lamella plane with respect to the loading axis. $\varphi = 45°$ is the soft mode of lamellae orientation, $\varphi = 0°$ is the intermediate mode, and $\varphi = 90°$ is the hard mode.

2. Polycrystal behavior expressed for the following three cases. ξ is the rotation angle of the lamellar colonies about the loading axis.

Case	Rotation angle ξ of the lamellar colonies about the loading axis	Inclination (orientation) angle φ of the lamellar colonies against the loading axis
A	Randomly aligned (isotropic) $0° \leqslant \xi \leqslant 360°$	Randomly aligned within $-20° \leqslant \varphi \leqslant +20°$
B	Random (isotropic) $0° \leqslant \xi \leqslant 360°$	Uniformly aligned $\varphi = 0$
C	Random (isotropic) $0° \leqslant \xi \leqslant 360°$	Uniformly aligned $\varphi = 45$

Table 6.1: Case of study for γ-TAB with single and polycolony

The lamellae orientation of $\varphi = 90°$ has been excluded from the analysis since this kind of lamellae arrangement could not be found in the γTAB alloy.

The polycrystalline cube in Case A has the same orientation definition as the investigated γTAB material. Transverse to the extrusion direction (which here is also the loading direction) the colonies

are aligned in a quasi-isotropic manner without textured preferences ($0° \leqslant \xi \leqslant 360°$). Along the extrusion direction the colony alignment is confined in a narrow band, i.e., $-20° \leqslant \varphi \leqslant +20°$.

For Case B, an idealization has been introduced, i.e., all colonies in extrusion direction have the same parallel alignment, $\varphi = 0°$, while keeping the ξ rotation the same as in Case A.

In Case C, all colony planes are inclined ($\varphi = 45°$) against the loading axis. Transverse to the loading axis the quasi-isotropic random rotation of the lamellar colonies ($0° \leqslant \xi \leqslant 360°$) is maintained, like in Case A.

In Fig. 6.8(a), the $\sigma-\epsilon$ curves for a single PST crystal for three lamellae orientations under tensile loading are shown. Differently oriented lamellae activate different kinds of twinning and slip systems [16], which result in highly anisotropic deformation.

Fig. 6.8(b) shows the deformation behavior (expressed by $\sigma-\epsilon$ curves) of the lamellar polycrystal. Compared to the results of the single PST crystal, hardly any φ-orientation effects are seen. For $\varphi = 0°$ (Case B) and $\varphi = \pm 20°$ (Case A), a minor difference in the $\sigma-\epsilon$ curves is found. For the soft lamellae orientation, $\varphi = 45°$, this $\sigma-\epsilon$ curve deviates early from the elastic curve, however, this curve lies significantly above the $\sigma-\epsilon$ curve obtained from the single PST crystal for the same orientation.

For the polycrstal, the three curves lie in a narrow band. The models in these three cases (Case A, B and C) have analogous random orientations (transverse to the loading axis, i.e., $0° \leqslant \xi \leqslant 360°$) and all of them are subjected to almost the same degree of constraint effects.

With the presence of a few soft colonies, the global $\sigma-\epsilon$ curves of the polycrystal will remain close to the results observed for cases A or B. The results indicate that the global variation of $\sigma-\epsilon$ curves observed in the tensile tests may come from the supplementary influences of the microstructural variations and not only due to the random orientation of the colonies.

A significant variation in the $\sigma-\epsilon$ curves can be obtained due to pronounced occurrences of soft mode ($\varphi = 45°$) or hard mode ($\varphi = 90°$) orientations, however, such arrangements can not be found in the extruded γTAB alloy.

6.1.5 Local variation of stress-strain curves for the stochastic approach

The local variation of stress-strain curves are incorporated in a continuum based macro model, by which the deformation behavior of the colonies is captured. The variation of equivalent stress-strains of the colonies, as shown in Fig. 6.5b, is considered for this macro scale modeling. These σ-ϵ curves describe the von Mises type plasticity for the colonies.

For modeling simplicity, only the upper limit and the lower limit of the curves are taken as the variation band. This band is equally divided into five $\sigma-\epsilon$ curves, i.e., $\sigma-\epsilon.1$ to $\sigma-\epsilon.5$ as depicted in Fig. 6.9. The $\sigma-\epsilon.3$ curve is the arithmetic mean of the five $\sigma-\epsilon$ curves. The polycrystal average behavior is described by this curve. This curve will also be denoted as σ-ϵ.Mid.

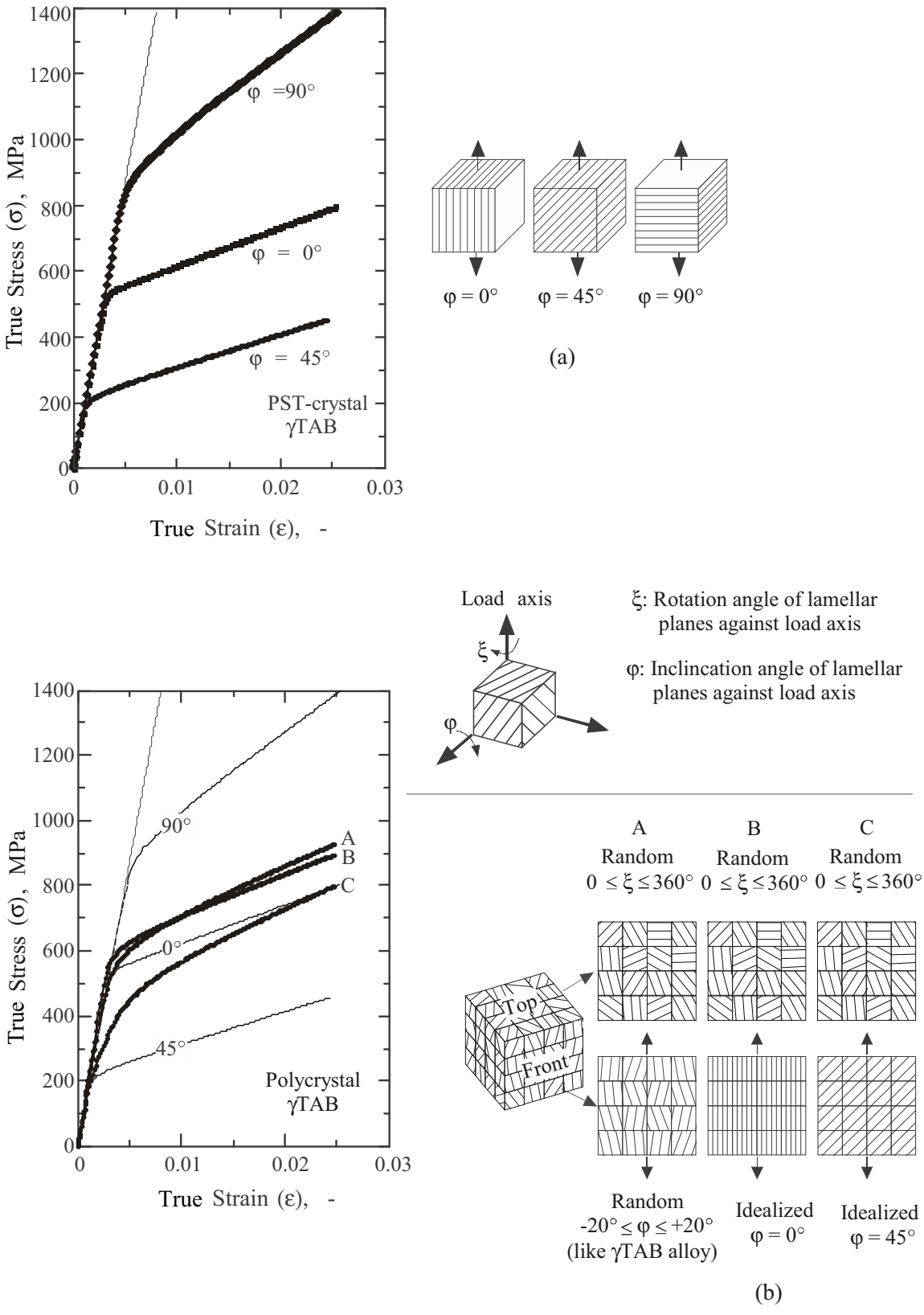

Figure 6.8: Effects of lamellae orientation along the load-axis: (a) for a single PST crystal, (b) for a polycrystal consisting of 64 colonies

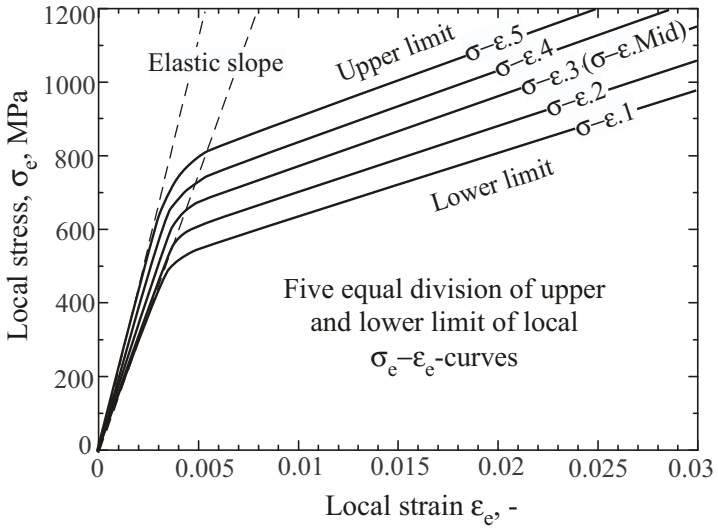

Figure 6.9: Five σ_e-ϵ_e curves for the stochastic simulation.

6.2 Fracture simulation of tensile bar at a macro scale

In the present section the influence of material properties on the scatter of experimental stress-strain curves will be investigated. For this analysis fracture simulations are performed on the tensile specimens using a stochastic approach of the cohesive model. The deformation behavior of the tensile model is described by local stress-strain curves of the polycrystal colonies, while the fracture is described by cohesive strength and cohesive energy. The parameters are considered to be stochastic in nature and have a certain variation band. The variation bands in the present case are taken from experimental results and numerical simulations. For example, the variation band of the local stress-strain curves (σ_e-ϵ_e curves) of the polycrystal are obtained from the two-scale simulation. For cohesive strength, T_0, exact values can not be obtained by straightforward means. However, for brittle or quasi-brittle material like γTAB, reasonable approximations of the T_0 are the experimentally determined global maximum stresses from the true stress-strain curves, which are very close to the physical fracture strengths. With this assumption the variation band for T_0 is approximated and taken between 680 and 820 MPa. The variation band of the cohesive energy, Γ_0 is determined from the fracture tests of the bend specimen. The band lies between 3 to 5 N/mm.

6.2.1 FE modeling

Due to three fold symmetry one-eighth of the flat tensile bar was modeled. The experimental tensile bar and the meshed FE model are shown in Fig. 6.10(a,b). The fracture plane was constructed at the symmetry plane using a layer of 3D cohesive elements (see Fig. 6.10(c), number 3). The 3D cohesive elements are the zero thickness interface elements, which respond according to the "cohesive law of separation" to simulate crack propagation along the fracture plane.

The fracture plane was divided into 100 x 100 μm^2 quadratic areas which are denoted as "cohesive blocks". Each cohesive block was subdivided into fine meshes with a 20 x 20 μm^2 size. Therefore, each cohesive block contains 25 FE elements. Above the fracture plane two regions were chosen, the moderate mesh (marked with "2") and the coarse mesh (marked with "1") in Fig. 6.10(c). Three types of models were developed for this investigation.

Model A: Global fracture of a tensile bar influenced by the stochastic nature of fracture parameters.

For this investigation, the fracture parameters of the cohesive model (T_0 and Γ_0) were randomly assigned throughout the cohesive blocks in region 3, see Fig. 6.10(c). The rest of the model was considered as a homogeneous polycrystal which follows an average von-Mises type elastic-plastic constitutive behavior described by $\sigma-\epsilon.3$. The curve σ-$\epsilon.3$ will also be denoted as σ-ϵ.Mid

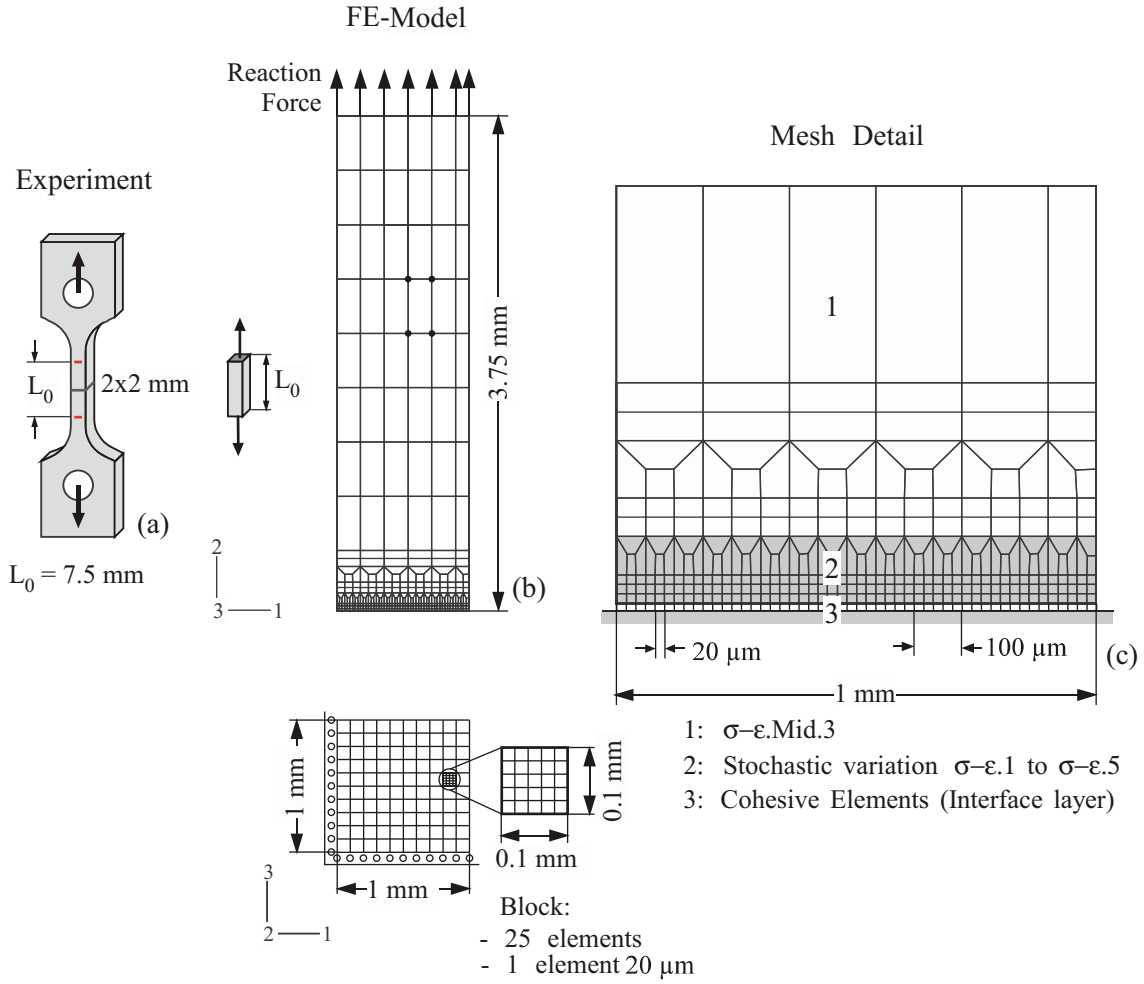

Figure 6.10: FE model of the flat bar tensile specimen: (a) Tensile specimen, (b) FE model of the tensile bar, (c) Mesh detail. The stress-strain curves are defined in section 6.1.

Model B: Global fracture of a tensile bar influenced by the stochastic nature of fracture parameters coupled with the evolution of local inhomogeneous stress-strain developments in the vicinity of the fracture process zone.

For this investigation, the fracture parameters, T_0 and Γ_0, were distributed in the same way as Model A. Additionally the σ-ϵ.1 to σ-ϵ.5 curves were randomly distributed in region 2. With this arrangement, the inhomogeneous deformation (described by the five individual von-Mises type elastic-plastic constitutive behaviors) in the vicinity of the fracture process zone was phenomenologically described.

The bottom faces in region 2 were compatibly attached to the cohesive blocks in region 3. For this reason, region 2 was divided into 3D blocks of 100 x 100 μm^2 faces and denoted as continuum blocks. Thus, the global response of the model incorporated the influence of both elastic-plastic behavior of the colonies and their fracture properties.

The rest of the model (region 1) was considered as a homogeneous polycrystal which follows an average von-Mises type elastic-plastic constitutive behavior described by the $\sigma-\epsilon$.Mid.

Model C: Global deformation and fracture of a tensile bar influenced by the stochastic nature of fracture parameters and local inhomogeneity of stress-strain fields throughout the model.

For this investigation the fracture parameters, T_0 and Γ_0, and the σ-ϵ.1 to σ-ϵ.5 curves were randomly distributed like Model B. Moreover, in region 1, contrary to Model B, the σ-ϵ.1 to σ-ϵ.5 curves were stochastically distributed. By doing this, the local polycrystal deformation was phenomenologically described in the whole tensile model.

6.2.2 Distribution of stochastic parameters

For cohesive strength, T_0 and cohesive energy, Γ_0:

Discrete values of T_0 and Γ_0 within the variation band were generated using a random generator. For Models A and B these values were randomly distributed under a constant frequency distribution, defined by a rectangular distribution function (see Fig. 4.4), along the 100 cohesive blocks. This kind of distribution represents a constant probability density with equal probability of failure for each block.

For Model C, the frequency distribution functions shown in Fig. 4.6 were used to define the variation of cohesive parameters, T_0 and Γ_0. By implementing such distribution functions one can set priorities to the occurrence of certain fracture properties.

For $\sigma-\epsilon$ curves:

For Model B, the five σ-ϵ curves were randomly distributed like T_0 and Γ_0 using the rectangular distribution function (as shown in Fig. 4.4) along the 100 continuum blocks.

For Model C, the five σ-ϵ curves were also distributed according to the frequency distribution function shown in Fig. 4.6. The whole tensile model was divided into small volumes, where the random parameters were applied. With these distribution functions, priorities are given to certain σ-ϵ curves to control the influence of global elastic-plastic behavior.

A summary of the property distribution and the models is shown in Fig. 6.11.

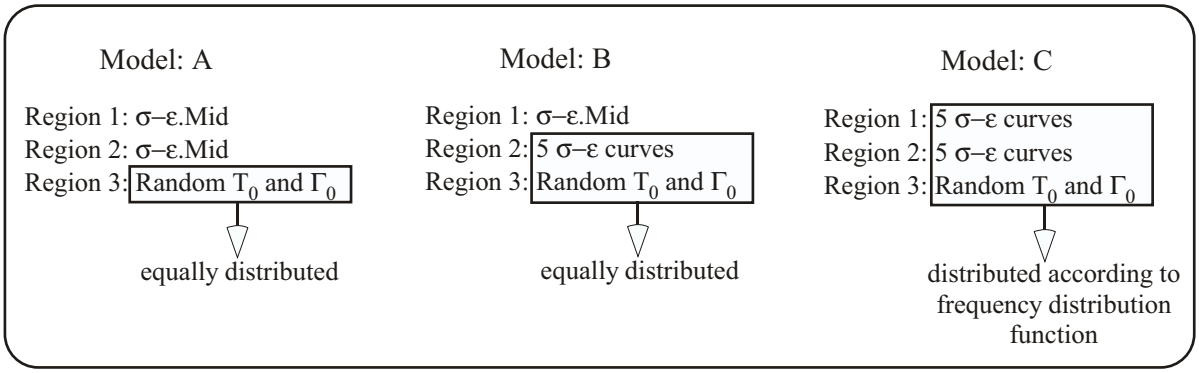

Figure 6.11: Summary of the model analysis.

6.2.3 Tensile test simulation using stochastic approach

Model A and Model B:

The stochastic parameters for model A and B are summarized in Table 6.2. For Model A only one simulation was performed denoted as RD.Mid, while for Model B three cases were simulated with three different distributions, denoted as RD.01, RD.02, and RD.03. Additionally, the variation of cohesive parameters for RD.03 were assigned to be the same as RD.Mid in order to compare the effect of local inhomogeneous stresses and strains in the vicinity of the fracture zone. By comparing the RD.03 and RD.Mid the effects of the global fracture, crack initiation, and crack evolution on the $\sigma-\epsilon$ curves can be identified.

Model-Case	σ-ϵ curve	T_0, MPa	Γ_0, N/mm	Random generation
Model A-RD.Mid	Only σ-ϵ.Mid	680-820	3 - 5	T_0 and Γ_0 variations are identical to RD.01
Model B-RD.01	σ-ϵ.1 - σ-ϵ.5	680 - 820	3 - 5	Distribution type 01
Model B-RD.02	σ-ϵ.1 - σ-ϵ.5	680 - 820	3 - 5	Distribution type 02
Model B-RD.03	σ-ϵ.1 - σ-ϵ.5	680 - 820	3 - 5	Distribution type 03

Table 6.2: Case of study for different random distributions

The simulation results for the four models are shown in Fig. 6.12. Due to the same elastic-plastic constitutive behavior (described by σ-ϵ.Mid) all the curves lie on the average $\sigma-\epsilon$ curve ($\sigma-\epsilon$.Mid). However, minor variations in the fracture points were obtained, which were caused by the variation of T_0 (820-680 MPa) and Γ_0 (5-3 N/mm).

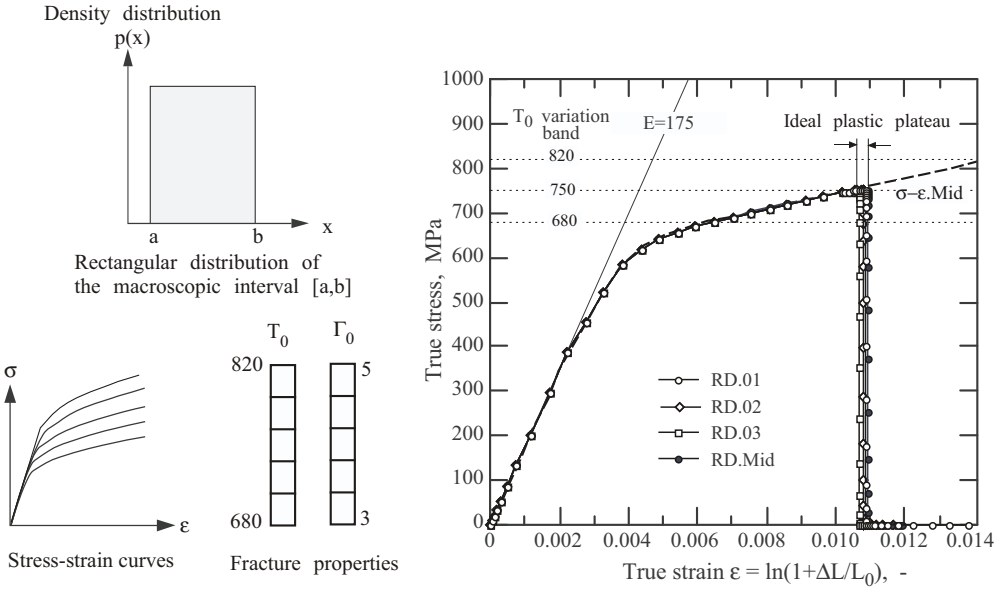

Figure 6.12: Global response of several stochastic simulations of the tensile bar: RD.01, RD.02, RD.03, and RD.Mid

In Fig. 6.13 a magnified view of the maximum stress level is shown. For RD.01 RD.02 and RD.03 minor differences near the maximum can be observed. These differences came from the locally developed inhomogeneous stress due to the variable σ-ϵ-curves near the fracture surface. At the maximum stress a small plateau can be seen. This occurred due to the constant traction part of the Rect-TSL. On this maximum stress plateau, locally no fracture takes place i.e., no crack initiation occurs. The data attained from the FE calculations showed that local crack initiations had occurred at a lower T_0, however, due to the local deformation constraint all specimen failed around the average cohesive strength, $T_{0,mean}$ = 750 MPa.

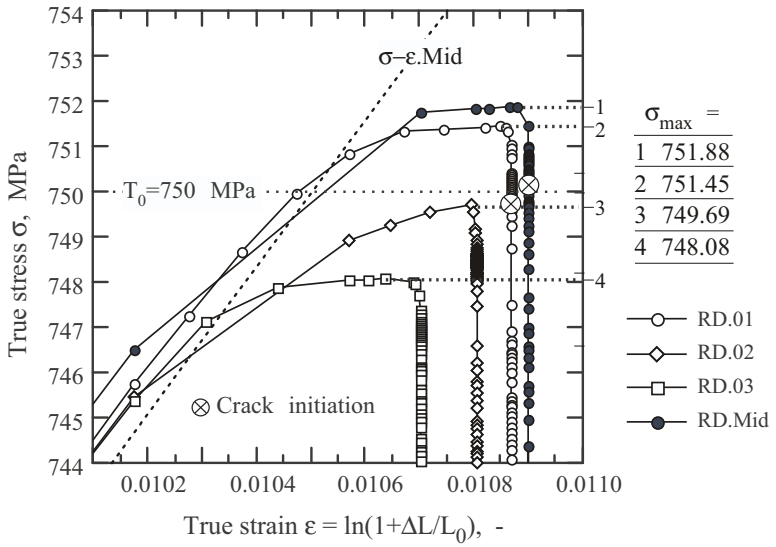

Figure 6.13: High resolution of the maximum region of the stochastic simulations.

For model A and B the bulk material was described by the σ-ϵ.3-curve. This assumption implies that the specimens have an identical microstructure. As the miniature specimens were taken from different positions of the parent material, slight changes in the microstructure for all the specimens are expected. This microstructural change results in a variation in the experimental σ-ϵ curves. To capture this variation a change in the material properties (or a shift in the properties) in each tensile model needs to be considered. Information about this property changing can only be obtained if the frequency distribution of the material properties are known. Only six experiments, as has been done for the present case, are not sufficient to quantify these distributions. Therefore, Model C is generated with some assumed frequency distributions. The modeling assumptions and the results are discussed below.

Model C:

To take into account the possible material property variations (i.e., shift in the material properties from specimen to specimen) four distribution functions, FD.A, FD.B, FD.C and FD.D, were assumed. The parameters and the assumed histogram of the distributions are shown in a schematic drawing in Fig. 6.14. Here, the variation bands of the local σ-ϵ-curves, T_0 and Γ_0 were divided into five groups X1, X2, X3, X4, X5 (shown previously in Fig. 4.6a), which are placed along the horizontal axis of

Fig. 6.14. The frequency of occurrences of these values are plotted along the vertical axis. Frequency of occurrence in this case means how much volume percent of the material in a specimen is occupied by a certain parameter-value. For example, higher occurrence of X1 means that the X1 value appears more frequently than the other parameters, and that this value occupies a larger material volume.

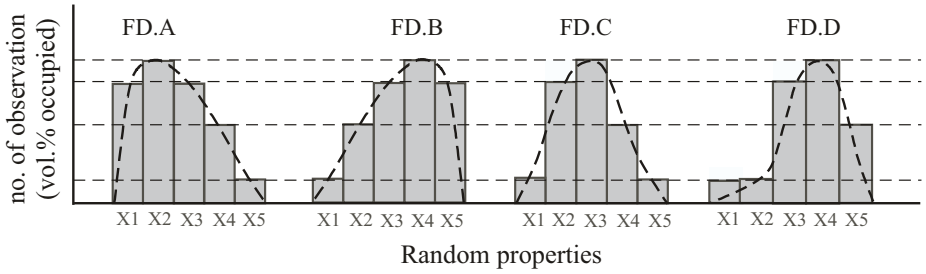

Figure 6.14: Four assumed frequency distributions.

The material parameters, which follow any of the above distribution functions, are assigned randomly in the tensile model. In Fig. 6.15 parameter distributions for the calculation set A are shown. Here, the σ-ϵ-curves are distributed under FD.A and the cohesive parameters are distributed under FD.A, FD.B. FD.C and FD.D. Therefore, four models are obtained. The global stress-strain responses of the models are SR.A1, SR.A2, SR.A3, and SR.A4.

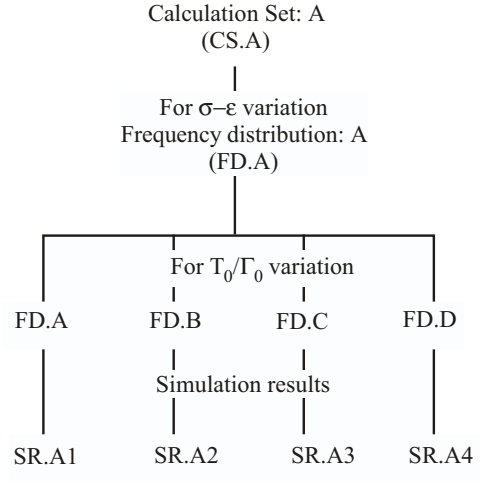

Figure 6.15: Arrangements of the parameters for simulation, calculation set A is shown.

Similar to FD.A, the σ-ϵ-curves are distributed under FD.B, FD.C and FD.D and the the cohesive parameters are distributed under FD.A, FD.B. FD.C and FD.D. For each set of σ-ϵ distribution, four simulated results are obtained. The parameter arrangements that are used in this investigation are shown in Table 6.3.

The three parameters, σ-ϵ, T_0, and Γ_0 can be arranged in many different ways by combining similar or different frequency distributions. Each arrangement results in a particular parameter distribution related to a particular specimen that is taken from a random position of the extruded rod.

Variation of σ-ϵ curve	Variation of T_0	Variation of Γ_0	Calculation Results
FD.X$*$	FD.A	FD.A	SR.X1$*$
FD.X$*$	FD.B	FD.B	SR.X2$*$
FD.X$*$	FD.C	FD.C	SR.X3$*$
FD.X$*$	FD.D	FD.D	SR.X4$*$

$*$X=A, B, C, or D, where A for calculation set A, B for calculation set B, etc.

Table 6.3: Case of study for different random distributions

The results for the case FD.C are shown in Fig. 6.16 and the assigned distributions are shown below the plotted curves. The global σ-ϵ curves for FD.C collapse to one. This trend in the global curves is similar to the results of model B. Such similarities are expected, as the frequency of occurrence of the σ-ϵ curves is the same for all the calculations under a particular model. That means, for RD.01, RD.02, and RD.03 in model B, an equal weight is given for all the σ-ϵ curves. On the other hand, for SR.C1, SR.C2, SR.C3, and SR.C4 in model C, all the σ-ϵ curves were assigned under the FD.C.

In model C, compared to model B, a considerable variation in the fracture stresses and strains was obtained, which resulted from the different frequency distributions of the fracture parameters. From the results it was shown that the influence of property variability on the global fracture behavior can be well described by frequency distribution functions rather than a constant (equal) distribution function.

In Fig. 6.17 all the results from FD.A, FD.B, FD.C, and FD.D are plotted. Each set shows coinciding elastic-plastic responses, which is, as mentioned before, due to the same distribution of σ-ϵ curves within one set.

The shift in the global σ-ϵ curves as well as the variation of the fracture stresses and strains are captured fairly well with the stochastic approach. An upper limit and a lower limit of the fracture stresses was obtained from each type of frequency distribution. The results show that the set SR.A results in a higher fracture strain than the set SR.B, which means that the fracture strain decreases with the increase of the curve stiffness.

The experimental and simulated variations of the fracture stresses and strains are compared in Fig. 6.18. The obtained experimental fracture points lie within the simulated results. The trend of the experimental fracture points match quite well with the SR.C results. This trend can only be confirmed by a number of experiments. Also, the assumed frequency distribution, FD.C, of the properties can be verified with the experimentally obtained variation band. Such experimental program was beyond the scope of the present work.

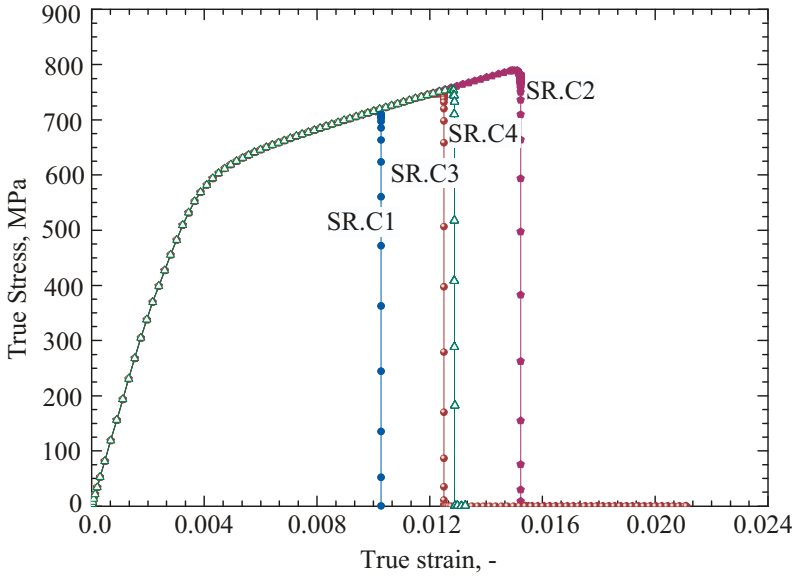

Parameters:

Variation σ–ε curves	Variation, T_0	Variation, Γ_0	Results
FD.C	FD.A	FD.A	SR.C1
FD.C	FD.B	FD.B	SR.C2
FD.C	FD.C	FD.C	SR.C3
FD.C	FD.D	FD.D	SR.C4

(FD = Frequency distribution; SR = Series of results)

Figure 6.16: Stress-strain curves for the calculation type C.

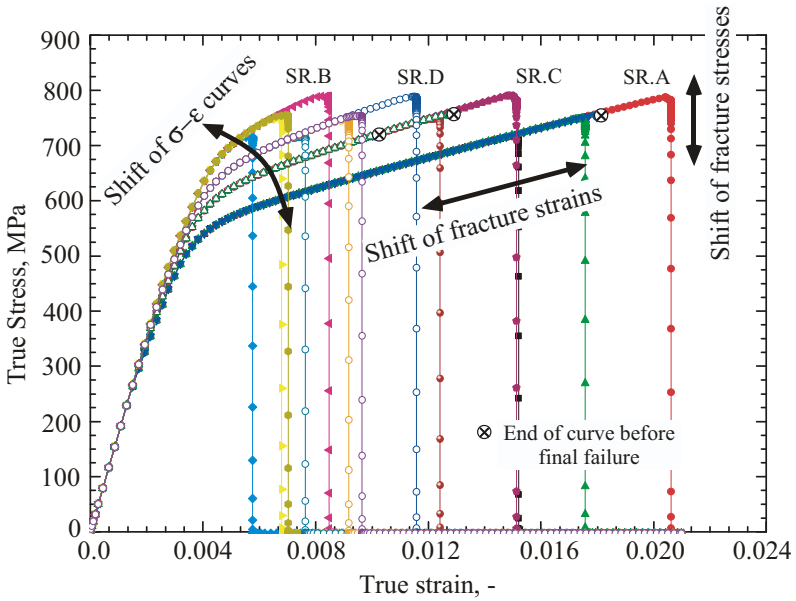

Figure 6.17: Simulated stress-strain curves obtained from various arrangements of the parameter distribution.

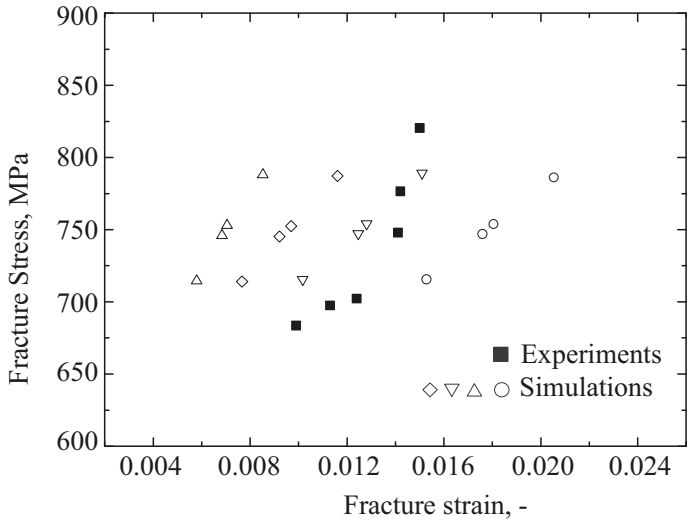

Figure 6.18: Comparison of numerical and experimental variation.

6.2.4 Simulation of tensile fracture using cohesive model

The tensile failure of brittle or quasi brittle materials occurs mostly dynamically, therefore, detailed information about crack initiation and propagation can not be easily obtained from experiments. Instead, the numerical simulations provide information about the local decohesion of material and degradation of stresses due to fracture. To access this information the numerical fracture under tensile loading for the model RD.01 are explained, and the influences of the local stress evolution on the crack propagation is discussed.

In Fig. 6.19 a magnified view of the simulated $\sigma-\epsilon$ curve at the maximum stress region is shown. The sharp stress drop at the vertical line is due to tensile damage. Three phases can be distinguished beyond the maximum stress level. These are marked on the global $\sigma-\epsilon$ curve.

Phase 1: Phase 1 can be phenomenologically interpreted as the start of material degradation or the damage process. At this point, the global force reduces during displacement controlled loading. The model can no longer carry external loads and the stress reduces at constant deformation. This displacement condition is marked by the increment 39 on a vertical tangent.

Phase 2: Further stress reduction occurs at constant displacement, marked by the "100" on the curve. In this calculation step, crack initiation occurred at a random block by breaking a cohesive element. Just after the first element breaks, the whole block starts to fail rapidly. Phase 2 ended by the failure of the first cohesive block.

Phase 3: Phase 2 is followed by multi-block failure. Within a short series of incremental steps, massive crack propagation along the fracture plane continues. All blocks fail either successively or simultaneously. There was no regular rule for the failure sequence, instead crack initiation

and propagation occurred in a stochastic nature, controlled by the distribution of the material parameters.

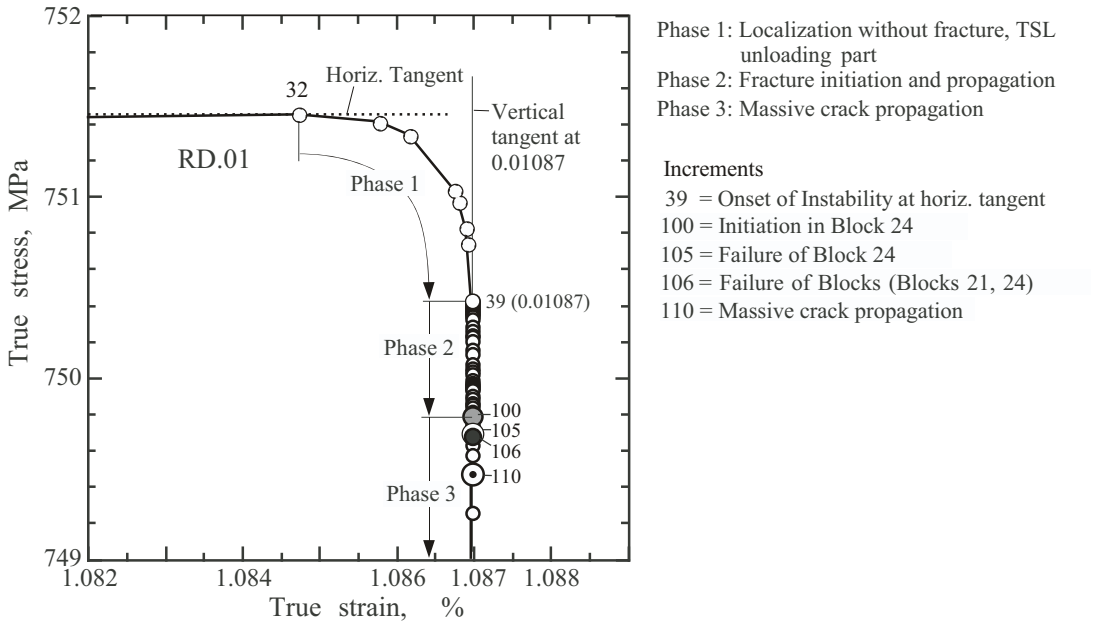

Figure 6.19: Magnified view of stress-strain curves for RD.01 beyond maximum stress levels, divided in three phases: damage like degradation, crack initiation in a block and the final massive crack propagation.

In Fig. 6.20 the local fracture strength evolution starting from the crack initiation to the final failure on the fracture plane is shown. For visual clarity the component stresses, σ_{22}, in the continuum elements near the fracture interface are shown. The σ_{22} in the continuum elements and the cohesive traction, T_0, in the cohesive elements (at the fracture plane) are equal.

Fig. 6.20(a) shows the stress contour at increment 32. The stresses in the continuum elements increase to a maximum level, as long as the cohesive law follows the ascending part up to a maximum traction, T_0. With further increase of the global displacement the blocks begin to soften following the softening part of the Rect-TSL. Consequently, the global force (or component stresses, σ_{22}) decreases. At the end of this progress (increment 39), the global displacement cannot be increased further due to the beginning of damage. Reduction of the global force along the vertical tangent occurs when the stresses, σ_{22}, decreases according to the last part of the Rect-TSL. As seen in Fig. 6.20(c), the first element breaks in block 24 (the local component stress σ_{22}, which is equivalent to T_0, is reduced to zero). This situation represents crack initiation in the FE model.

Just after the first cohesive element failure, local failure progresses for each cohesive element across the whole block (Fig. 6.20(d)).

This continuous fracture process causes further reduction of the external forces (Fig. 6.20(e)). The fracture continues producing massive irregular cracking throughout the cross section (Fig. 6.20(f)).

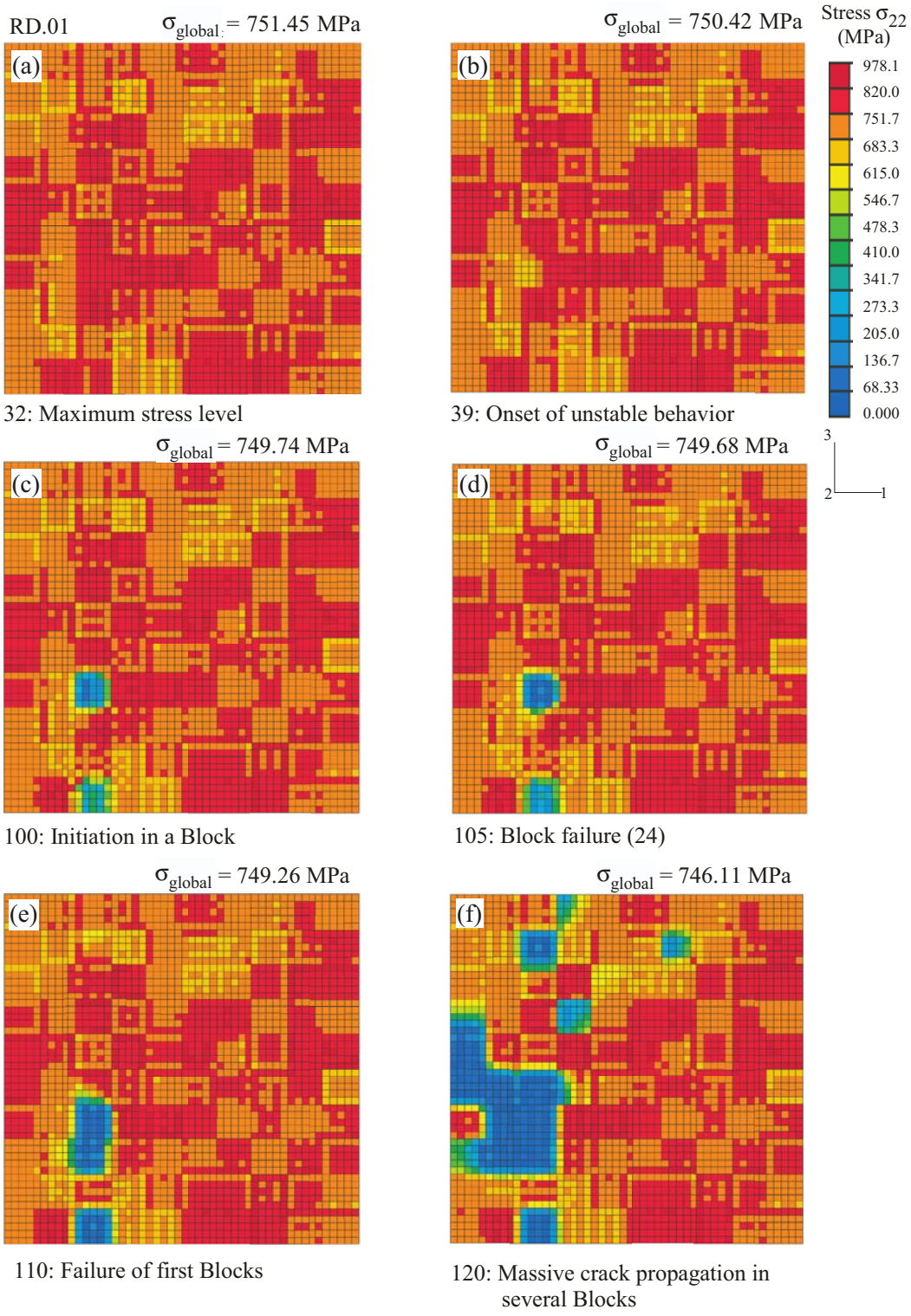

Figure 6.20: σ_{22} distribution of the simulation RD.01 across the fracture plane for characteristic loading steps showing the evolution of crack initiation and propagation: (a) for increment 32, (b) for increment 39, (c) for increment 100, (d) for increment 105, (e) for increment 110 (f) for increment 120.

The experimental force-displacement records exhibit only the initial part of Phase 1. However, the experimental stress-strain response is quite similar to the simulated one. In Fig. 6.21 two results of experimental $\sigma-\epsilon$ curves (belonging to the tensile tests ZQ4 and ZQ5) at and beyond their maximum stress levels are shown with a high magnified view. In both cases a plateau is reached which sustains over a small range at the strain axis. The simulated curves with the stochastic approach also show a narrow plateau at the maximum stress level followed by a vertical drop (Fig. 6.13 and Fig. 6.19). For the experiments, the very last data points just before failure can not be collected by the experimental setup. The curves are, therefore, tentatively extrapolated until a vertical tangent is reached.

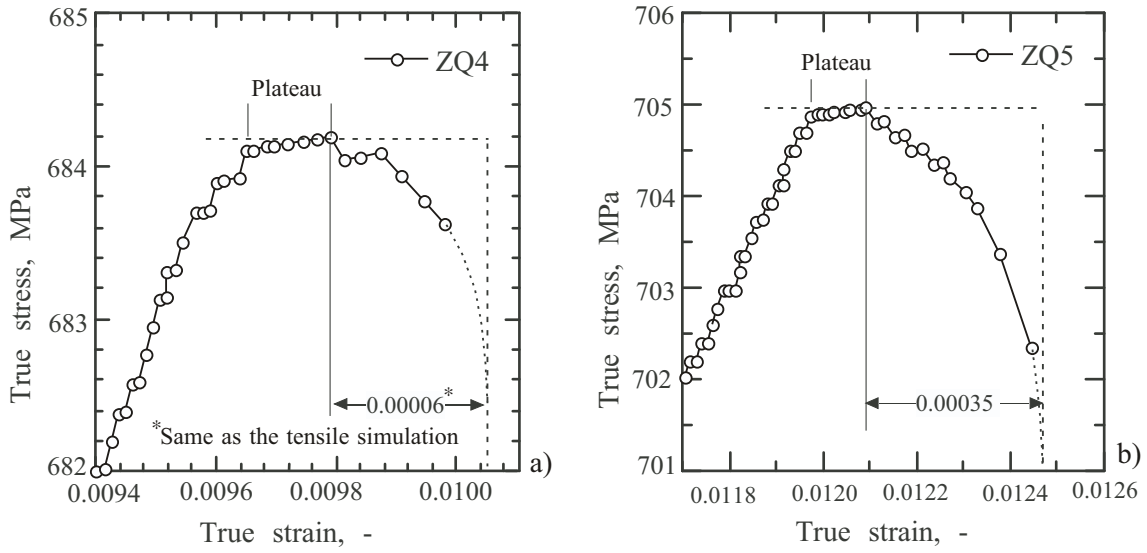

Figure 6.21: Magnification of stress-strain curves around maximum load of two tensile tests.

6.2.5 Local stress evolution

Following the evolution of damage in the hard and soft colonies in a lamellar microstructure is discussed. The meso-scale deformation of the hard and soft colonies were described by the higher and lower stress-strain curves (i.e., σ-ϵ.5 and σ-ϵ.1 curves). To obtain a better knowledge about the colony failure, interplay between the locally developed stresses and the material separation under the cohesive damage model have been discussed. For this purpose, a fracture model with RD.01 arrangement was used. Since the cohesive tractions, T, at the interface elements equal the normal stresses, σ_{22}, at the attached continuum elements, the normal stresses and strains at the attached continuum elements are studied. Additionally, elastic-plastic analyses (without fracture) were performed to compare the stress evolution in cracked and uncracked models.

For the investigation, four exemplary blocks were chosen among the 100 blocks: blocks 24 and 59 as hard colonies and blocks 52 and 68 as soft colonies. The blocks 24 and 59 were attributed to the highest $\sigma-\epsilon$ curve (curve $\sigma-\epsilon$.5). A higher fracture strength, T_0 = 802.43 MPa to block 24 and a lower fracture strength, T_0 = 689.93 MPa to block 59 were assigned. Similarly, the blocks 52 and 68

were attributed to the lowest $\sigma-\epsilon$ curve (curve $\sigma-\epsilon.1$). A higher fracture strength, T_0 = 803.54 MPa to block 52 and a lower fracture strength, T_0 = 686.92 MPa to block 68 were assigned.

The local evolution of stresses and strains in load direction (σ_{22}, and ϵ_{22}) for the fractured and deformed (without fracture) models are shown in Fig. 6.22(a) and Fig. 6.22(b)

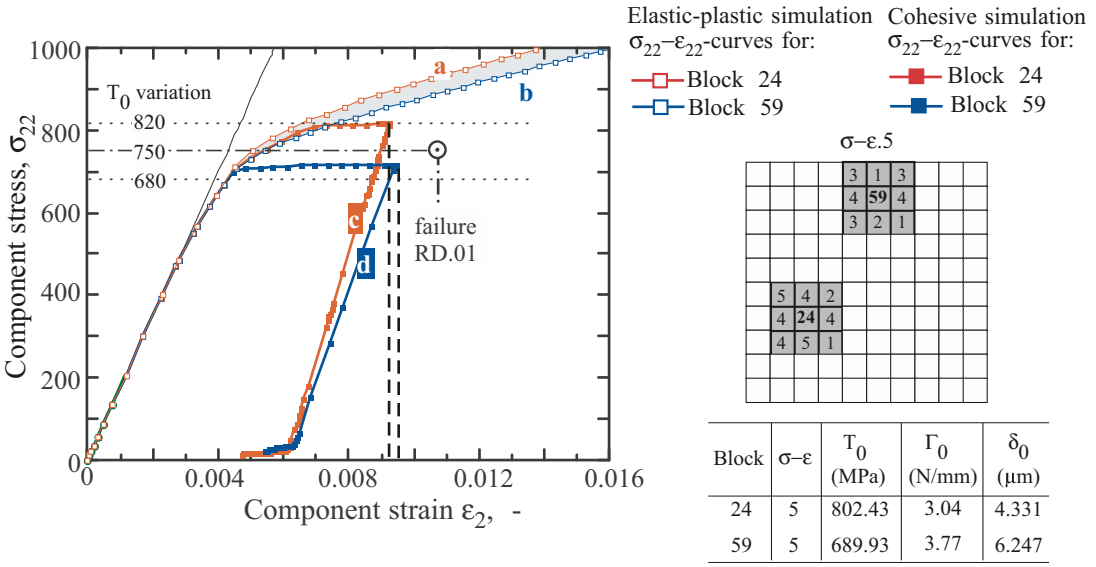

Block	σ–ε	T_0 (MPa)	Γ_0 (N/mm)	δ_0 (μm)
24	5	802.43	3.04	4.331
59	5	689.93	3.77	6.247

(a)

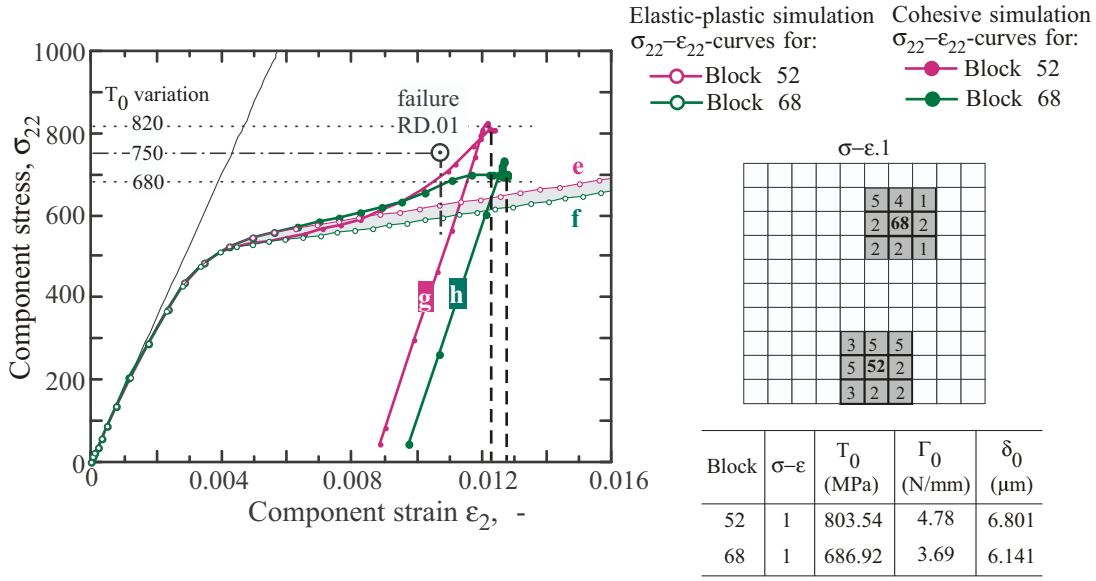

Block	σ–ε	T_0 (MPa)	Γ_0 (N/mm)	δ_0 (μm)
52	1	803.54	4.78	6.801
68	1	686.92	3.69	6.141

(b)

Figure 6.22: Activation of the component stresses σ_{22}: (a) for blocks 24 and 59 with σ-ϵ.5 curve, (b) for blocks 52 and 68 with σ-ϵ.1 curve, (c) view of the block positions and their assigned values.

In Fig. 6.22(a), two continuous σ_{22}-ϵ_{22} curves, a, b, (without stress degradation) for the hard colonies (blocks 24 and 59) are shown which resulted from the damage free models. The minor variation in

the hardening behavior (shown as a gray zone) of both blocks was due to the deformation constraint resulting from the neighboring colonies. Similar results were obtained from the soft colonies (curves e and f) as shown in Fig. 6.22(b). The yield stress of a and b is higher than the yield stress of e and f.

If fracture is introduced in the elastic-plastic model using only one set of T_0 and Γ_0 (without stochastic T_0 and Γ_0 under the variation band), the evolution of σ_{22} and ϵ_{22} would be similar to the previous cases (curve a,b or e,f) until the σ_{22}-ϵ_{22} curve is truncated by the cohesive parameters. The required ϵ_{22} to attain σ_{22} depends on the local higher or lower σ_{22}-ϵ_{22} curves, i.e., the curves with higher or lower yield stress. For example, for a higher σ_{22}-ϵ_{22} curve (curve a or b), a lower ϵ_{22} is required to attain the maximum σ_{22} corresponding to T_0. For a lower σ_{22}-ϵ_{22} curve (curve e or f), a large ϵ_{22} is required to gain the same maximum σ_{22} corresponding to T_0.

If fracture is introduced by a random set of T_0 and Γ_0 values, the evolution of σ_{22} and ϵ_{22} will be quite different from the previous cases of a single set of T_0 and Γ_0. In this case, the local σ_{22} and ϵ_{22} developments will be highly influenced by the deformation constraint of the poly-colonies. Such cases are shown in Fig. 6.22(a) with c and d curves, and in Fig. 6.22(b) with g and h curves.

For the curves c and d, a higher σ-ϵ.5 was attributed to the hard colonies. Therefore, less ϵ_{22} was sufficient to increases the σ_{22} up to the equivalent stress to fracture (T_0 = 802 and 689.93). The colony was deformed pure plastically until the stress begins to fall down due to damage evolution. On the other hand, for the curves g and h corresponding to soft colonies, larger local strains, ϵ_{22} should be needed to achieve the required fracture stresses defined by the cohesive tractions, T_0. But larger ϵ_{22} can not be achieved in the model as the ϵ_{22} can not increase freely due to the deformation constraint of the colonies. Rather, the local stress, σ_{22}, increased sharply to gain the required fracture stress, T_0.

Thus, it can be shown that the required ϵ_{22} to attain σ_{22} for crack initiation is notably influenced by the deformation constraint of the colonies. This phenomenon can not be captured if the fracture surface is completely described by a single set of cohesive parameters, which basically simulates a homogeneous crack propagation without the influence of colony fracture properties. The stochastic approach simulates the crack initiation in a polycrystal quite realistically and provides a meaningful explanation about the role of inhomogeneous stress development to initiate cracks.

6.2.6 Generation of random crack

In Fig. 6.23 the nodal displacement, U2, along the loading direction at the fracture plane of RD.01 (Model B) is shown. The separations, δ, of the cohesive elements are equals the U2 for the continuum elements at the fracture interface. Due to the symmetric model, the plotted U2 is equal to δ/2. In the figure the attained U2 is shown on the right hand side and the colored contours are shown on the left hand side.

The smallest value of δ_0 (δ_0 = 4.93 μm) was attributed to block 24 during random data assignment which initiated the first crack in the model. As the δ follows the TSL of the cohesive model, the evolution of δ is dependent on the evolution of the T. The evolution of the T is again influenced

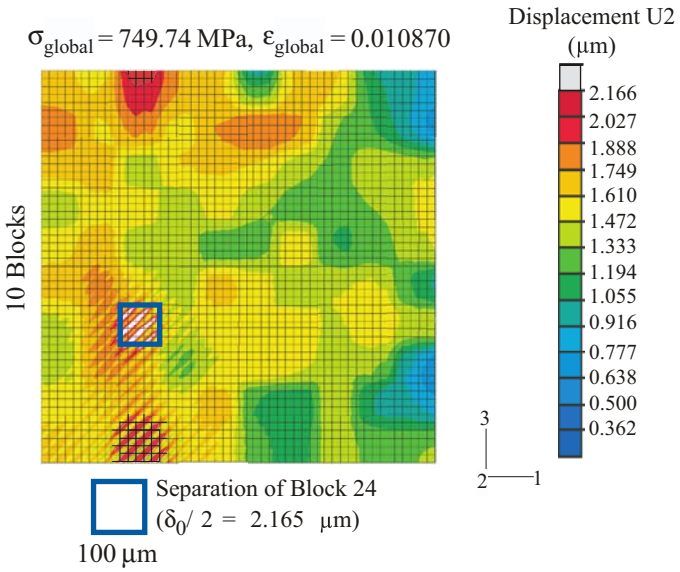

Figure 6.23: Displacement contours of the simulation RD.01 along the cohesive layer displaying the cohesive separation across the fracture plane, crack initiation occurs in block 24.

by the locally defined elastic-plastic behavior of the colonies as well as the deformation constraint imposed by the neighboring blocks. Thus, the crack initiation is correlated to the local deformation and evolution of stress at the fracture surface.

The stress distributions, σ_{22}, across the fracture plane at the beginning of a block failure for the stochastic cases of RD.01, RD.02, and RD.03 are shown in Fig. 6.24. The stochastic values were kept same for RD.01, RD.02, and RD.03 but were differently distributed throughout the fracture surfaces. The figure shows that the initiation of cracks in all cases occur at different blocks, which clearly proves that the random location of crack initiation results from the heterogeneous deformation described by the random elastic-plastic curves of the colonies.

6.2.7 Concluding remark

Tensile failure of γTAB with lamellar microstructure has been described phenomenologically using the cohesive model. Adopting the stochastic assumptions for property variability, the mechanisms of failure are explained fairly well as well as the experimental scatter is captured in an acceptable range. It has been shown that the distribution functions for assigning the random parameters into the model significantly influence the global tensile responses. The polycrystal deformation and failure are also realistically predicted. The results show that the local deformation constraint plays an important role for attaining required local stresses for crack initiation. The crack initiation is found to be mostly stochastic in nature. After the initiation of a crack load drops rapidly, which can be seen at the vertical tangent of the global $\sigma-\epsilon$ curve. Crack propagates dynamically at this line. It has been found that the rapid crack propagation begins just after the failure of a single element.

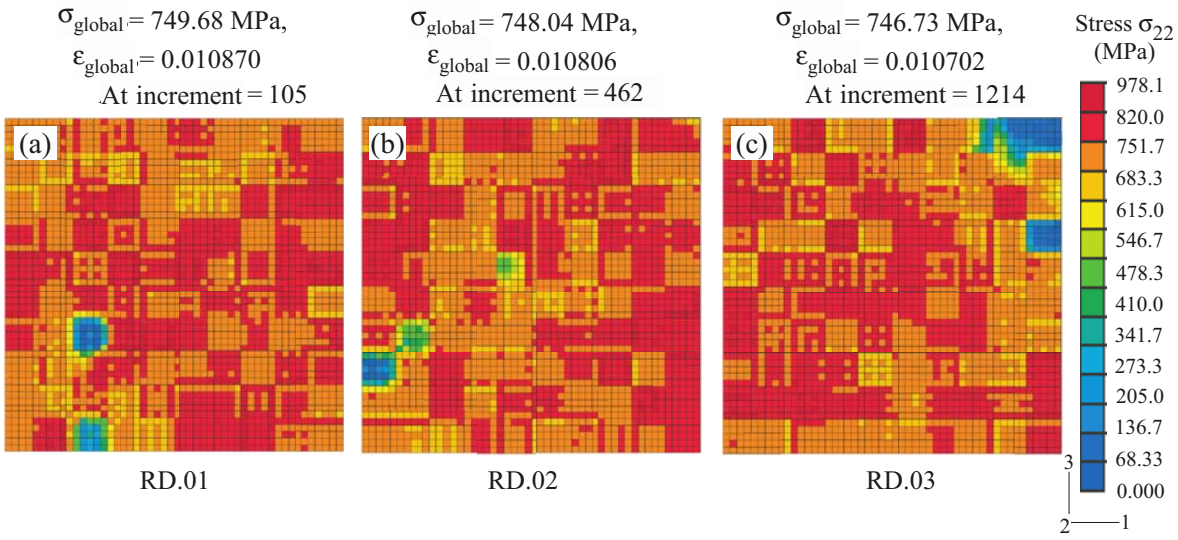

Figure 6.24: σ_{22} distribution of the stochastic simulation RD.01, RD02, RD.03 showing the initiation in different blocks.

The influence of the stochastic property variation on the crack initiation and propagation can be understood more clearly by analyzing a stable crack propagation. Such a controlled crack propagation can be obtained through fracture testing of notched bend specimens. In the next section the stochastic approach is validated comparing the scatter in the experimental and simulated force-displacement curves obtained from the chevron notched bend specimens.

6.3 Verification of the stochastic approach on chevron notched bend specimens

In this section the crack propagation through lamellar colonies and the sudden failure of specimens (as seen during fracture testing) are interpreted with the help of numerical simulations. Influences of the fracture parameters on the scatter of experimental force-displacement curves are investigated. Chevron notched bend specimens are used for the investigation.

6.3.1 Meshing of the chevron notched bend specimen

A 3D symmetric model of the chevron notched bend specimen was constructed as shown in Fig. 6.25. The triangular fracture plane was placed at the symmetry plane. Zero-thickness interface cohesive elements with 20 μm x 20 μm cross section are attached to the triangular plane. Adjacent to the fracture plane 8-noded brick-like continuum solid elements were chosen, each of which has the same size as the cohesive element. In such quadratic mesh a slightly jagged edge remains along the notch-edge of the triangular ligament. This jagged edge has no significant influence on the numerical crack propagation as well as the development of stress, strain and displacement fields.

To simulate the colony fracture the fracture plane was divided into100 μm x 100 μm blocks (analogous to the size of lamellar colonies in γTAB polycrystal). Each block contained 25 quadratic cohesive elements.

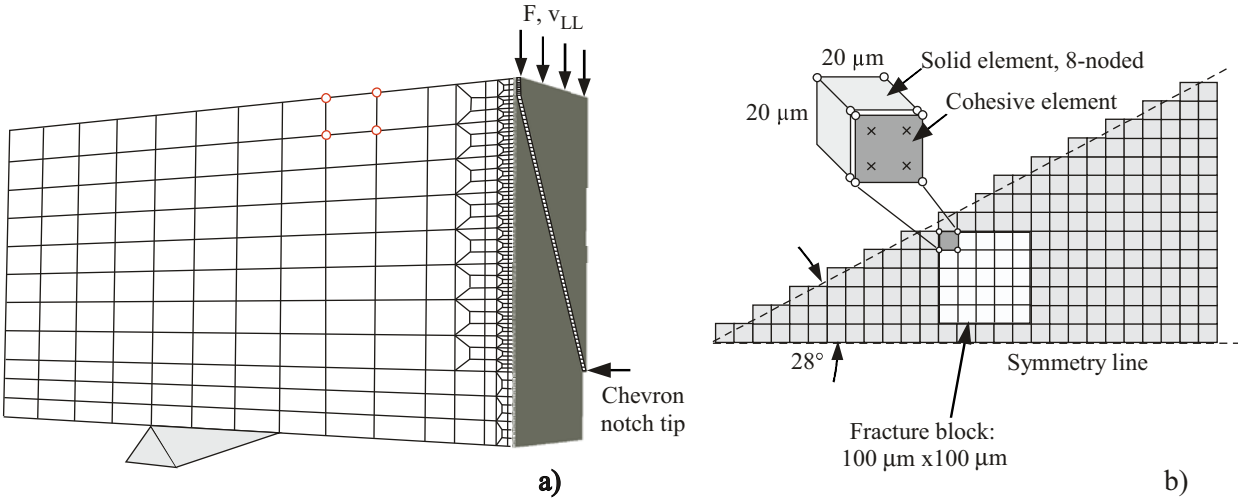

Figure 6.25: FE model with mesh design and stochastic blocks for the chevron notched bend specimen.

6.3.2 Simulation with a single set of cohesive parameters

In this investigation fracture was described by a set of fixed fracture parameters, T_0 and Γ_0. The parameters were distributed uniformly throughout the fracture surface. With this single set of parameters the fracture surface was considered to be homogeneous. The effect of lamellar orientations on the crack propagation was neglected. Such simplified assumptions are useful to identify the principal effects of cohesive parameters on the global fracture response. Also, basic information about the variation band of the fracture properties can be obtained.

A Rect-TSL was used for the fracture simulation. The bulk material above the fracture plane was described by the classical isotropic von Mises yield criterion. In Chapter 5, the average Γ_0 was determined as 4 N/mm. From the tensile experiments the average T_0 was found to be 750 MPa. The values were considered as mean values of the variation band.

The variation band of Γ_0 is determined by comparing the experimental and simulated crack initiation from the chevron notched bend specimens. For this purpose simulations were performed keeping the T_0 = 750 MPa and changing the Γ_0 from 3 to 5 N/mm. Crack initiations in the simulations were defined at the point where more than two cohesive elements were broken. These elements were confined to the first colony at the chevron notch tip. As at the notch tip only one block is involved, the initiation of crack is significantly influenced by the notch-tip colony behavior.

In Fig. 6.26(a) the simulated F-v_{LL} curves are shown. For some cases a continuous growth of crack-front was obtained that shows a gradual reduction of force, for example, in the case of Γ_0=3.75, 4, 5 and 8 N/mm. The continuous growth of crack during increasing deformation can be termed as “stable crack propagation”. For the other cases (Γ_0 lower than 3.35 N/mm), the crack propagation stopped during increasing deformation. Numerical calculation was cut off due to the model instability. This situation can be interpreted as sudden failure of the specimen.

The simulations show that the deformation controlled crack propagation varies with the Γ_0-values. With decreasing Γ_0, the load-displacement curves change from continuous softening to sudden failure. The transition lies close to Γ_0 = 3.75 N/mm, shown as a gray zone in Fig. 6.26(a). Also, small load-drops (pop-in) were observed. In this calculation a pop-in is defined as a global vertical load drop at a constant (non-increasing) load-line displacement, v_{LL}. After a final load drop the load can increase again, and the crack can propagate further in a stable manner. During pop-in, the traction in the cohesive elements soften to zero according to the third part of the Rect-TSL. However, the global load-line displacement, v_{LL}, remains unchanged. In reality, the pop-in is a dynamic load drop at non-increasing v_{LL} due to local material instability. The numerical pop-in depends on the loading system and the material properties, i.e., the cohesive parameters T_0 and Γ_0.

The numerical pop-ins for different Γ_0 are depicted in Fig. 6.26(b). The pop-in phenomena depend on the Γ_0. The first pop-ins occur at a certain applied v_{LL}. For further increment of v_{LL} a second pop-in may arise or the curve may end by a final load-drop. For Γ_0 = 3.33 N/mm, sudden failure has been observed at the first relatively large pop-in. With somewhat increased Γ_0 (Γ_0 = 3.75 N/mm), still

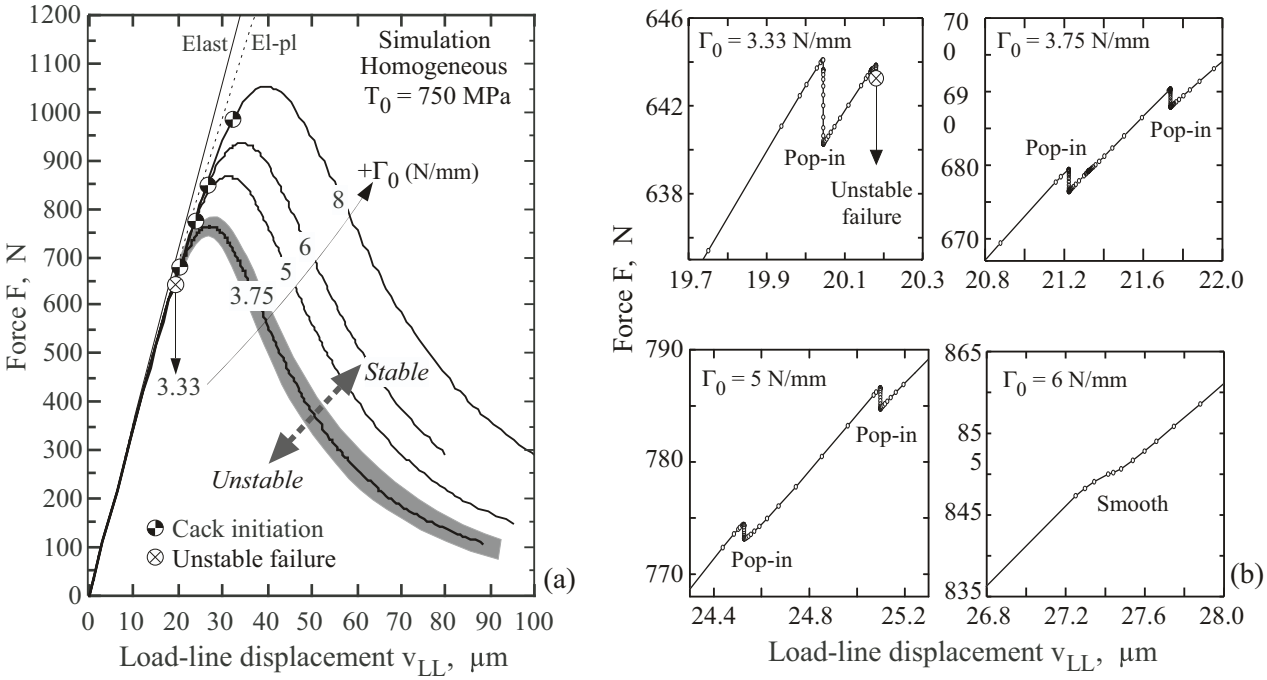

Figure 6.26: Simulations of chevron notched bend specimens with homogeneous cohesive parameters and average elastic-plastic bulk behavior: (a) influence of Γ_0 on the global behavior, (b) numerical pop-in effects emerging in the curves.

relatively large pop-ins were obtained, which did not lead to unstable failure. After this pop-in the crack propagation proceeded further in a stable manner.

The pop-in phenomenon gradually vanishes with further increase of Γ_0. For example, a smaller pop-in was observed for $\Gamma_0 = 5$ N/mm and it vanished completely beyond $\Gamma_0 = 6$ N/mm.

In Table 6.4, cohesive parameters and the simulation results are summarized.

Case	T_0, MPa	Γ_0, N/mm	δ_0, μm	F-v_{LL} behavior
1	750	3.33	5.07	Sudden failure
2	750	3.75	5.72	Continuous softening, significant pop-in
3	750	5.00	7.62	Continuous softening, reduced pop-in
4	750	6.00	9.15	Continuous softening, pop-in smoothed
5	750	8.00	12.19	Continuous softening, without pop-in

Table 6.4: Simulations with homogeneous cohesive parameters

In all simulations, ABAQUS [76] “Stabilization Parameter” has been applied. This control parameter enables one to simulate pop-ins or sudden failure. The stabilization parameter initiates an artificial damping on the FE model at the onset of an unstable condition. Due to the artificial damping, the solution can proceed further at a constant load-line displacement, v_{LL}, showing vertical load drop.

In a statically loaded system no equilibrium in the numerical solutions can be found during vertical

load drop. Simulations without stabilization parameter stop generally at the onset of an unstable condition. On the other hand, the artificial stabilization parameter promotes reduction of internal stresses in the cohesive elements at a fixed global displacement. The action leads to a vertical load drop in the global F-v_{LL} curve. Further load drop progresses with the incremental steps till a next equilibrium condition.

The stabilization parameters have to be chosen according to the model geometry and the loading system. The default parameter determined by ABAQUS for the pre-notched specimen is able to generate a quasi-stable equilibrium condition at least for small load drops. For large load drops the calculation stops at intermediate incremental steps. Many incremental steps can be produced along the fixed global displacement. Such situation is observed in the simulation curve with Γ_0 = 3.33 N/mm.

The experimental curves of the tested chevron notched bend specimens (CV1-CV8) are plotted in Fig. 6.27 together with the simulations of homogeneous cohesive parameters. The experimental scatter lies within the simulated curves of Γ_0 = 3-5 N/mm. The curve for Γ_0 = 6 N/mm is not included, as the simulated maximum load is far beyond the experimental one. Below Γ_0 = 3 N/mm, the simulation predicts unstable failure that occurred at the elastic slope. The maximum achieved load is pretty lower than the experimental maximums. Equivalently, the forces at crack initiation as indicated in Fig. 6.26(a), lie in the same range as the experimental ones.

The Γ_0 within the variation 3-5 N/mm satisfies the experimental observation qualitatively with respect to pop-in and sudden failure. The range 3-5 N/mm can be taken as a valid variation band for Γ_0.

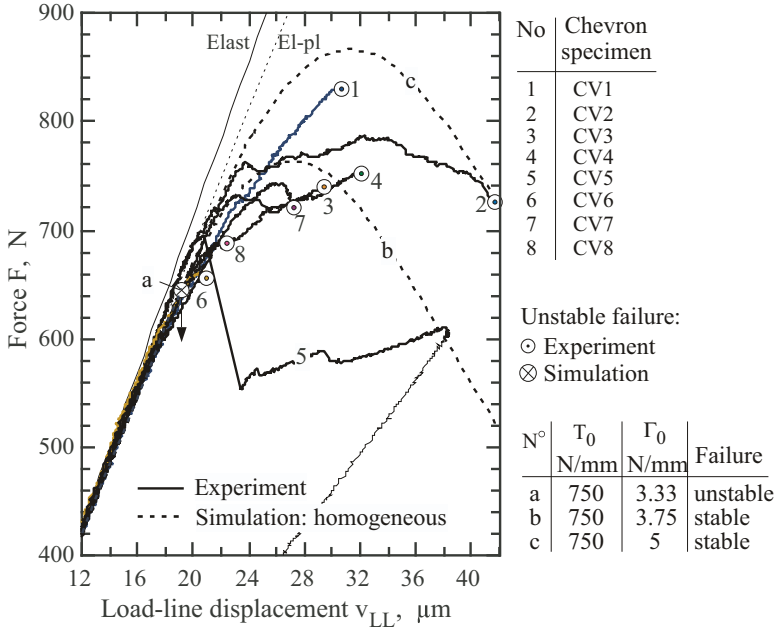

No	Chevron specimen
1	CV1
2	CV2
3	CV3
4	CV4
5	CV5
6	CV6
7	CV7
8	CV8

Unstable failure:
⊙ Experiment
⊗ Simulation

N°	T_0 N/mm	Γ_0 N/mm	Failure
a	750	3.33	unstable
b	750	3.75	stable
c	750	5	stable

Figure 6.27: Comparison of experiments, 1-8, and simulations with homogeneous parameters, a-c.

6.3.3 Fracture simulation with stochastic cohesive parameters

The features of the F-v_{LL} curves, e.g., the saw-tooth irregularity in the F-v_{LL} curves with pop-in phenomena, the different locations of the maximum loads, and irregularly occurring sudden failure are due to translamellar crack propagation through the randomly oriented lamellar microstructure. From the previous analysis of a homogeneous fracture surface such characteristic features of the global curves have not been captured in detail.

The necessity of implementing random cohesive parameters on the fracture surface is obvious. Such random properties may describe the underlying principle of crack propagation through the γTAB polycrystal. Therefore, in the following section details of the stochastic approach will be verified on the chevron notched bend specimen.

In this approach, the randomly oriented colonies in a polycrystal and their contributions to fracture were described with the random representation of cohesive parameters. The stochastic parameters and their distributions were generated as described for the tensile specimens in section 6.2.2. The T_0 and Γ_0-parameters used in the simulations are as follows:

T_0, MPa	Average value	750	taken from the average fracture strength (from the tensile tests)
	Variation band	680-820	taken from the variation band of the fracture strengths (from the tensile tests)
Γ_0, N/mm	Average value	4	From simulations with homogeneous parameters
	Variation band	3-5	From simulations and experimental comparison of chevron notched bending tests

Table 6.5: Selected cohesive parameters

Here, the fracture process was fully attributed to the cohesive parameters without any influence of the variation of stress-strain curves in continuum elements above the fracture surface. Simulations with both the variation of stress-strain and cohesive parameters will be discussed in section 6.3.4.

A sample arrangement of the parameter variation for T_0 and Γ_0, are depicted in Fig. 6.28(a,b). In Fig. 6.28(b) the assigned random cohesive parameter values in each block were shown in different color columns. The parameter variations can be clearly seen from a 3D view, as shown in Fig. 6.29(a,b), where the stochastic values of each block were plotted for T_0 and Γ_0 respectively.

Several simulations are performed from which only three random arrangements are selected. They are denoted as RC1, RC2, and RC3. The stochastic analysis requires a number of simulations to accommodate the experimental scatter. To reduce the numerical efforts, some manually selected changes on the parameter distribution have been performed at the chevron notch tip. However, this particular selection is related to the microstructural information of colonies at the chevron notch tip.

In agreement to the observations, some cohesive parameters are manually re-ordered to some par-

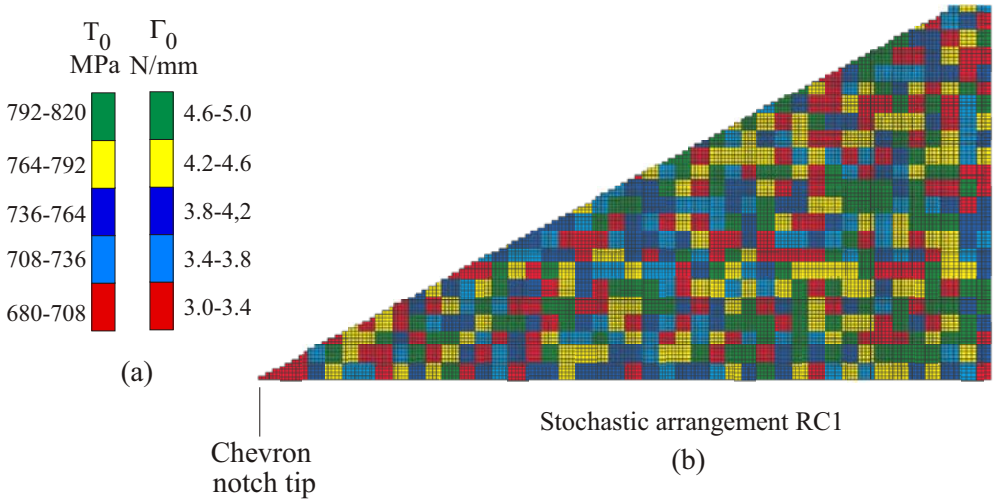

Figure 6.28: Stochastic arrangement of quadratic blocks: (a) variation band of the cohesive parameters, T_0 and Γ_0, (b) spatial stochastic arrangement, RC1, with blocks of 100 μm x 100 μm and their color depiction of the column levels for Γ_0-values.

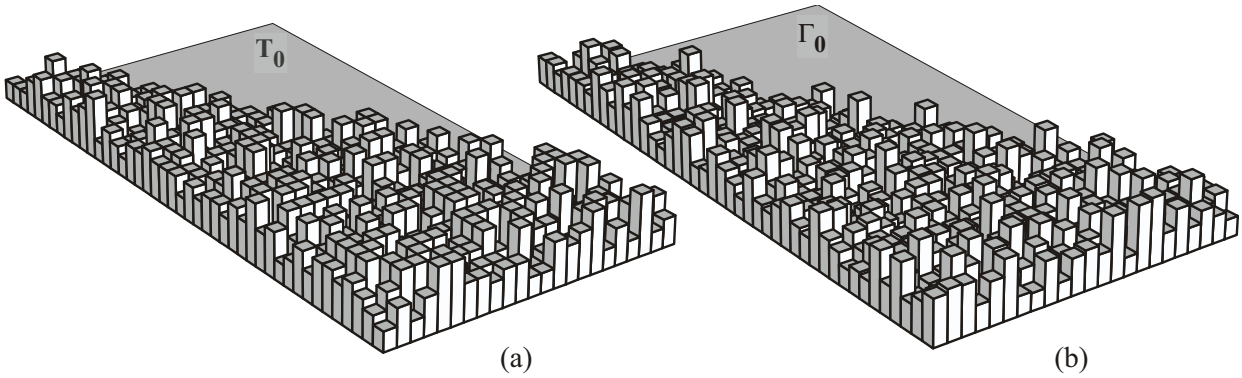

Figure 6.29: 3D view of the stochastic arrangement of the cohesive parameter variation for RC1: (a) for cohesive traction, T_0, (b) for cohesive energy, Γ_0.

ticular blocks adjacent to the chevron notch tip. Lower or higher values of cohesive parameters are manually implemented at the notch tip, which will represent the effect of weaker or stronger colonies. This manual re-distribution is considered as one occurrence among many randomly mixed parameters, all of which can not be simulated due to computational expenses.

In Fig. 6.30(a), the F-v_{LL} curves from the stochastic parameters and the single set parameters are shown. It clearly demonstrates that uniform parameters are not able to predict the experimental curves properly, whereas the curves from the stochastic approach cover all experimental aspects, like pop-in, variations in sudden failure, different extensions of load-line displacements and different maximum loads.

The Fig. 6.30(b) presents a comparison of the simulations for three different random arrangements,

RC1, RC2, RC3, with the experimental curves. The simulated results from the stochastic approach satisfy the experimental scatter of F-v_{LL} curves. They lie within the experimental variation band. The zigzag nature during crack propagation, the pop-in phenomena, the sudden failure either early or later, is described in a right order.

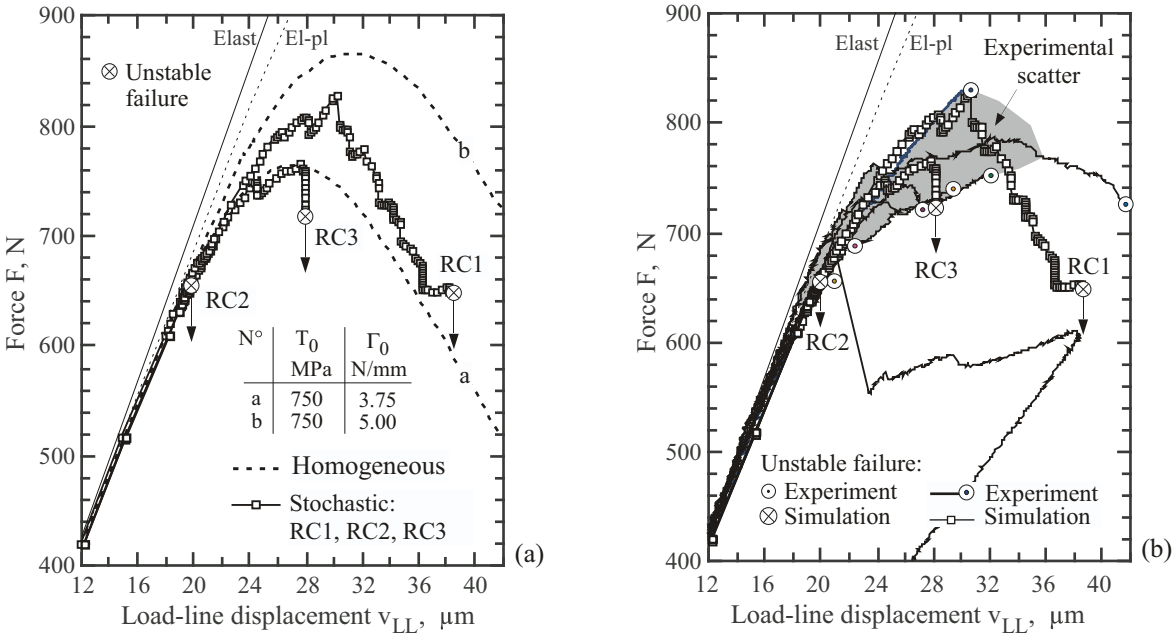

Figure 6.30: Comparison of simulations and experiments of chevron notched bend specimens: (a) simulations with homogeneously and stochastically distributed cohesive parameters, (b) simulations with stochastic approach and experiments.

Simulation with the arrangement RC1 exhibits a long extended continuous F-v_{LL} curve. On the decreasing part beyond maximum load, the calculation stops at a certain point which is interpreted as sudden failure of the specimen, i.e., equilibrium is no more reached in the last increment. At the chevron notch tip relatively weak cohesive parameters (lower value combinations of T_0 and Γ_0) were situated, which promoted stable crack propagation after crack initiation. A lower cohesive traction, T_0, allows the break of the first few blocks adjacent to the chevron notch tip.

In arrangement RC1, a rugged crack front is obtained during subsequent crack propagation. Here, the blocks with higher parameters behave like obstacles and promote pop-in when high stresses relax according to the third part of the Rect-TSL. Numerical pop-ins occurred during stress reduction of a hard colony.

Due to the neighboring blocks of different parameter sets, the crack can propagate continuously by increasing the stresses in neighboring blocks. Along the decreasing part of the F-v_{LL} curve, the crack front may stop at a point where an increasing width of the crack front causes sudden failure.

In contrast to arrangement RC1, the RC2 exhibits sudden failure just after crack initiation (Fig. 6.30). Higher values of T_0 combined with smaller values for Γ_0 were assigned at the notch tip. Just after

breaking the first cohesive elements the calculation terminated, even with the ABAQUS stabilization parameters.

In the case of arrangement RC3, some moderate values of T_0 and Γ_0 were attributed in several blocks at the chevron notch tip. There were also some "hard" combinations (higher T_0 and Γ_0 values) of the cohesive parameters situated just after the notch tip. From Fig. 6.30(b), it can be seen that the calculation for RC3 terminates anywhere in between the limit borders of RC1 ("soft" initiation) and RC2 ("hard" initiation). Sudden failure at various v_{LL} can thus be simulated using the random arrangement of weak and strong combination of T_0 and Γ_0. Thus, controlling only a few blocks at the chevron notch tip the experimental fracture behavior can be globally satisfied fairly well without performing a huge number of calculations with different random arrangements.

In Fig. 6.31, the F-v_{LL} response for arrangement RC1 is plotted together with the corresponding crack front evolution. The random approach produces an irregular crack front until the model shows a non-equilibrium condition (which is interpreted as sudden failure of a specimen).

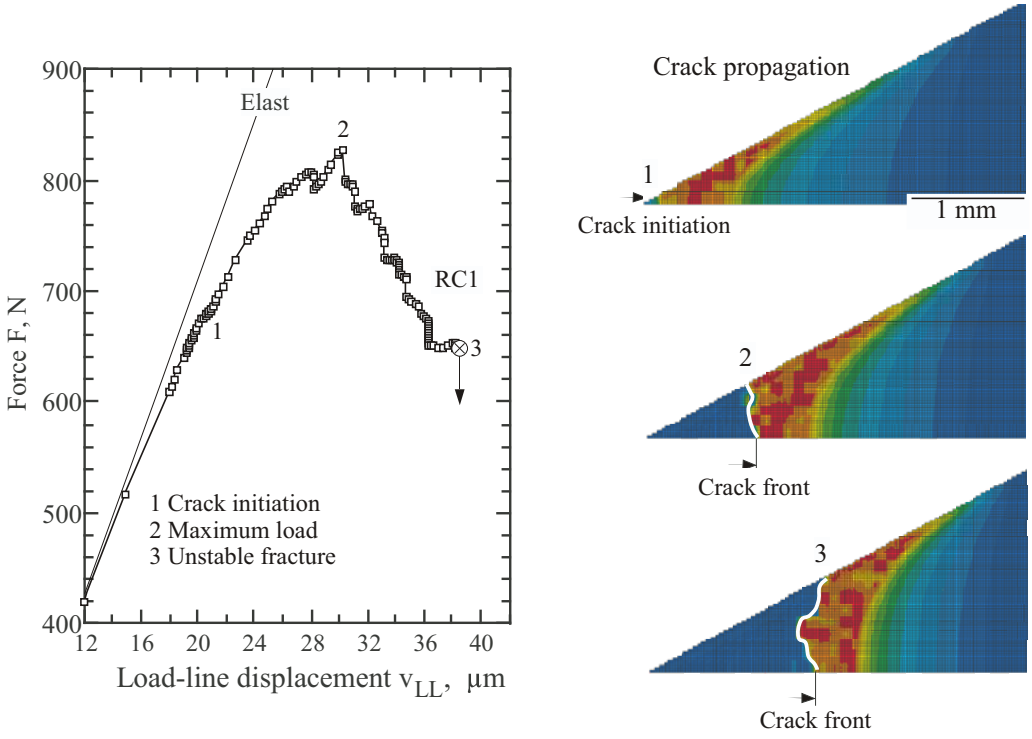

Figure 6.31: Crack propagation at three loading steps for stochastic arrangement RC1.

The three simulations RC1, RC2 and RC3 provide information about the influence of the variability of material properties on crack propagation and resulting F-v_{LL} curves. A particular experimental curve can be satisfied by changing the material parameters based on the knowledge of previous three calculations. In Fig. 6.32(a), the F-v_{LL} curve of an additional arrangement RC4 is plotted and compared with the experimental records of specimen CV3. These arrangements were changed manually not only adjacent to the chevron notch tip but also somewhere inside the fracture plane. The crack

initiation and maximum load is still higher compared to the experiment. The experimental lower load was due to the pre-damage at the notch tip which promotes easy crack initiation. This kind of material defects came from specimen preparation. Such effects were not considered in the numerical model.

In the specimen the fracture process contains interlamellar cleavage facets inside the first colony at the chevron notch tip, see Fig. 6.32(b). This may be due to the specific lamellae orientation allowing for interlamellar fracture. For a pure interlamellar fracture, the Γ_0 is very low in general which is approximately in the range of 0.05-0.1 N/mm. In the FE model no such weak interlamellar fracture parameter is included within a colony. A colony always takes a single set of cohesive parameters without considering explicitly micro-level fracture parameters. The lower limit of the variation band for Γ_0 is 3.0 N/mm, which is appropriate for translamellar fracture in the colony of γTAB polycrystal but is much higher compared to the pure interlamellar fracture resistance.

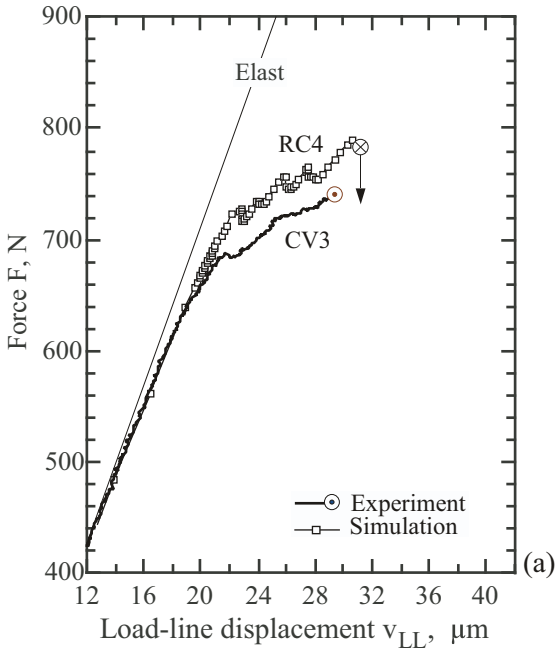

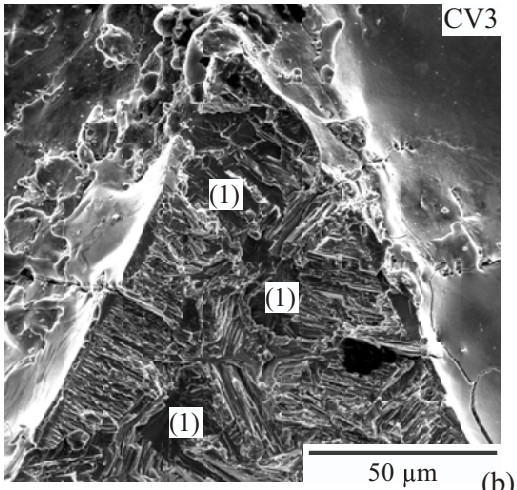

(1) Interlamellar fracture facets

Figure 6.32: Stochastic distribution with respect to interlamellar fracture adjacent to the chevron notch tip taken from specimen CV3: (a) comparison of the simulation for arrangement RC4 with the record of specimen CV3, (b) microstructural detail at the chevron notch tip of the fracture surface of specimen CV3.

In Fig. 6.33, the experimental and numerical fracture surfaces for specimen CV1 and simulation RC1 are compared. The results are taken at the point of failure. An almost similar crack front was obtained from the simulation. At the onset of unstable failure the simulated crack length was found to be 0.96 mm, which is close to the experimentally determined crack length of 1.04 mm.

The above results indicate that the stochastic random arrangements of cohesive parameters are able to predict the behavior of experimental curves almost entirely. An exact agreement with the experimental curves is, however, not possible as the macro scale simulations do not take the real microstructure,

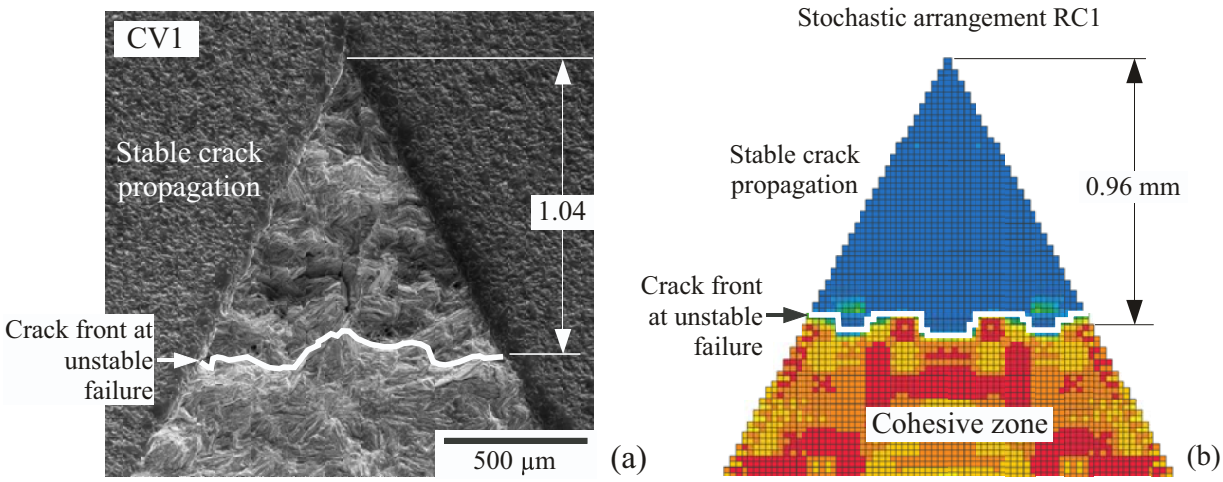

Figure 6.33: Specimen CV1: (a) fracture surface at the end of the test, (b) simulated fracture surface for stochastic arrangement RC1 at unstable failure.

its local crystallographic deformation and fracture features into consideration. Nevertheless, the hypothesis about the random distribution of cohesive traction, T_0, and cohesive energy, Γ_0, under the stochastic approach as well as the assumptions of colony-sized blocks is sufficient to capture the quasi-brittle fracture. The fracture characteristics, even for the complicated lamellar microstruture, can be well reproduced on the macro scale.

6.3.4 Simulation with stochastic cohesive parameters and variable stress-strain curves

The local stress development near the fracture surface is influenced by the deformation behavior of colonies. The variation of local stress-strain curves at the colonies produces inhomogeneous stress states that may influence the initiation of cracks. To verify this influence, variable $\sigma-\epsilon$-curves are applied in the colonies near the fracture surface.

To apply the stochastic concept with variations of $\sigma-\epsilon$ curves, several layers of continuum elements above the cohesive elements were selected from the chevron model, see Fig. 6.34. The size of continuum elements and cohesive elements at the fracture surface was 20 μm x 20 μm. 100 μm x 100 μm blocks were constructed with cohesive and continuum elements that represent simplified lamellar colonies. The choice of the $\sigma-\epsilon$ variation and their random distributions were the same as in the simulation of the tensile specimens (section 6.2).

To comprehend the effects of $\sigma-\epsilon$ variations a model RD1 was established. The RD1 had exactly the same distribution of T_0 and Γ_0 as the model RC1. The only difference between them is the mechanical behavior of continuum elements above the fracture plane. In RD1 five σ-ϵ-curves were distributed at the continuum blocks near the fracture surface that result in inhomogeneous stresses near the fracture process zone (FPZ), whereas in RC1 only the average σ-ϵ curve (σ-ϵ.Mid) was attributed which generate a homogeneous stress at the FPZ.

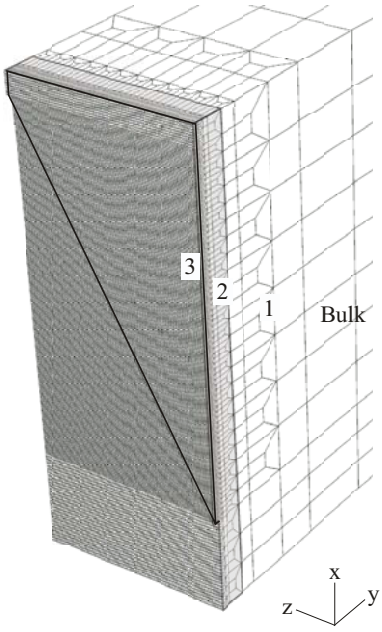

Layer

1 Homogeneous bulk, average σ–ε curve (σ–ε.Mid ≅ σ–ε.3)
2 Stochastic variation of σ–ε curves (σ–ε.1 to σ–ε.5)
3 Cohesive interface

Figure 6.34: Chevron notched bend specimen including a layer of stochastic distributed stress-strain curves above the cohesive interface.

The simulated global F-v_{LL} curves are shown in Fig. 6.35(a,b). Both the arrangements RC1 and RD1 showed coinciding F-v_{LL} curves up to the maximum load. For arrangement RD1, sudden failure occurred just after reaching the maximum load whereas in arrangement RC1 stable crack propagation continued beyond the maximum load.

In Fig. 6.35(b), the F-v_{LL} curves of both random arrangements, RC1 and RD1, are shown in an enlarged window where the onset of cracks can be seen. The pop-ins in RD1 occurred earlier than the RC1. This slight change in pop-ins is due to the inhomogeneous stress states that resulted from the variable $\sigma\epsilon$-curves at the notch-tip.

The local variation of $\sigma-\epsilon$ curves has no immediate effect on the global response except for the final failure points on the curves. Differences in local stress and strain development are observed only locally at the fracture plane.

From Fig. 6.36(a-d), the stress and strain fields in the continuum elements above the cohesive layer are depicted for both arrangements (RC1 and RD1) at the last load increment of RD1, just before the failure point (v_{LL} = 30.6 μm). The figure shows slight differences in stress and strain fields as well as in crack fronts, which are due to the variation in local σ-ϵ-curves. A higher local $\sigma-\epsilon$-curve in a block produces higher stresses at lower strains, in contrast to a lower local $\sigma-\epsilon$ curve, which eventually influences the evolution of T(δ) and δ.

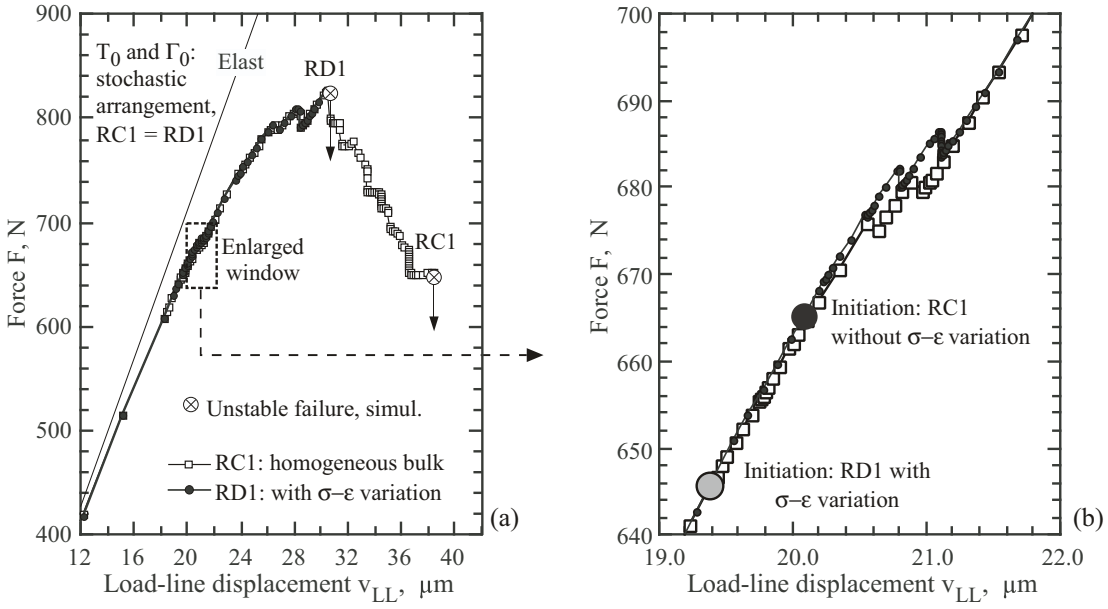

Figure 6.35: Comparison of the stochastic arrangements RD1 and RC1, with and without stochastic stress-strain curves, both with exact distributed stochastic cohesive parameters: (a) entire force vs. load-line displacement curve, (b) enlarged window at crack initiation.

Slightly different crack initiation and propagation can be seen in the Fig. 6.35 and Fig. 6.36. This is due to different notch tip properties of the RC1 and RD1, i.e., different σ-ϵ curves at the notch tips (σ-ϵ.5 for RD1, but average σ-ϵ.Mid for RC1), which results in different evolution of local σ_{22} and ϵ_{22} at RC1 and RD1.

6.3.5 Short summary

- The influence of the stochastic nature of the fracture parameter to the global response including sudden failure has been justified numerically with a stochastic approach in combination with the cohesive model.
- Some microstructural features have to be considered in the model for a better prediction of the experimental behavior. The information of the lamellae tilting, which produces a weak or strong colony (or soft and hard grain [77]), is applied to the chevron notch tip. With this additional information the simulations can quantitatively describe the experimental scatter.
- The stochastic approach considers a small variation band of the cohesive properties. Looking at the micro scale, the local variability may be larger than assumed (but not known in any case). At such micro-level the colony effect vanishes. Here, the variation band is considered for the meso surface of the colonies, where the very local variations are homogenized. Therefore, a small variation band for the fracture properties can be assumed.
- Simulations using a variation of σ-ϵ curves together with the cohesive parameters T_0 and Γ_0,

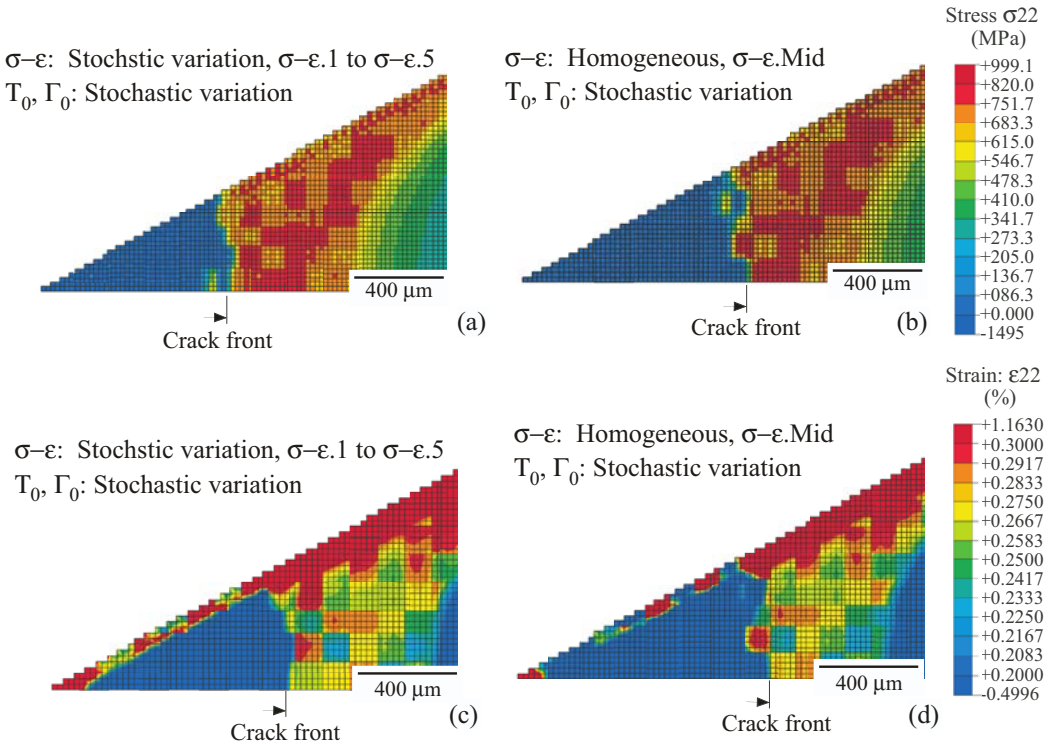

Figure 6.36: Stress and strain fields across the ligament for the stochastic arrangements RC1 and RD1 (as Fig. 6.35) at unstable failure of RD1 (v_{LL} = 30.6 μm): (a) RD1 with variable σ-ϵ curve with stress component normal to the fracture plane, (b) RC1 with homogeneous bulk (σ-ϵ.Mid), (c) RD1 with variable σ-ϵ curves, strain component normal to the fracture plane, (d) RC1 with homogeneous bulk (σ-ϵ.Mid).

show that the local constraint due to variable σ-ϵ-curves does not significantly influence the global response. Therefore, quite the same F-v_{LL} curves are found for the two different arrangements of RC1 and RD1. However, variations in the local deformation constraints have minor influence on the crack initiation.

Chapter 7

Transferability of the cohesive parameters

To predict the failure of structures the transferability of material parameters from laboratory test specimens to components has to be assured. A rigorous validation check with parameter transferability on a complex geometry is hard to conduct. Some transferability factors (e.g., constraint due to geometry or loading, environment) have to be determined that have to be related to the behavior of laboratory specimens and real components. For a simple case, the transferability of the model parameters can be verified on appropriate laboratory specimens with different geometries under equivalent loading conditions that are known from real component tests.

In this chapter, transferability of material parameters will be examined on a single edge notched bend (SE(B)) specimen with a straight notch. Such an SE(B) specimen with straight notch seems to have sufficient distinguished characteristics compared to the chevron notched bend specimen. Due to the differences in the straight and triangular notches, the crack initiation and propagation conditions are different.

As components are considered to be initially free of cracks, a bend specimen without a notch (or equivalent defect free) is also simulated. Such unnotched bend specimen is a worthwhile approximation of complicated loaded components like turbine blades, which undergoes bending and tension across the thickness.

7.1 Transferability of the cohesive parameters to the SE(B) specimen

A symmetric 3D geometry of the SE(B) specimen with the mesh design is shown in Fig. 7.1. The fracture plane was constructed with regular quadratic cohesive elements (20x20 μm^2). Shallow and deep notches with a_0/W = 0.35 and 0.6 were simulated. Details of the geometry are given in chapter 3, Fig. 3.2.

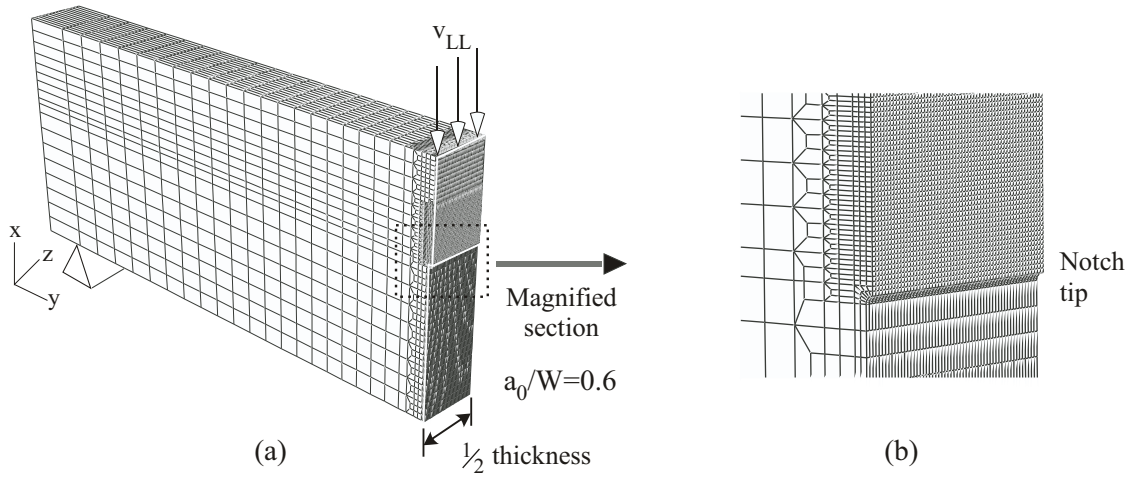

Figure 7.1: FE model of SE(B) specimen with $a_0/W = 0.6$

A single set of cohesive parameters was assigned to the fracture plane. In such assumption, the crack propagates evenly throughout the material showing no irregularities at the crack front.

For this analysis, the maximum cohesive traction, T_0, was fixed to 750 MPa, and the maximum cohesive energy, Γ_0, was varied from 3, 4 and 5 N/mm. The bulk material was assumed to be homogeneous and its elastic-plastic behavior was described by the $\sigma-\epsilon$.Mid curve. Fig. 7.2(a) shows the sensitivity of force-displacement curves (F-CMOD) for both notch depths calculated by a single set of cohesive parameters.

As expected from the analysis of chevron notched bend specimens, the global F-CMOD curves for the straight notch geometry is either continuous or discontinuous depending on the cohesive energy. For the discontinuous curves, the deformation controlled crack propagation could not extend further and the numerical calculations stopped, the situation is interpreted as uncontrolled crack propagation leading to abrupt failure as seen in the real specimens. In chapter 6, a similar behavior has been shown for the case of chevron notched bend specimens.

The simulations show that the maximum force and crack initiation for the straight notched SE(B) specimens satisfied the experimental results quite well, however, neither the scatter in force-deformation curves nor the scatter in failure points in the curves is fully satisfied by a single set of cohesive parameters.

The analysis is extended to the stochastic approach, where the cohesive parameters, T_0 and Γ_0 were randomly assigned across the entire fracture plane under its variation band. The variation bands for T_0 and Γ_0 were same as the chevron notched bend specimen, i.e., $680 \leqslant T_0 \leqslant 820$ MPa and $3 \leqslant \Gamma_0 \leqslant 5$ N/mm.

In Fig. 7.2(b), the stochastic simulations are compared with the experimental records of the F-CMOD curves for both notch depths, $a_0/W = 0.35$ and 0.6. For the case of $a_0/W = 0.6$, two random distributions have been performed, i.e., RS100a and RS100b. The effects of these distributions on the crack

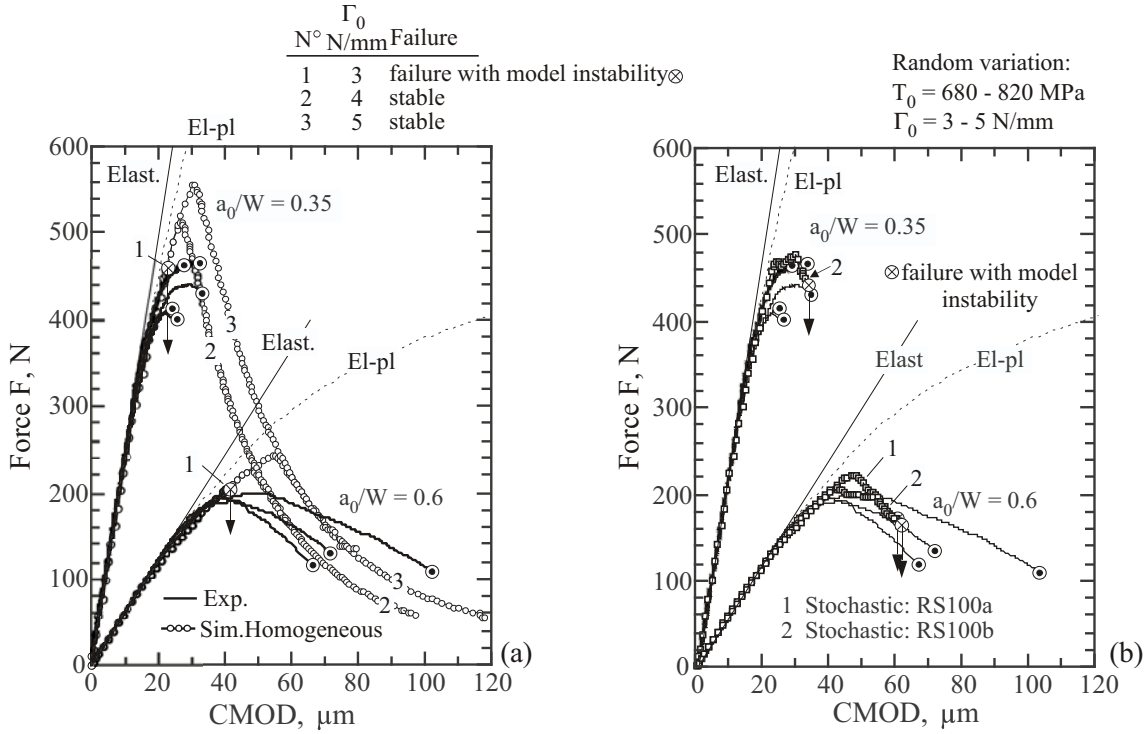

Figure 7.2: F-CMOD curves for SE(B) specimen for $a_0/W = 0.35$ and $a_0/W = 0.6$: (a) simulation results with a single set of cohesive parameters compared with the experimental curves, (b) simulation results with the stochastic arrangements compared with the experimental curves.

propagation can be seen from the global F-CMOD curves at their maximum load. Similarly, the distribution, RS100b, has been performed for the $a_0/W = 0.35$. From the simulation of both notch-depths it is shown that the randomly distributed stochastic parameters satisfy the characteristic features of the experiments very well, equivalent to the case of chevron notched specimens.

The maximum force and the onset of failure are reasonably predicted. For both notch depth ratios, the failure points on the curves are nearly equal to the experimental onset of abrupt failure. For the notch depth ratio, $a_0/W = 0.35$, the numerical instability occurs just after the onset of a crack. The prediction of specimen failure by the simulations is close to the experimental one.

It has been seen from the Fig. 7.2(a)(b) that the experimental curves lie somewhat below the simulated curves. The explanation may be related to the notch preparation. The spark eroded notch tip sustains some local damage at the notch surface which may introduce some strength decrease in the first row of colonies, which were not taken into account in the simulations.

The crack profiles of the homogeneous and the stochastic parameters at maximum load are shown in Fig. 7.3. An uneven crack front is obtained using the stochastic simulations. The characteristic behavior of the F-CMOD curves depends mainly on the amount of crack propagation, but marginally on the evolution of the crack front across the thickness. It seems that the stochastic approach can realistically simulate the crack front in a lamellar polycrystal on a macro-scale.

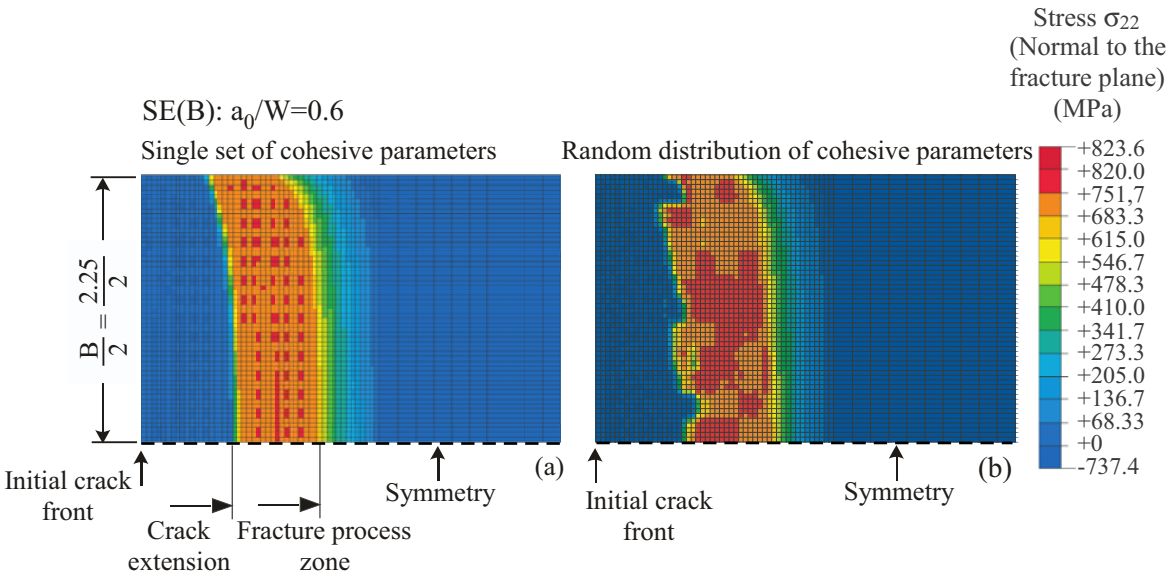

Figure 7.3: Crack profiles and fracture process zone with crack propagation at maximum force: (a) homogeneous or regular crack front using a single set of cohesive parameters, (b) irregular crack front using the stochastic arrangement, RS100a.

7.2 Influence of block size on the stochastic approach

Based on the information of lamellar microstructure, the colonies are simplified as blocks (100 μm x 100 μm) in the simulation. With this assumption the simulations satisfied the experimental results very well. To justify the applied block size, effects of the blocks on global force-displacement behavior have also been investigated.

The real microstructural fracture properties within a single colony may vary due to intra-lamellae fracture. Whereas in a block the micro-scale fracture properties are assumed to be averaged by a single set of cohesive parameters.

The simulations are systematically performed with quadratic blocks of 100, 60 and 20 μm sizes, where the lower limit of the block size is the cohesive element size itself, i.e., 20 μm. The stochastic approach is applied to the SE(B) specimens with a notch depth ratio of a_0/W = 0.6. Respective variation bands of the cohesive parameters are the same as before.

In Fig. 7.4(a), the simulated F-CMOD curves for three block sizes are plotted and compared with the single parameter set, T_0 = 750 MPa, Γ_0 = 4 N/mm as well as with the stochastic approach. The inserted window shows the curves at maximum force.

The F-CMOD curve for the 20 μm block size, the stochastic combination RS20, is completely continuous and follows the curve of the single parameter set. The 60 μm and 100 μm block sizes, RS60 and RS100a,b respectively, exhibit numerical failure where the failure-points are situated close to each other. The RS100a and RS100b have the same block sizes but are attributed with different random

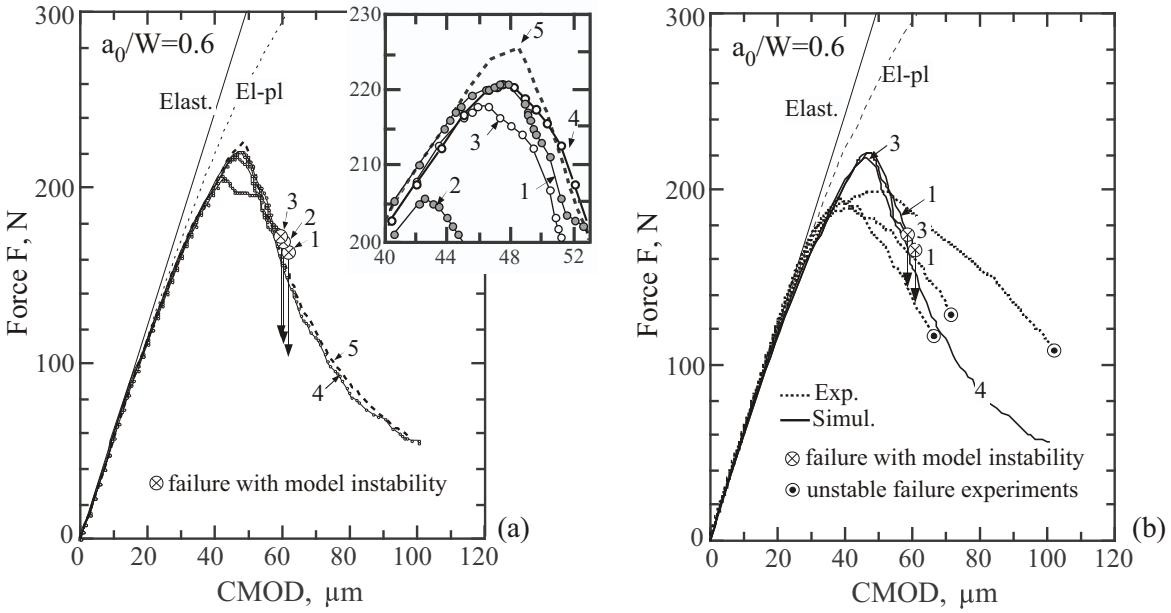

N°	Blocksize (μm)	Notation	Failure behavior
1	100	RS100a	⊗model instability
2	100	RS100b	⊗model instability
3	60	RS60	⊗model instability
4	20	RS20	stable

Single set parameter			Stochastic parameter
N°	T_0 (MPa)	Γ_0 (N/mm)	T_0 = 680-820 MPa
5	750	4	Γ_0 = 3-5 N/mm

Figure 7.4: Influence of block size on the F-CMOD curves for $a_0/W = 0.6$: (a) stochastic arrangements compared with the single set parameters, (b) stochastic arrangements compared with the experimental curves.

distributions.

For the 20 μm block the stochastic distribution is more refined. Due to small block size, the block failure per element results in a micro-sized defect. In global force-displacement response, initiation of a single micro-sized defect has no significant influence. However, when several micro-sized defects are clustered somewhere on the fracture plane, a significant change in the force-displacement curves can be noticed. In the case of 20 μm block size, a clustered area on the fracture plane is not obtained by the randomly distributed fracture parameters. A clustered area, however, is automatically generated by the larger blocks. With reducing block size the colony characteristics are lost, which makes qualitatively almost no difference with the complete homogeneous case.

In Fig. 7.4(b), the F-CMOD curves from stochastic simulations for three types of blocks are compared with the experimental data. The simulated unstable failures with the bigger blocks (100 and 60 μm) match very well with the experimental failure points. The experimental curves are found to be marginally softer before reaching the maximum force which are situated below the simulation maximum. Under-estimating the experimental maximum load is due to the notch damage during notch preparation. Such effects are not considered in the present simulation.

Fig. 7.5 shows the crack profiles for the different block sizes. As shown, the crack paths for the 100 and 60 μm block sizes are better related to the microstructural observation of the lamellar fracture surfaces. This irregularity along the crack front is homogenized with the reduction of the block size and no significant differences have been found between the crack fronts for the random approach with block size 20 μm and the homogeneous approach with a single set parameter.

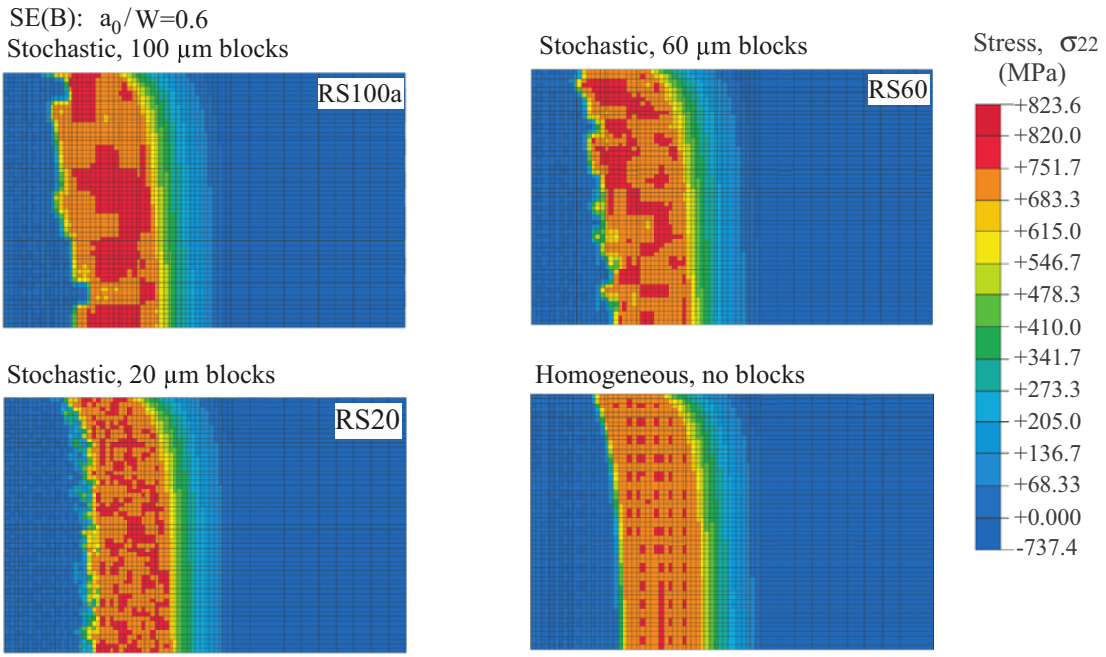

Figure 7.5: Crack profiles and activated cohesive zones during crack propagation for different block size.

The above investigations suggest that the choice of block sizes has to be appropriately related to the given microstructure. Providing this microstructural information the micromechanical based cohesive damage model can predict the global fracture behavior of the γTAB as seen in the experiments.

7.3 Fracture behavior of a defect-free bend specimen

Force-displacement behavior of a defect-free (unnotched) bend specimen is presented in this section. Failure of a component with possible crack development under bending can be qualitatively explained with this simplified specimen.

The geometry of the bend specimen is taken from the pre-notched bend specimen, only the notch has been eliminated from the FE mesh. As there is no pre-crack in the model, no crack-mouth-opening-displacement (CMOD) can be measured. However, in the present analysis, the displacement, CMOD, on the unnotched bend specimen is calculated on the same points as were taken for the notched bend specimens. The gauge length is the notch width, i.e., about 70 μm (this width is due to the spark erosion with a 50 μm wire).

A fracture surface is modeled with a single set of cohesive parameters. For the cohesive energy, Γ_0, three values are considered, i.e., Γ_0 = 3, 4, and 5 N/mm, each of them is combined with a fixed cohesive traction, T_0 = 750 MPa. The simulation results are shown in Fig. 7.6(a).

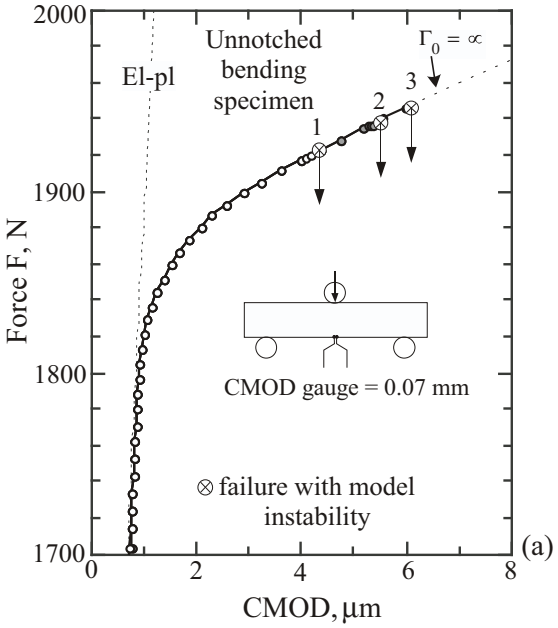

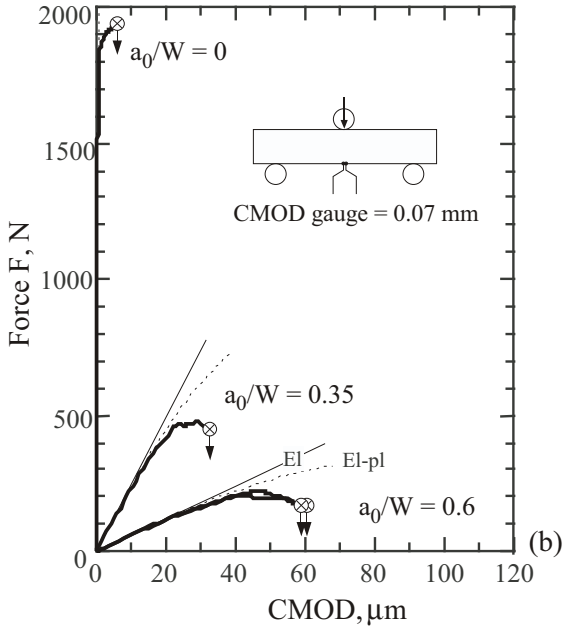

Homogeneous simulation

N°	T_0 (MPa)	Γ_0 (N/mm)
1	750	3
2	750	4
3	750	5

Figure 7.6: Simulated F-CMOD curves for unnotched bend specimens: (a) F-CMOD curves for different cohesive energies, Γ_0, (b) comparison of unnotched and notched bend specimens.

For all F-CMOD curves shown in the figure, the simulations stopped after showing short nonlinear deformation. Such numerical performance can be interpreted as unstable failure of a specimen (also recall numerical instability discussed in section 5.1 and 6.3). At this point the separation of a cohesive element did not yet reach the maximum separation, δ_0, to initiate a physical crack. As understood, a full separation of the cohesive elements (i.e., crack initiation) is not necessarily required for developing unstable failure situation in an unnotched specimen in contrast to a precracked specimen.

The failure points shown in Fig. 7.6(a) lie very closely for the different Γ_0 values. The nonlinear F-CMOD behavior prior to unstable failure is a result from the Rect-TSL. An ideally plastic behavior is activated before reaching the unloading part in the TSL.

With a very large Γ_0 value, unstable failure would be shifted along the extrapolation (dotted line) of the initial curve in Fig. 7.6(a). For infinite Γ_0, no unstable failure would occur, instead, a saturation level with plastic collapse due to an ideal-plastic material behavior would be reached.

As no crack propagation prior to failure has been obtained, stochastic nature of crack initiation and

propagation can not be predicted. Therefore, no fracture simulations with the stochastic approach have been performed. From the knowledge of the previous analysis it can be said for the unnotched bend specimen that the stochastic approach will produce variable strain to failure, which will lie within the values as obtained from the single set parameter calculations with different Γ_0 values.

The simulated F-CMOD curves for different bend specimens (unnotched and notched) are compared in Fig. 7.6(b). The displacement, CMOD, on the unnotched bend specimen is determined at the same points as were taken for the notched bend specimens. The notch effects can easily be seen from the curves. The F-CMOD relation for an unnotched specimen is not confirmed by the experiments. However, in previous sections this F-CMOD relations have been validated for the notched specimens.

Chapter 8

Summary and conclusion

A hybrid methodology of characterizing the quasi-brittle fracture of fully lamellar γTAB alloy has been presented in this work. The methodology incorporates micromechanics based damage defined by a traction-separation law within a cohesive model and scatter of material properties described by the stochastic approach. The following assumptions are taken for the analysis:

- Fracture of a colony (at meso-scale) is fully described by the fracture properties of the cohesive model (fracture strength is represented by cohesive strength, T_0, and fracture toughness is represented by cohesive energy, Γ_0).
- The variation band of the fracture parameters at a meso-scale (scale of colonies) is taken small assuming that the very local fracture parameters at a micro-scale (scale of lamellae) are averaged in a colony. However, the variation band of fracture parameters for single lamellar break is probably quite large.
- Some extreme frequency distributions of the fracture properties are assumed. The stochastic nature of fracture is fully attributed to the stochastic distribution of cohesive fracture properties. Crack initiation (or fracture) in a colony is defined by the stochastic values of critical material separation, δ_0, which is calculated from the Eq. (4.3).

The fracture behavior is investigated adopting experiments, fracture surface analyses, and simulations. Mechanical properties of the γTAB alloy and its quasi-brittle fracture behavior have been identified by testing miniature specimens. Thereafter, global force-displacement phenomena of this particular material have been simulated adopting macroscopic FE models. A micromechanical based crystal plasticity model has been used to determine the local variability of the stress-strain responses of lamellar colonies in a polycrystal.

As the fracture plane is known in advance for the tested specimens, a predefined fracture plane has been introduced in the FE model. Random effects of material fracture properties are attributed to this

fracture plane. Fracture properties of the colonies and their variations are represented by cohesive parameters. The variations of colony-stiffness are represented by the respective stress-strain responses. Some microstructure related assumptions, like colony size, colony orientation etc. are also introduced in the numerical model. The lamellar colonies are simplified as quadratic blocks. The fracture behavior of strong or weak colonies (depending on the orientation of lamellar colonies) are interpreted through the combination of high and low values of the cohesive parameters (T_0 and Γ_0). The global fracture behavior as seen from the bending specimens, which is influenced by the differently oriented colonies at the triangular notch tip, has been numerically captured by varying the material properties in few blocks at the notch tip. The required information for this variation was taken from the fractographic analysis.

The model parameters and their variation band are determined in several steps. Preliminary information of the model parameters has been obtained from a 2D simulation of the bend specimen. They are verified on the 3D FE models of bend specimens and validated with the experimental results. The variation band of cohesive traction, T_0, has been taken from the fracture points of the tensile-test curves and the variation band of cohesive energy, Γ_0, has been obtained by fitting the cohesive fracture simulation with the experimental curves from bending tests. The variation bands of the local fracture parameters (T_0 and Γ_0) are found small compared to the local variation band reported in the literature. However, the small variation band has been validated with the global fracture phenomena of the chevron notched bend specimen. Finally, material parameters from Chevron notched specimen are transferred to a fracture specimen of different geometry (SE(B) with straight notch) for which the global unstable failure has been predicted quite well.

From the tensile test simulations, crack initiation and final failure under tensile loading are predicted close to the reality. The scatter band of the experimental $\sigma-\epsilon$ curves from the tensile tests has been fairly captured. From the simulation of chevron notched bend specimen, the influence of the variability of fracture properties on the global response has also been justified. It has been shown that the realistic simulation of fracture evolution and the prediction of experimental scatter need a qualitative description of the microstructure in the numerical model.

The presented approach showed that the cohesive damage model combined with the proposed stochastic approach with a simplified distribution function and a small variation band of local material parameters can quantitatively predict the quasi-brittle fracture of the γTAB alloy. The scatter of the fracture curves obtained from the bending tests, pop-in phenomena, and unstable failure have been quantitatively predicted. The approach can give an appropriate physical insight into the effects of property variability on the crack initiation and propagation for the fully lamellar γTAB alloy.

From the investigation of deformation and fracture behavior of γTAB alloy, several conclusions can be drawn, which are stated subsequently:

Micromechanical crystal plasticity model of tensile deformation:

- Two-scale simulations on a 4x4x4 colony cube with random orientations proved that the inhomogeneous local stress-strain response depends on the deformation constraint exhibited by the lamellar colonies in a polycrystal. The plastic part of the $\sigma-\epsilon$ curve up to 1-2% plays an important role for the local constraintd behavior. In polycrystals this constraint effects prevail everywhere. The mechanical behavior of a single colony embeded in a polycrystal is influenced by the imposed constraint from the neighbouring colonies.

- The random orientation of lamellae in radial direction (orientation against the load axis) delivers the strongest contribution to the constraint effects (refer to the section 6.1.4).

- Simulations with a crystal-plasticity deformation model indicate that the local mechanical behavior of the colonies expressed in terms of stress-strain curves vary within a large range. The model does not include fracture, therefore, no information about the variation of fracture toughness and strength in a colony is obtainable.

Macromechanical modeling of fracture:

- The tensile simulations showed that the local stress evolution due to deformation constraint plays an important role for crack initiation. The bending test simulations showed that the local colony orientations control the crack propagation through the lamellar microstructure.

- Stochastic simulations using the frequency distribution functions proved that each tensile specimen has its own distribution function of the material properties.

- The proposed modeling approach can quantitatively explain almost all phenomena of quasi-brittle fracture of γTAB that have been observed from the global load-displacement curves. A statistical approach can not be realistically applied when a few test data is available. However, using limited test results in the proposed model, quite good prediction of the global crack propagation and failure has been made. In this case a quantitative analysis from the fractography was needed for a better description of the model.

- A small variation band of local fracture properties for colony break has been assumed in the simulation, and is validated with the global responses of the specimens. As common in statistical FE method, a big variation band of local properties has to be assumed which would satisfy the global scatter described by the phenomenological Weibull distribution. Such statistical FE method considers very local fracture properties (e.g., micro-defect due to particle failure) but not the microstructural information like colony orientation or colony size etc. However, the proposed approach assumes that the fracture properties and the material response are related to a meso scale description. It has been shown that the small variation band can reproduce the global experimental scatter quite satisfactorily.

- Prediction of crack initiation and final failure is quite important for structures or components. It has been shown that the cohesive model with an appropriate TSL shape (here the Rect-TSL) can capture the basic fracture phenomena of a component. Stochastic crack initiation, crack extension can be predicted quite well.

Outlook

Prediction of component failure using micromechanics based description of deformation and damage at full length-scale (micro-meso-macro) is the recent modeling challenge. In the present work, different length scales are considered discretely, for example, a micro-meso model for explaining scatter in local stress-strain behavior that are influenced by the colony orientation, the meso-scale fracture of the colonies described by the cohesive model, and the scatter in the global force-displacement behavior using macro-scale specimens. Until now, no comprehensive multi-scale model for TiAl alloy can be found that links the global failure of a component with the micro-scale fracture mechanisms, for example, micro-crack initiation and propagation through lamellae. Also, in any micro-scale model for TiAl alloy, the evolution of cracks considering the influences of the variation of local stiffness and fracture properties is not explicitly defined. An extensive work has to be done to develop such full-scale model.

The present approach predicts the global failure of a fully lamellar alloy considering microstructural variation of material properties. However, its application to a wide range of TiAl microstructures (for example, globular, nearly lamellar, duplex, etc.) is still open. Some other critical issues related to the proposed approach are stated as follows:

- Information about the variation band of the fracture parameters at a micro-level was not experimentally obtained. Sufficient knowledges about the variation band can be obtained through tensile testing of a single colony with different orientations, or adopting micro-hardening tests on single colonies.
- The distribution functions of the material properties were unknown. A number of experiments are needed to obtain the functions.

The effectiveness of the approach can be enhanced by answering these issues. Moreover, further investigations are needed to ensure the transferability of the model parameters to a real component.

Bibliography

[1] E. A. Loria. Gamma titanium aluminide as prospective structural materials. *Intermetallics*, 8:1339–1345, 2000.

[2] Y.-K. Kim and D. M. Dimiduk. Progress in understanding of gamma titanium aluminides. *Journal of Materials*, 43(8):40–47, 1991.

[3] M. Peters, J. Kumpfert, C. H. Ward, and C. Leyens. *Titanium alloys for aerospace application*, chapter 13. Wiley-Vch Verlag, 2003.

[4] K. S. Chan and Y.-W. Kim. Effects of lamellae spacing and colony size on the fracture resistance of a fully lamellar TiAl alloy. *Acta Metallurgica et Materialia*, 43:439–451, 1995.

[5] G. Cao, L. Fu, J. Lin, Y. Zhang, and C. Chen. The relationship of microstructure and properties of a fully lamellar TiAl alloy. *Intermetallics*, 8:647–653, 2000.

[6] D. M. Dimiduk, P. M. Hazzledine, T. A. Parthasarathy, S. Seshagiri, and M. G. Mendiratta. The role of grain size and selected microstructural parameters in strengthening fully lamellar TiAl alloys. *Metallurgical and Materials Transactions A*, 29A:37–47, 1998.

[7] F. Appel and R. Wagner. Microstructure and deformation of two-phase γ-titanium aluminides. *Materials Science and Engineering: R: Reports*, 22:187–268, 1998.

[8] G. Bao and Z. Suo. Remarks on crack-bridging concepts. *Applied Mechanics Reviews*, 45:355–366, 1992.

[9] K. S. Chan and D. L. Davidson. The fracture resistance and crack-tip micromechanics of in-situ intermetallic composites. *Journal of Materials*, 48:62–67, 1996.

[10] K. S. Chan and Y.-W. Kim. Influence of microstructure on crack-tip micromechanics and fracture behaviors of a two-phase TiAl alloy. *Materials Transactions A*, 23A:1663–1677, 1992.

[11] J. J. M. Arata, K. S. Kumar, W. A. Curtin, and A. Needleman. Crack growth in lamellar titanium aluminide. *International Journal of Fracture*, 111:163–189, 2001.

[12] D. A. Knaul and J. L. Beuth J. G. Milke. Modeling and measurement of the notched strength of gamma titanium aluminides under monotonic loading. *Metallurgical and Materials Transactions A*, 30A:949–959, 1999.

[13] F. Appel, U. Lorenz, T. Zhang, and R. Wagner. Fracture behavior of two-phase γ-titanium aluminides. *Material Research Society, Symposium Proceeding*, 364:493–498, 1995.

[14] J. D.H. Paul, M. Oehring, R. Hoppe, and F. Appel. Strength properties of a precipitation hardened high niobium containing titanium aluminide alloy. *The Minerals, Metals and Material Society (TMS)*, pages 493–501, 2003.

[15] N. Biery, M.D. Graef, J. Beuth, R. Raban, A. Elliott, C. Austin, and T.M. Pollock. Use of Weibull statistics to quantify property variability in TiAl alloys. *Metallurgical and Materials Transactions A*, 33A:3127–3136, 2002.

[16] H. Uhlenhut. *Ursachen plastischer Anisotropie von γ-TiAl-Basislegierungen*. PhD thesis, Technical University of Hamburg-Harburg, 1999.

[17] O. Diard, S. Leclercq, G. Rousselier, and G. Cailletaud. Evaluation of finite element based analysis of 3D multicrystalline aggregates plasticity: Application to crystal plasticity model identification and the study of stress and strain fields near grain boundaries. *International Journal of Plasticity*, 21:691–722, 2005.

[18] A. Cornec, M. Werwer, and V. Heitmann. Micromechanical modeling of deformation and fracture in lamellar gamma-TiAl alloys. *Gamma Titanium Aluminides 2003, The Minerals, Metals and Materials Society (TMS)*, pp. 493-501, 2003.

[19] H. Takahashi, H. Motohashi, M. Tokuda, and T. Abe. Elastic-plastic finite element polycrystal model. *International Journal of Plasticity*, 10:63–80, 1992.

[20] S. M. Schlögl and F. D. Fischer. The role of slip and twinning in the deformation behaviour of polysynthetically twinned crystals of TiAl: a micromechanical model. *Philosophical Magazine A*, 75:621–636, 1997.

[21] A. Charkraborty and J. C. Earthman. Numerical models of creep cavitation in single phase, dual phase and fully lamellar titanium aluminide. *Acta Materialia*, 45:4615–4626, 1997.

[22] S. R. Kalidindi. Incorporation of deformation twinning in crystal plasticity models. *Journal of the Mechanics and Physics of Solids*, 46:267–290, 1998.

[23] R. Lebensohn, H. Uhlenhut, C. Hartig, and H. Mecking. Plastic flow of γ-TiAl-based polysynthetically twinned crystals: micromechanical modeling and experimental validation. *Acta Materialia*, 46:4701–4709, 1998.

[24] W. T. Marketz, F. D. Fischer, and H. Clemens. Micromechanical modelling of the deformation behaviour of gamma titanium aluminides. *Zeitschrift für Metallkunde*, 90:588–593, 1999.

[25] M. Werwer and A. Cornec. The role of superdislocations for modeling plastic deformation of lamellar TiAl. *International Journal of Plasticity*, 22:1683–1698, 2006.

[26] J. Schicker and M.Pfuff. Statistical modeling of fracture in quasi-brittle materials. *Advanced Engineering Materials*, 8(5):406–410, 2006.

[27] M. Grujicic and Y. Zhang. Crystal plasticity analysis of the effect of dispersed β-phase on deformation and fracture of lamellar $\gamma + \alpha_2$ titanium aluminide. *Materials Science and Engineering*, A265:285–300, 1999.

[28] M. H. Yoo, J. Zou, and C. L. Fu. Mechanistic modeling of deformation and fracture in TiAl and Ti_3Al. *Materials Science and Engineering*, A192/193:14–23, 1995.

[29] W. Weibull. A statistical theory of the strength of materials. *Ing. Vetenskaps Akad. Handl.*, 151:1–45, 1939.

[30] W. Weibull. A statistical distribution function of wide applicability. *Journal of Applied Mechanics*, pages 293–297, 1951.

[31] S. She and J. D. Landes. Statistical analysis of fracture in graphite. *International Journal of Fracture*, 63:189–200, 1993.

[32] C. Berdin, G. Cailletaud, and D. Jeulin. Brittle failure prediction of ceramics using a multiscale approach. *Journal of the American Ceramic Society*, 79(11):2825–32, 1996.

[33] P.Rossi and S.Richer. Numerical modeling of concrete cracking based on a stochastic approach. *MS*, 20:334–337, 1987.

[34] V. V. Silberschmidt. Effect of materials randomness on scaling of crack propagation in ceramics. *International Journal of Fracture*, 140:73–85, 2006.

[35] C. Baxevankis, D. Jeulin, B. Lebon, and J. Renard. Fracture statistics modeling of laminate composites. *International Journal of Solids Structures*, 35 No 19:2505–2521, 1998.

[36] M. Yamaguchi and Y. Umakoshi. The deformation behaviour of intermetallic superlattice compounds. *Progress in Materials Science*, 34:1–148, 1990.

[37] A. Godfrey, D. Hu, and M. H. Loretto. The role of α_2 phase in the transmission of slip in lamellar TiAl-based alloys. *Philosophical Magazine A*, 77:287–289, 1998.

[38] D. Hu and M. H. Loretto. Slip transfer between lamellae in fully lamellar TiAl alloys. *Intermetallics*, 7:1299–1306, 1999.

[39] S. Jiao, N. Bird, P. B. Hirsch, and G. Taylor. Characteristics of ordinary 1/2 ⟨110] slip in single crystals of γ-TiAl. In *Mat. Res. Soc. Symp. Proc*, volume 552, pages KK8.11.1–KK.8.11.5, 1999.

[40] Y. Umakoshi and T. Nakano. The role of ordered domains and slip mode of α_2 phase in the plastic behaviour of TiAl crystals containing oriented lamallae. *Acta Metallurgica et Materialia*, 41:1155–1161, 1993.

[41] J. M. K. Wiezorek, X.-D. Zhang, W. A. T. Clark, and H. L. Fraser. Activation of slip in lamellae of α_2-Ti_3Al in TiAl alloys. *Philosophical Magazine A*, 78:217–238, 1998.

[42] V. Paidar, D. Imamura, H. Inui, and M. Yamaguchi. Plastic deformation of bicrystals composed of polysynthetically twinned TiAl crystals. *Acta Materialia*, 49:1009–1019, 2001.

[43] T. Fujiwara, A. Nakamura, M. Hosomi, S. R. Nishitani, Y. Shirai, and M. Yamaguchi. Deformation of polysynthetically twinned crystals of TiAl with nearly stoichiometric composition. *Philosophical Magazine A*, 61:591–606, 1990.

[44] H. Inui, A. Nakamura, M. H. Oh, and M. Yamaguchi. Deformation structure in Ti-rich polysynthetically twinned crystals. *Philosophical Magazine A*, 66:557–573, 1992.

[45] M.-C. Kim, M. Nomura, V. Vitek, and D. P. Pope. Deformation of polysynthetically twinned TiAl single crystals with near-hard orientations. In *Mat. Res. Soc. Symp. Proc*, volume 552, pages KK.3.1.1–KK.3.1.6, 1999.

[46] M. Werwer. *Mikromechanische Modellierung des Verformungs- und Bruchverhaltens von lamellarem TiAl*. PhD thesis, Technische Universität Hamburg-Harburg, Internal Report, GKSS 2005/12, ISSN 0344-9629, 2005.

[47] I.Scheider, W.Brocks, and A.Cornec. Procedure for the determination of true stress-strain curves from tensile tests with rectangular cross-section specimens. *Journal of Engineering Materials and Technology*, 126:70–76, 2004.

[48] B. F. Dorensen, P. Brethe, and P. S. Hansen. Controlled crack growth in ceramics: the DCB specimen loaded with pure moments. *Journal of the European Ceramic Society*, 16:1021–1025, 1996.

[49] E. E. Gdoutos. *Fracture Mechanics An Introduction*. Springer Publisher, 2nd edition, 2005.

[50] K. Takashima, T. P. Halford, D. Rudinal, Y. Higo, and M. Takeyama. Micro fracture toughness testing of TiAl based alloys with a fully lamellar structure.

[51] S. M. Barinov. On toughening in TiAl. *Journal of Materials Science Letters*, 15:1765–1766, 1996.

[52] K. S. Chan, P. Wang, N. Bhate, and K. S. Kumar. Intrinsic and extrinsic fracture resistance in lamellar TiAl alloys. *Acta Materialia*, 52:4601–4614, 2004.

[53] M.H. Yoo and C.L. Fu. Cleavage fracture of ordered intermetallic alloys. *Material Science and Engineering*, A153:470–478, 1992.

[54] A. A. Griffith. The phenomena of rapture and flow in solids. *Philosophical Transactions of the Royal Society*, A221:163–198, 1920.

[55] G. R. Irwin. Analysis of stresses and strains near the end of a crack traversing a plate. *Journal of Applied Mechanics, ASME*, pages 361–364, 1957.

[56] J. Rice. A path independent integral and the approximate analysis of strain concentrations by notches and cracks. *Journal of Applied Mechanics, ASME*, 35:379–386, 1968.

[57] A. A. Wells. Application of fracture mechanics at and beyond general yielding. *British Welding Journal*, 10:563–670, 1963.

[58] D. S. Dugdale. Yielding of steel sheets containing slits. *Journal of The Mechanics and Physics of Solids*, 8:100–106, 1960.

[59] G. Barenblatt. The mathematical theory of equilibrium cracks in brittle fracture. *Advances in Applied Mechanics*, 7:55–129, 1962.

[60] A. Needleman. A continuum model for void nucleation by inclusion debonding. *Journal of Applied Mechanics*, 54:525–531, 1987.

[61] V. Tvergaard and J. W. Hutchinson. The influence of plasticity on the mixed mode interface toughness. *Journal of the Mechanics and Physics of Solids*, 41:1119–1135, 1993.

[62] A. Hillerborg, M. Modeer, and P. E. Petersson. Analysis of crack formation and crack growth in concrete by means of fracture mechanics and finite elements. *Cement and Concrete Research*, 6:773–782, 1976.

[63] K.-H. Schwalbe and A Cornec. Modelling crack growth using local process zones. *Technical report*, 1994.

[64] A. Needleman. An analysis of decohesion along an imperfect interface. *International Journal of Fracture*, 42:21–40, 1990.

[65] Z.P.Bazant. Concrete fracture models: testing and practice. *EFM*, 69:165–205, 2002.

[66] Z. K. Bazant. Concrete fracture models: testing and practice. *Engineering Fracture Mechanics*, 69:165–205, 2002.

[67] I. Scheider and W. Brocks. Simulation of cup-cone fracture using the cohesive model. *Engineering Fracture Mechanics*, 70:1943–1961, 2003.

[68] I. Scheider. *Bruchmechanische Bewertung von Laserschweißverbindungen durch numerische Rißfortschrittsimulation mit dem Kohäsivzonenmodell*. PhD thesis, TU Hamburg-Harburg, Internal Report, GKSS 2001/3, 2001.

[69] W. Feller. An introduction to probability and its applications. *Volume II, John Wiley & Sons, USA*, 1996.

[70] M. Werwer, R. Kabir, A. Cornec, and K.-H. Schwalbe. Fracture in lamellar TiAl simulated with the cohesive model. *Engineering Fracture Mehanics*, 74:2615–2638, 2007.

[71] S.Kruch, J.L. Chaboche, and T. Pottier. Two-scale viscoplastic and damage analysis of a metal matrix composite. *In G.Z. Voyiadjis and D.H Allen, editors, Damage and Interfacial Debonding in Composites, Studies in applied Mechanics*, 44, 1996.

[72] M. Werwer and A. Cornec. Numerical simulation of plastic deformation and fracture in polysynthetically twinned (PST) crystals of TiAl. *Computational Materials Science*, 19:97–107, 2000.

[73] Y. Huang. A user-material subroutine incorporating single crystal plasticity in the ABAQUS finite element program. Report MECH - 178, Division of Applied Science, Havard University, Cambridge, Massachusetts, 1991.

[74] G. Lin and M. Werwer. An ABAQUS user material subroutine incorporating single crystal plasticity for simulation of titanium aluminide based alloys. Technical report, GKSS, Technical Note GKSS/WMS/01/01, 2001.

[75] M. Yamaguchi, H. Inui, and K. Ito. High-temperature structural intermetallics. *Acta Materialia*, 48:307–322, 2000.

[76] *ABAQUS User Manual*, volume 6.5. Habbit, Karlsson, and Sorensen Inc., Pawtucket, Ri, USA, 2005.

[77] R. T. Zheng, Y. G. Zhang, and C. Q. Chen. Microcrack nucleation and its effect on the plastic deformation of FL γ-TiAl alloy. *Journal of Materials Science*, 39:1721–1725, 2004.

Acknowledgement

The thesis work has been done during my stay in GKSS Research Centre Geesthacht as a scientific fellow. I would like to thank my supervisor at GKSS, Prof. Wolfgang Brocks, for his guidance and support. I am grateful for his suggestions and comments on mechanics and modeling aspects that greatly improved the quality of this work. Also, kind gratefulness to Prof. Helmut Föll and Prof. Rainer Adelung from Christian-Albrechts-Universität zu Kiel for their valuable suggestions and comments.

I am very grateful to the members of the working group, WMS at GKSS Research Centre, who were always beside me with their suggestions and comments. My warm thanks to Dr. Alfred Cornec for his unwavering support throughout the work. Our discussion on fracture mechanics issues and numerical techniques for handling technical problems widen my knowledge greatly. Special thanks to Dr. Michael Pfuff for the friendly discussion regarding the stochastic problems of material heterogeneity. Furthermore, I would like to thank Dr. Dirk Steglich and Dr. Ingo Scheider who always kept their doors open for any kind of suggestions and constructive ideas.

I greatly acknowledge the financial support of the German Research Foundation (DFG). This project has been done as an extension of the previous research work on the "Micromechanics of Multiphase Materials, SFB 371". I am grateful to the SFB for providing their results.

Finally, I would like to take the opportunity to thank my family for their encouragement and support, that motivated me throughout the harder times. Also thanks to my friends who were by my side in every situations.